WELDING OF T-JOINT CONFIGURATION BETWEEN DISSIMILAR METALS USING LOW POWERED FIBER LASER

SHAMINI A/P P.JANASEKARAN

FACULTY OF ENGINEERING
UNIVERSITY OF MALAYA
KUALA LUMPUR

2017

WELDING OF T- JOINT CONFIGURATION BETWEEN DISSIMILAR METALS USING LOW POWERED FIBER LASER

SHAMINI A/P P.JANASEKARAN

THESIS SUBMITTED IN FULFILMENT OF THE REQUIREMENTS FOR THE DEGREE OF DOCTOR OF PHILOSOPHY

FACULTY OF ENGINEERING
UNIVERSITY OF MALAYA
KUALA LUMPUR

2017

UNIVERSITY OF MALAYA
ORIGINAL LITERARY WORK DECLARATION

Name of Candidate: Shamini A/P P.Janasekaran

(I.C/Passport No:

Matric No: KHA120086

Name of Degree: The Degree of Doctor of Philosophy

Title of Project Paper/Research Report/Dissertation/Thesis ("this Work"):

Welding of T-joint configuration between dissimilar metals using low powered fiber laser

Field of Study: Manufacturing Processes (Engineering and Engineering Trades)

I do solemnly and sincerely declare that:

(1) I am the sole author/writer of this Work;
(2) This Work is original;
(3) Any use of any work in which copyright exists was done by way of fair dealing and for permitted purposes and any excerpt or extract from, or reference to or reproduction of any copyright work has been disclosed expressly and sufficiently and the title of the Work and its authorship have been acknowledged in this Work;
(4) I do not have any actual knowledge nor do I ought reasonably to know that the making of this work constitutes an infringement of any copyright work;
(5) I hereby assign all and every rights in the copyright to this Work to the University of Malaya ("UM"), who henceforth shall be owner of the copyright in this Work and that any reproduction or use in any form or by any means whatsoever is prohibited without the written consent of UM having been first had and obtained;
(6) I am fully aware that if in the course of making this Work I have infringed any copyright whether intentionally or otherwise, I may be subject to legal action or any other action as may be determined by UM.

Candidate's Signature   Date:

Subscribed and solemnly declared before,

Witness's Signature   Date:

Name:

Designation:

ABSTRACT

Welding is a fabrication process of joining two different parts together and in some welding process it involves heat transmission between two metals to get strong joint. Welding process can be divided into two categories, which are fusion welding and solid state welding processes. The drawbacks of these fusion methods are welding can damage the surface of the materials and need precise techniques with skilled and trained operators. Laser beam welding technique was established on high power laser machine which requires high capital cost and investment. However, with the advancement of fiber laser technology, there is possibility of using low power fiber laser welding to weld dissimilar metals. In this research, low power fiber laser welding were used to weld T-joint on dissimilar metals. A fuzzy logic model was developed from the training data and validated with testing data from pull test results to select parameter range for further metallurgical and microhardness analysis. In preliminary study, dissimilar aluminum alloys of AA2024-O acted as skin and AA7075-T6 acted as stringer were welded double-sided to evaluate the joining capability. The influences of laser welding speed and focal distances for constant laser power, 270 W were studied to determine the weldment penetration in this study. It was found that full penetration was obtained at welding speed 9mm/s with the highest heat input approximately 4715 J/mm needs 642.79N to break the joints. The microstructural analysis proved the formation of smaller grain sizes due to laser welding. Vickers microhardness did not show improvement in weldment hardness and filler alloy, BA4047 was added to evaluate its influence to mechanical properties. For the same parameters, the fracture force and Vickers microhardness increased approximately 300% and 1200% respectively when filler alloy was added. Single sided laser welding has advantage for inaccessible seam welding. Titanium base alloy, Ti6Al4V as skin and nickel base alloy, Inconel 600 as stringer were welded in T joint configuration using same technique. Overlapping factor

and welding speed were studied and the effects were examined. The maximum force, 150N needed to fracture the welded sample when the overlapping factor was 50% and the welding speed was 40 mm/s at a given constant power of 250W. Microhardness has increased 200% from base metals with formation of intermetallic compound, NiTi and $NiTi_2$ formed at fusion zone from the Energy Dispersive X-Ray Spectroscopy and X-ray diffraction analysis. Overall, double sided and single sided laser welding was possible using low power fiber laser to form a sound weldment.

ABSTRAK

Kimpalan ialah proses fabrikasi yang menyambungkan dua bahagian yang berbeza bersama dan dalam beberapa proses kimpalan ia mungkin melibatkan pengaliran haba antara dua logam untuk mendapatkan ikatan yang kuat. Proses kimpalan boleh dibahagikan kepada dua kategori iaitu kimpalan pelakuran dan proses kimpalan keadaan pepejal. Kelemahan kaedah pelakuran adalah kimpalan boleh merosakkan permukaan bahan dan memerlukan teknik yang tepat dan operator terlatih. Sebelum ini, teknik kimpalan laser rasuk digunakan pada mesin laser kuasa tinggi yang berkos tinggi. Namun, dengan kemajuan teknologi gentian laser, terdapat kemungkinan menggunakan gentian kuasa yang rendah laser kimpalan untuk mengimpal berlainan. Dalam kajian ini, kuasa rendah laser kimpalan gentian digunakan untuk mengimpal bahan tidak serupa dalam bentuk T. Pengaturcaraan Fuzzy telah dibangunkan daripada data latihan dan disahkan dengan data ujian dari keputusan ujian tarik untuk memilih parameter sesuai untuk analisis logam dan kekerasan. Pertama, aloi aluminium AA2024-O sebagai kulit dan AA7075-T6 sebagai penyambut dikimpal secara bermuka dua untuk menentukan kekuatan kimpalan. Pengaruh kelajuan laser kimpalan dan jarak focus telah dikaji untuk menentukan penusukan hasil kimpal dalam kajian ini. Penembusan penuh diperolehi pada kelajuan kimpalan 9mm/s dengan input haba yang paling tinggi 4715 J/mm , yang memerlukan 642.79N untuk meretakkan kimpalan. Analysis mikrostruktur membuktikan pembentukan saiz bijian yang kecil disebabkan oleh laser kimpalan. Bagaimanapun, kekerasan Vickers tidak meningkat menyebabkan penambahan aloi pengisi BA4047 di antara aloi aluminum untuk menilai pengaruh aloi pengisi kepada sifat-sifat mekanikal. Bagi parameter yang sama, daya patah dan kekerasan Vickers meningkat kira-kira 300 % dan 1200% masing-masing apabila aloi pengisi ditambah. Kimpalan laser bermuka tunggal mempunyai kelebihan untuk bahagian yang tidak boleh diakses. Aloi titanium, Ti6Al4V sebagai kulit dan nikel aloi, Inconel 600 sebagai

penyambut dikaji untuk penyambung-T dengan menggunakan teknik yang sama. Faktor pertindihan dan kelajuan kimpalan telah digunakan dalam kajian ini dan kesan telah diperiksa. Daya maksimum, 150N diperlukan untuk patahkan kimpalan sampel apabila faktor bertindih adalah 50% dan kelajuan kimpalan adalah 40 mm/s pada kuasa 250W. Mikrokekerasan meningkat 200% berbanding dengan logam biasa dengan pembentukan sebation antara logam, NiTi dan $NiTi_2$ di zon pelakuran hasil daripada analisis Spektroskopi serakan tenaga sinar-X dan pembelauan sinar-X. Secara keseluruhan, kimpalan laser sisi dan tunggal boleh dilakukan dengan menggunakan laser serat kuasa rendah untuk membentuk kimpalan.

ACKNOWLEDGEMENTS

This study is dedicated to the memories of my late father, Mr. P.Janasekaran Palaniandy (2011), my mother in law, Mrs. Mangadath Vijayalakshmi (2012) and my father in law, Mr. Vijayasree Madhavan (2013).

With thanks and love,

Shamini P. Janasekaran,

August, 2017

TABLE OF CONTENTS

LIST OF FIGURES

LIST OF TABLES

LIST OF SYMBOLS AND ABBREVIATIONS

3D	:	Three-dimensional
AC	:	Alternating current
BM	:	Base metal
CO_2	:	Carbon dioxide
CW	:	Continuous wave
DC	:	Direct current
$d\gamma/dT$	:	temperature coefficient of surface tension
EDS	:	Energy Dispersive X-Ray Spectroscopy
FZ	:	Fusion zone
GMAW	:	Gas metal arc welding
GTAW	:	Gas tungsten arc welding
HAZ	:	Heat-affected zones
LASER	:	Light amplification by stimulated emission of radiation
LBW	:	Laser beam welding
MIG	:	Metal inert gas
OM	:	Optical microscope
SEM	:	Scanning electron microscope
SiC	:	Silicon carbide
SMAW	:	Shielded metal arc welding
TIG	:	Tungsten inert gas
XRD	:	X-ray diffraction
κ	:	thermal conductivity

CHAPTER 1: INTRODUCTION

1.1   Background of study

Welding is a flexible and sensible fusion joining method applied in the majority of the industrial field. Contemporary welding techniques include arc welding, such as tungsten inert gas (TIG) welding and metal inert gas (MIG) welding. Laser beam welding (LBW) is an advanced process of welding materials using a high-energy laser beam. Laser welding can be categorized as deep or shallow penetration depending on weld application (Katayama, 2013). LBW technology offers exceptional precision owing to the high speed, small heat input and great seam depth. As a high-intensity laser beam hits the surface of most metals, a vaporized capillary called a keyhole forms (Y. Zhang et al., 2008). LBW has been used in the metal industry at a rapidly increasing rate for the following reasons (Reutzel, 2009) (Simeon & Vadim, 2013) (Elijah Kannatey-Asibu, 2009):

a) Deep penetration welding with keyhole mode for thick substrates using a single pass leads to fewer chances of defects.

b) The low heat input reduces distortion and improves the metallurgical microstructure in the heat-affected and fusion zones.

c) Inaccessible areas of high thermal conductivity or high melting point metals can be welded.

Welding dissimilar metals is important in many industrial applications. However, conventional welding methods, such as TIG and MIG welding have many drawbacks that have lead industry experts to feel reluctant to practice them. In the TIG welding technique non-consumable electrode tungsten is primarily used in welding, but this calls

for tremendous skill and patience to obtain good finishing. The MIG welding technique has been automated such that minimally trained welders are sufficient, but MIG cannot be used to fabricate thin flanges (Vince, 2015). Once laser welding was introduced, many industries have been motivated by the possibility of laser welding, although this technique is initially high-cost. The higher the maximum output power, the higher the initial cost is (Huntress, 2015). Investment in high-power laser welding needs the involvement of huge industries, whereas small upcoming industries cannot participate. Table 1.1 shows estimated cost and time for low power fiber laser and TIG welding (Miller, 2004) for 100000 samples.

Table 1.1: Estimation cost and time for fiber laser welding and TIG welding

	Fiber laser	TIG welding
Initial cost (300W)	RM300,000.00	RM2,000.00
Installation	RM150,000.00	RM200.00
Consumable - shielding gas (50 samples)	RM250.00	RM250.00
Electricity (50 samples)	RM0.20	RM0.20
Maintenance (50 samples)	RM0.00	RM500.00
Investment	RM450,000.00	RM2,200.00
Cost/sample	RM5.00	RM15.00
Cost for 100000 samples	RM500,400.00	RM1,500,400.00
Welding Time/sample	1s	5s

[1]

Therefore, a low-power laser welding technique has been introduced and studied in detail for initial cost and time reduction. New studies have also been done to improve the joining of thinner alloys through laser welding. Besides, it seems difficult to weld the T-joint configuration with conventional methods, so laser beam welding (LBW) has been applied to weld joints to evaluate their weldability. Double-sided LBW was proposed to improve production efficiency and to reduce the overall weight. LBW can

---

[1] Assuming samples size 20*20*1mm, Shielding gas used is Argon gas , Price referred to year 2015, Welding speed 20mm/s

replace mechanical fastening because it provides high-energy density, high welding speed, greater flexibility in welding complex shapes with narrow heat-affected zones (HAZ) and high depth-to-width ratio. In cases where accessibility to the joining surfaces is limited, single-sided joining can be employed. Single-sided LBW can be used to weld areas with limited accessibility, although the resulting weld will be prone to cracking due to asymmetric forces (Daneshpour et al., 2009; Zain-ul-Abdein et al., 2009). Therefore, these factors are taken into account and a detailed study is done from preliminary testing through to a comprehensive analysis.

1.2   Importance of study

The importance of this study is in finding an alternative method of welding dissimilar metals in the T-joint configuration. Many earlier studies have focused on using high-power laser to weld materials, and in the current study, materials with similar thicknesses are welded using lower-power fiber laser. Fiber laser is a new type of laser that has penetrated the research area for betterment (Okhotnikov, 2012). This technique takes less time to weld metals, resulting in fast production and higher profit overall (Kurakake et al., 2013).

1.3   Problem statement

Joining dissimilar metals has difficulties due to differences in thermal stress and formation of intermetallic compounds during joining that might lead to brittle joints. Besides that, thermal expansion mismatch during joining tends to give difficulties to get sound joint. However, it is important that these problems are addressed and solved for applications that needs properties from both dissimilar metals are being joined successfully. Weight increment is the biggest concern and laser welding can join two

parts into one. Yet, high power laser welding is expensive and low power is definitely a better choice.

1.4   Research motivation

For many decades, welding was used to join similar or dissimilar materials into single pieces with zero or few defects. In mechanical joining, adhesives, rivets, screws, bolts and nuts were used. The greatest motivation for this research is that mechanical joining methods are not suitable since their strength is lower than fusion joining as in laser welding. Besides, the addition of rivets, screws, bolts and nuts accumulates unwanted joint material weight. Laser welding can reduce the time for joining each workpiece more than mechanical bonding.

1.5   Research objectives

The aim of this research is to develop a method of T-joint configuration with low power fiber laser welding that can reduce the time at the same time increased quality and quantity. The initial experiments involved low melting temperature alloys (aluminum alloys) and were extended with the addition of filler for improvement purposes. The next stage was to initiate low-power fiber laser welding of a new combination of high-temperature precious metals (Ti6Al4V and Inconel 600). The specific research objectives are as follows:

i.   To evaluate the effects of laser welding parameters on mechanical properties and microstructural analysis for successive double-sided laser welding of AA2024-O and AA7075-T6 without and with filler

ii.   To determine the effects of laser welding parameters on mechanical properties and microstructural analysis for single-sided laser welding Ti6Al4V and Inconel 600.

iii.   To predict the range of parameters through fuzzy logic for dissimilar metals laser welding.

1.6   Scope of research and limitations

The novelty of this research is to weld dissimilar materials specifically metals in a T-joint configuration using a low-power fiber laser. The maximum power of the laser machine is 300 W and recommended to use up to 90% of the maximum value. Part I consists of successive double-sided laser welding between aluminum alloys, AA2024-O and AA7075-T6 in T-joint configuration. Both sides are laser welding using without any filler alloys. Argon gas is used as shielding gas to protect the welding areas. Part II consists of successive double-sided laser welding between AA2024-O and AA7075-T6 in T-joint configuration with filler, BA4047 addition. Shielding gas in not necessary as the flux inside the filler alloy can protect the welding areas. Part III comprises of single-sided laser welding between titanium based alloy, Ti6Al4V and nickel based alloy, Inconel 600 in T-joint configuration. No filler alloys were used and inert gas, Argon gas was used as shielding gas to protect the laser irradiated area.

1.7   Structure of thesis

This thesis consists of 5 chapters: introduction, literature review, methodology, results and discussion, and conclusions and recommendations. A summary of each chapter is given below.

Chapter 1 presents a background of previous studies and their importance, especially regarding laser welding of complex configurations. The importance of the current research is noted with convincing research objectives. The research scope and problems are explained as well.

Chapter 2 documents a complete literature review of joining technologies in general and more specifically welding techniques that compromise between conventional and contemporary methods. Next, the parameters influencing joining and defects that can occur during laser welding are discussed in detail. Lastly, details of the bonding strength in the fusion and heat-affected zones conclude the chapter. Fuzzy logic and its fundamentals are discussed at the end of the chapter.

Chapter 3 explains in detail each experimental method applied throughout the research. The materials, equipment and testing machines used are also elaborated. The development of fuzzy expert smart model for each study was explained in detail.

Chapter 4 presents the experimental results with a full analysis and discussion in each sub-section. Preliminary tests were done for all experiments and the fuzzy logic method was used to select a range of parameters for mechanical studies and microstructural analysis through the pull test results. Experimental and prediction data were compared to choose suitable parameters for the remainder of the study. The results are expressed openly and each part of the experiments is explained clearly.

Chapter 5 concludes with the overall research findings and recommendations for future work.

CHAPTER 2: LITERATURE REVIEW

2.1 Welding techniques

In a weld, separate material pieces are joined and combined into one piece during high-temperature heating. In certain cases, filler materials are added to strengthen the material properties of the joint. Welding is used extensively in all manufacturing sectors. Conventional welding is a permanent joining method for typically similar materials. However, advanced welding techniques have been adapted to join dissimilar materials (Weman, 2003). Figure 2.1 shows the conventional and advanced joining techniques in the welding category.
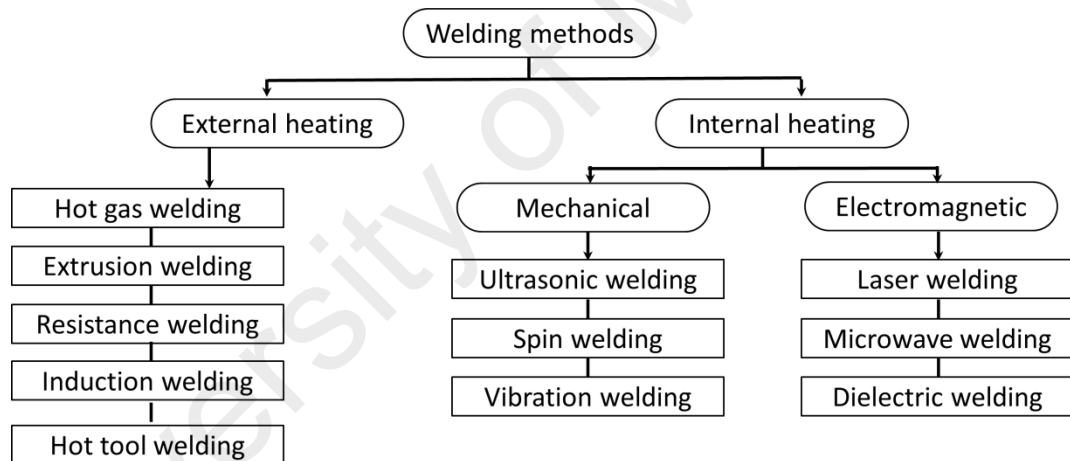
Figure 2.1: Typical welding methods in current manufacturing sectors (Weman, 2003)

Welding process selection depends on several criteria, such as equipment availability, weld quality, weld joint application, required persistence, accuracy, workpiece location, material type, welding time, the joint's cosmetic appearance, operator's skills, material size, overall cost, and design and specification requirements.

2.1.1   Conventional and contemporary methods

Common conventional joining methods include arc and gas welding. Arc welding involves an electric arc between the electrode and base material to melt the metal and accomplish welding. The power supply can be alternating current (AC) or direct current (DC). The most popular types of arc welding are shielded metal arc welding (SMAW), gas tungsten arc welding (GTAW) and gas metal arc welding (GMAW) (Weman, 2003). SMAW is a process in which a flux-covered metal electrode carries the electrical current that jumps from the electrode to the workpiece. The electric arc creates heat to melt both the base material and electrode. The molten pools from the base material and electrode mix together, and once the arc is removed, the molten pool solidifies. The electrodes resemble sticks, hence this type of welding is also called stick welding. As a precaution, the molten pool is protected by fumes coating the melting electrodes. SMAW is among the most popular and oldest methods that yield welds of sensible quality. It is cost-effective, flexible and versatile, but also has disadvantages such as huge smoke production, the need for post weld heat treatment as well as high skills for persistent quality welding. In GMAW, an arc is produced between the base metal and the continuous wire elecrode, where the thin wire is fed at continuous speed to melt the electrode. Shielding gas is necessary because the molten metal is sensitive to the open environment, for which reason this technique is also called metal inert gas (MIG) welding. The weldments are contamination-free and corrosive resistant because the filler alloy and base metal are normally made from the same alloy. Although the skill levels needed to operate this technique are not as high as for SMAW, some skill level is still required to ensure sound weld production. In GTAW, a tungsten electrode and filler wire are used with good shielding to avoid oxidation during welding. The tungsten electrode does not melt, whereas the filler wire that is manually fed into the pool melts and solidifies in an inert environment. This technique is comparetively cleaner than

SMAW and GMAW, yet slower. In the gas welding technique, a high-temperature flame is focused by gas combustion to melt the filler and base metal together (Weman, 2003).

Resistance welding, energy beam welding and solid state welding are non-conventional contemporary methods. Resistance between the metal surface contacts caused by heat generated from high current (up to 100 000 A) is simply called resistance welding. This eventually creates a molten pool in the welded area. Spot welding and seam welding are examples of resistance welding techniques. Energy beam welding, which includes laser beam welding, is a method of melting and joining workpieces. Meanwhile, in solid state welding, such as ultrasonic welding, explosion welding, roll welding, friction stir welding and pulse welding, the joining materials do not melt (Tomashchuk et al., 2015; L. J. Zhang et al., 2015)

2.1.2   Introduction to laser welding

LASER is an acronym for Light Amplification by Stimulated Emission of Radiation. Laser essentially entails a convergent, coherent, monochromatic beam of electromagnetic radiation with wavelengths varying from ultraviolet to infrared. In almost every field of electronics, engineering, medicine and dentistry, the application of lasers has become highly dominant and important (Dahotre & Harimkar, 2008). Generally, lasers can be used for laser surface treatment, surface melting, alloying, cladding, welding, material removal, hole drilling, cutting, scribing, and marking.

2.1.3   Laser welding configuration

Several common workpiece configurations for joining two materials are explained in this section. In any configuration, either with mechanical or physical bonding, pieces

must fit tightly in order for joining to happen. The gap should be as small as possible. When heat is present during joining in laser or arc welding, the molten materials must be able to move, flow and mix. A pointer in each configuration indicates the direction, which will be explained further (see Figure 2.2). A blue arrow indicates that heat is neither applied nor generated while bonding occurs, while a red arrow indicates some heat is present along the joint line during bonding, namely welding.

A butt joint also known as a seam joint shown in Figure 2.2(a) is made of two materials with either similar or dissimilar edges that are fitted together. The materials can normally be fitted with screws or bolts and nuts to keep them together. Adhesive can also be applied on the material surfaces to attach them for bonding, which is called mechanical bonding. During physical bonding, the touching line between both materials undergoes physical bonding with the help of joining techniques, such as brazing, welding and soldering. Brian Anthony Graville patented butt joining in 1976 and defined a method of joining two adjacent plates with the advantage of heat treating the HAZ on the parent material. Butt joining includes single pass welding, whereby the gap is cut in the center of the first weld, leaving the first weld material and re-welding the gap between the two adjoining surfaces. An advantage of this method is that adverse metallurgical effects on the primary metal are avoided (Graville, 1976).

Meanwhile, a lap joint as shown in Figure 2.2(b) can be made of fully or half-overlapping materials meant to be joined or fastened to produce one continuous surface (Mifflin, 2011). The materials can have similar or dissimilar sizes and properties with an interface area between different materials. John J. Marko from General Motors Corporation patented lap joint welding using a conventional method in 1980. The invention involves a welded lap joint between two metal sheets (John J. Marko, 1980). Initially in 1914, Carl Bartel from the United States patented the edge joint as a plate-

edge joint, as shown in Figure 2.2(c). This invention refers to joining plate edges mainly in burglarproof constructions. The initial method entailed grinding and no screws (Bartels, 1914). Figure 2.2(d) shows the T-joint configuration and it is elaborated in detail in the following sub-section.
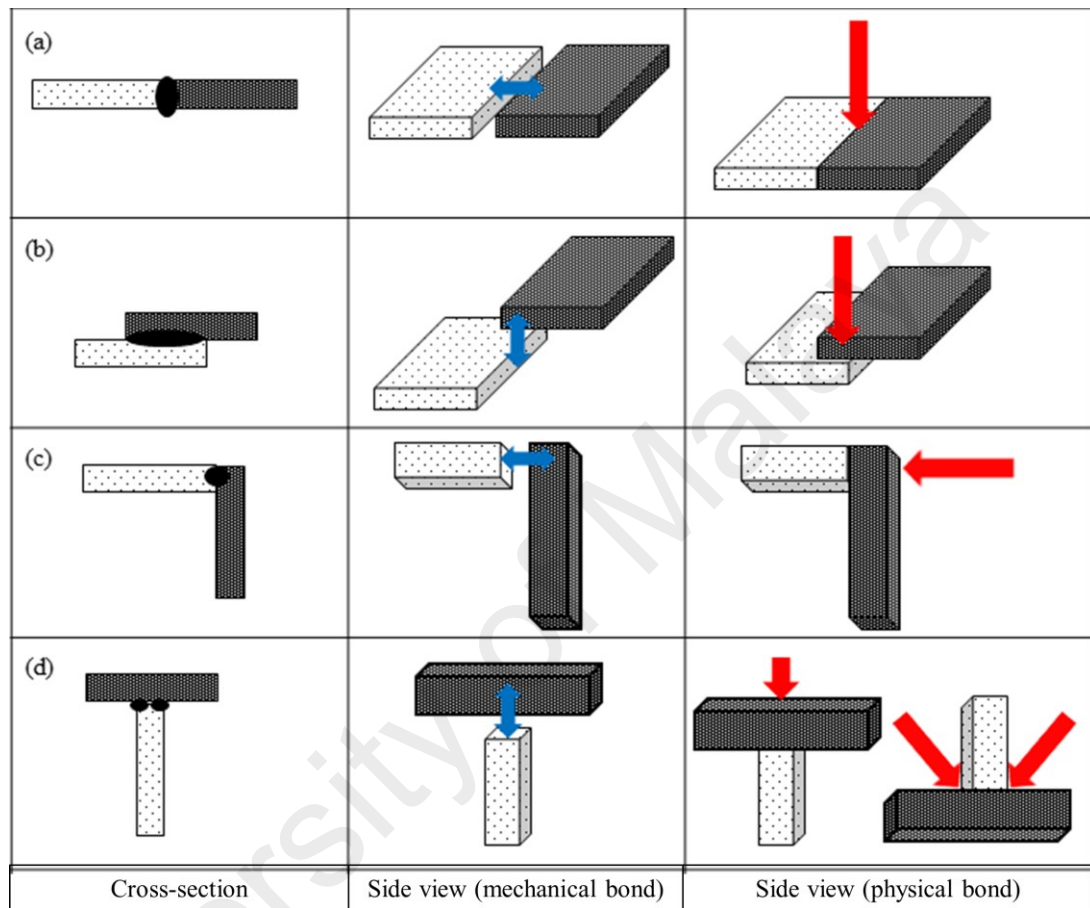
Figure 2.2: Bonding and welding configurations with red arrows indicating the laser beam direction: a) butt or seam joint, b) lap joint, c) edge joint, d) T-joint

2.1.3.1 T-joint configuration

A T-joint is a complex profile consisting of skins and stringers (as shown in Figure 2.3) that is often used in structured flying bodies and the fabrication industry, including steel bridges, pressure vessels, ships and offshore structures. Laser beam welding of T-joints has been studied and used in industry. The T-joint configuration also plays an important role in the transportation industry where components and panels often need to be joined. Such parts normally go through heavy-duty vibration during their lifespan

11

and must be fatigue resistant (Fratini et al., 2006). The T-joint profile has a couple of critical features that require attention, which are the stiffness and skin strength without significant weight increment (Tavares et al., 2009). Skin and stringer sheets placed in T-joints are vital to achieving good joining. The conventional method of joining this pattern is to use rivets in a mechanical process with the possibility for automation. However, extra rivets add to the total weight and this has led to seeking opportunities to eliminate the use of rivets or mechanical joining (A. C. Oliveira et al., 2015).

Double-sided laser beam welding with the T-joint configuration entails the beam angle, beam separation distance and incident beam as the parameters affecting the T-joint's metallurgical quality (Tao et al., 2013). In situations of limited accessibility where only one-side joining is possible, this T-joint configuration for a single side is very helpful. The weld beads along the skin-stringer components influence the joint's mechanical strength. Excessive penetration into the skin can lead to stress concentration, thus increasing the chances of cracks especially in the HAZ. Therefore, the melt region must not exceed 30% of the skin thickness and single-sided welding is one way to lower the penetration depth of the weld bead into the skin. Less heat input accumulates when only one laser runs on the joint, which decreases distortion. However, laser alignment must be ensured to avoid welding defects (Prisco et al., 2008).
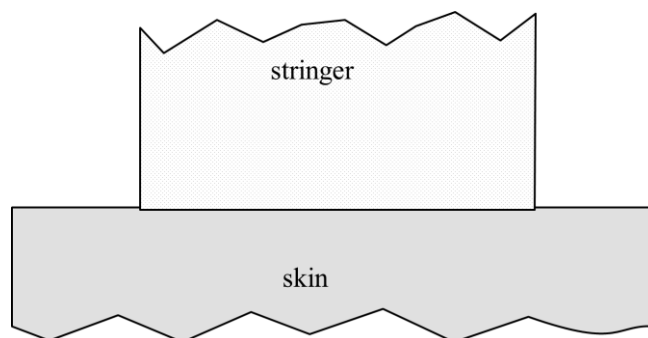
Figure 2.3: Schematic drawing of T-joint

T-joints are normally applied to customized clamping fixtures in order to retain the position between the skin and stringer and preserve a precise shape. Researchers who have investigated welded T-joints found that fatigue failure in structures is due to stress concentrators, which are also the ideal points for crack initiation (Carpinteri et al., 2004). Corrosion properties have also been studied in detail to maximize the lifespan of T-joints (Padovani et al., 2007). Zhao et al. (2014) applied the friction stir welding technique to join aluminum alloys using the T-joint configuration. They identified that T-joint fracturing along the skin is caused by the mating bond and tunnel defects that contribute to the tensile properties (Zhao et al., 2014).

To date, laser welding and friction stir welding are two alternative modern methods of joining series AA2XXX and AA7XXX aluminum alloys. Friction stir welding is based on the friction in the thermo-mechanically plasticized zone in the welded materials. This technique reduces porosity formation and the risk of hot cracking. Nevertheless, this technique requires expensive equipment and is used for joining simple configurations. Therefore, laser beam welding is a better choice for complex configurations. With the fusion welding method, porosity and hot cracking occur as a result of solidification shrinkage and thermal stress differences. However, these drawbacks can be overcome with a protected environment and good control of the laser welding parameters, particularly for 2000 and 7000 series aluminum alloys (Badini et al., 2009). Meanwhile, welding nickel and titanium base alloys in the T-joint configuration is of great importance in the aerospace industry as well as racing car exhaust systems.

2.2   Laser beam welding

Laser beam welding (LBW) is a non-contact process that requires access to the weld seam from one side to another side of the welded part. The intense laser light rapidly

(normally in milliseconds) heats the material to form a weld joint. LBW is divided into continuous wave (CW) and pulsed laser welding. CW can be either on or off and uses average power, while pulsed laser creates welds by individual pulses and utilizes high peak power. Hence, pulsed laser takes less energy to create a weld with a smaller heat-affected zone, unrivalled spot welding performance and minimal heat input seam welding (Hitz et al., 2012). During LBW, a molten pool forms in the joint area. Energy is absorbed when a laser beam irradiates the material surface, which causes material heating and melting or sometimes evaporation, depending on how much heat input has been absorbed. Compared with conventional welding, LBW has special advantages, such as micro welding, the possibility to weld dissimilar and difficult to weld materials, high welding speed, precise welding, a narrow HAZ and quality welding, and is also economical for larger production volumes. However, there are some limitations with workpiece thickness and laser welding speed (Dahotre & Harimkar, 2008). When two or more materials are placed together to be welded, closely fitting and well-clamped joints are necessary because the small focused spot of the laser beam will pass through a narrow gap. If the parts fit poorly, filler wires are used to overcome undercuts. The position of the beam is very important, because a narrow weld can be missed if the beam is not positioned accurately. The depth of the focused beam is small and in order to achieve the required power density, it should be positioned at the correct work surface. The laser gun should be fixed according to safety guidelines to ensure the operators are safe during operation. The equipment and operating costs are high because laser welding requires detailed work handling and the ancillary equipment is expensive. Therefore, the laser needs to be highly utilized to be cost effective and cover the purchase cost (Dawes, 1992).

A part, or a defined region of a part is heated by laser radiation through the sample component that should be joined. The part is held under mechanical pressure and is

heated, and a stable positive bond will be achieved during cooling if suitable component geometry is selected. LBW takes place when the workpiece melts after exceeding its liquidus temperature. Heat resistance analysis is essential to determine the amount of energy density that will permit attaining the heating stage rapidly. In the early experimental series, the influence of the surface structure on the joining process is examined. The main aim of the experiments is to evaluate the most adequate joining parameters that give the joints additional mechanical strength (Holtkamp et al., 2010). Figure 2.4 displays a schematic diagram of laser welding.
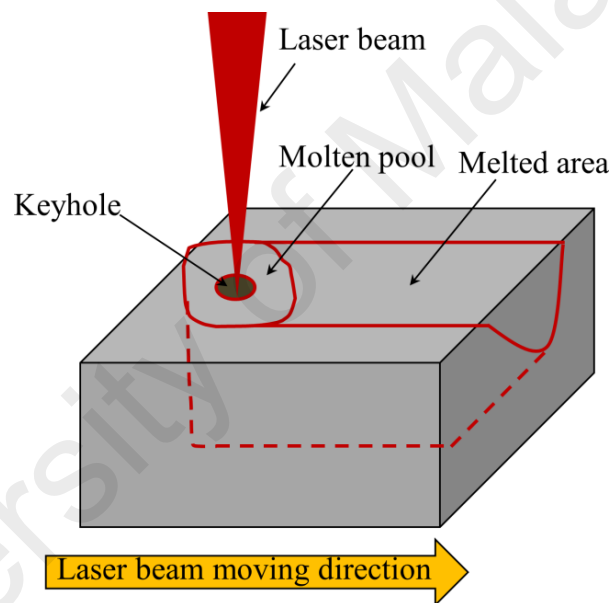
Figure 2.4: Schematic drawing of laser welding

Replacing conventional welding with LBW has many advantages, some of which are summarized below (Reutzel, 2009); (Simeon & Vadim, 2013); (Elijah Kannatey-Asibu, 2009; Moraitis & Labeas, 2008):

a) The ability to perform deep penetration welding in keyhole mode for thick substrates using a single pass, leading to fewer chances of defects.

b) Controlled beam energy that provides low heat input, which results in reduced

15

distortion.

c) Low heat input control that can improve the metallurgical microstructure in the heat-affected and fusion zones, leading to enhanced mechanical properties.

d) Non-contact welding through space and heat source dissipation to manipulate the welding torches.

e) Large working distances available to enable handling inaccessible parts and complicated joint geometries.

f) High power density ensures high heating rates, facilitating welding of metals with high thermal conductivity or high melting points.

g) High depth-to-width ratio ranging from 3:1 to 10:1.

h) The laser beam is not affected by magnetic fields or passing through air, therefore vacuum condition is not required and no radiation is generated.

i) Smaller heat affected zones, residual stress and strains.

However, one of the disadvantages of LBW is the high capital investment for the setup. Besides, fast cooling due to high-speed laser can result in centerline cracking, hot cracking and the formation of brittle and non-ductile solidification structures. Safety issues also make it difficult to handle by manual or portable means (Reutzel, 2009).

2.2.1   Types of laser

Generally, lasers are classified into four types subject to the physical nature of the active medium used, namely solid-state laser, gas laser, dye laser and semiconductor laser. Common solid-state lasers are Nd:YAG, Ruby and Er:YAG, whereas CO_2 laser is mainly a gas laser. Dye and semiconductor lasers have been used less in recent research. Fiber laser technology has matured and evolved remarkably during the last few decades. Fiber laser is a new type of laser used by modern research groups. This is a guided-

wave system that prevents induced thermal lensing constraints (Okhotnikov, 2012). There are several types of laser used for welding, each with different characteristics. Table 2.1 presents a detailed list of laser types (Katayama, 2013).

Table 2.1: Types of laser used for welding and characteristics

Laser type	Wavelength (μm)	Laser medium	Power
CO_2	10.6	CO_2-N_2-He mixed gas	CW: 50kW max
Lamp pumped YAG	1.06	Nd^{3+}:$Y_3Al_5O_{12}$ garnet solid	CW: 10kW max
Diode	0.8-1.1	InGaAsP solid	10kW max (stack type) 15kW max (fiber-delivery)
Diode pumped solid state	1	Nd^{3+}:$Y_3Al_5O_{12}$ garnet solid	CW: 13.5kW max (fiber-delivery) PW: 6 kW max (slab)
Disk	1.03	Yb^{3+}:YAG or YVO_4	CW: 16kW max (cascade)
Fiber	1.07	Yb^{3+}:SiO_2 (solid)	CW: 100 kW max (fiber)

2.2.2 Conduction and keyhole laser welding

There are two methods of laser welding: conduction welding and keyhole welding (deep penetration). Overall, the heat conduction and convection in the weld pool determine the penetration depth. In conduction welding the weld pool surface is unbroken, whereas in the latter method the laser process creates a "keyhole" in the weld pool. Incrementing the laser power intensity or irradiation time results in the transition from conduction mode to keyhole welding (Dahotre & Harimkar, 2008). Figure 2.5 shows the schematic differences between conduction and keyhole welding. In conduction welding, the heat from the laser beam is absorbed by the workpiece's top surface. Steady state condition is reached rapidly and the heat loss is balanced by

conduction. Thermal conduction and surface-tension-driven fluid flow determine the weld's aspect ratio. With decreasing temperature the surface tension decreases, leading to an outward flow of molten metal. Deep penetration welding occurs when the high energy density laser beam vaporizes the workpiece. The keyhole that forms allows the laser beam to penetrate deeper into the metal, producing a narrow melt pool. Upon keyhole formation, laser beam absorption increases as multiple reflections occur in the hole until the heat is absorbed by the metal. A keyhole cavity is formed when the beam intensity is sufficient, which can fill with gas or vapor from the continuous material evaporation (Walsh, 2002).
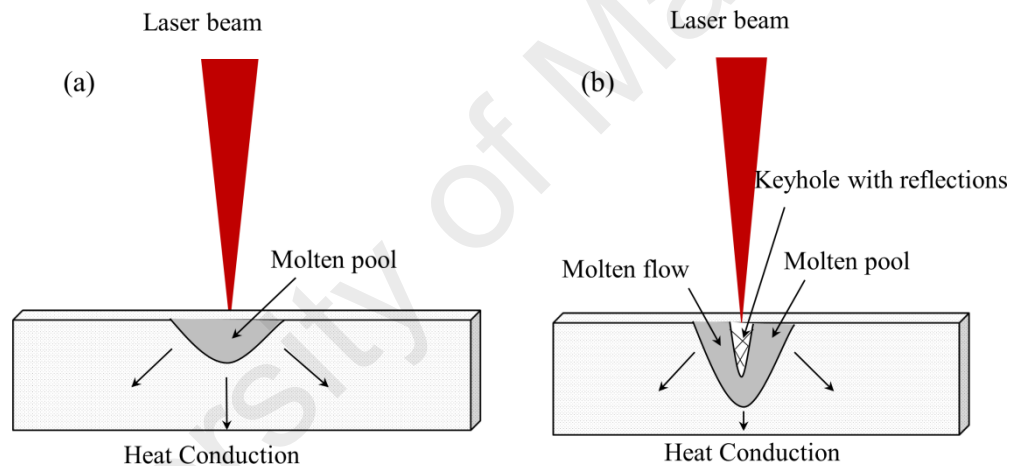
Figure 2.5: Schematic cross sections of two different types of welding;
(a) Conduction welding (b) Keyhole welding

2.2.3 Dissimilar materials

Welding dissimilar materials is highly challenging due to the differences between the materials' physical and chemical properties. The formation of an intermetallic brittle phase in the weldment causes degradation of the material's mechanical properties. Despite material dissimilarities, such welding is gradually becoming hugely demanded by industries owing to advantages such as improved and customized designs as well as material reduction (Dahotre & Harimkar, 2008). In the current era, welding dissimilar

18

materials has gained popularity and attention from various industries. Besides reducing material costs, designers can enhance and customize product designs. However, due to differences between chemical and physical properties, brittle phases, cracks and residual stresses occur in dissimilar material welds (Sun & Ion, 1995). Theoretically, any materials that can be joined by conventional methods can also be joined using laser. Nonetheless, the weldability of dissimilar materials depends on several parameters. Chemical and physical properties have a vital role in the manipulation of energy and heat transfer in the weld (Klages et al., 2003). Table 2.2 shows the weldability of metal pairs. Solid solubility is important for good joints in dissimilar material welding.

Metals within compatible melting temperature ranges can achieve good weldability, but if one metal has a melting point at the vaporization temperature of the other material, then poor weldability is obtained and brittle intermetallic layers will form. However, the formation of intermetallic layers during laser welding of dissimilar materials can be reduced to a certain extent since the weld zone is narrow. The composition that results in alloys is also significant in such formation. Even though molten metals mix during laser welding, chemically homogeneous fused zones are rarely achieved. Hence, local heterogeneity can lead to the presence of a brittle zone. Researchers have found that controlling the heat input can soundly reduce the formation of brittle intermetallic phases in dissimilar materials. The higher laser power with higher welding speed combination improves the weldment in aluminum-magnesium and steel-aluminum joints (Schubert et al., 2001).

Table 2.2: Weldability of metal pairs (Katayama, 2013)[2]

	Al	Ag	Au	Cu	Pt	Ni	Fe	Ti	W
Al	-	C	X	C	X	X	X	X	X
Ag	C	-	S	C	S	C	D	C	D
Au	X	S	-	S	S	S	C	X	N
Cu	C	C	S	-	S	S	C	X	D
Pt	X	S	S	S	-	S	S	X	X
Ni	X	C	S	S	S	-	C	X	X
Fe	X	D	C	C	S	C	-	X	X
Ti	X	C	X	X	X	X	X	-	X
W	X	D	N	D	X	X	X	X	-

Controlling the heat input can minimize the reactive interlayers' thicknesses. This would also eliminate the brittle intermetallic phase formation in laser welding of steel-kovar, aluminum-copper and steel-copper (Mai & Spowage, 2004). Applying a backing block under the welding samples is another alternative for controlling the heat flow and reducing the intermetallic layer thickness in dissimilar materials (Borrisutthekula et al., 2007). Dissimilarities in metal welding are divided into two types. First, there are dissimilarities in thermo-physical properties, such as thermal conductivity (κ) and the temperature coefficient of surface tension ($d\gamma/dT$). Conductivity differences indirectly influence the weld composition, leading to asymmetric heat transport. The weld's geometry pattern is dictated by the differences in $d\gamma/dT$, which influences the molten pool's surface tension. The second type of dissimilarity is inhomogeneous molten flow, which leads to the formation of different crystal phases due to metallurgical differences (Chatterjee et al., 2008). Dissimilar metal welding differs from similar metal welding in terms of the presence of intermetallic layers. Therefore, welding such materials is a big concern on account of their weldability. The formation of intermetallic phases is a common problem in thermal joining of dissimilar materials. The main concern here is

---

[2] Al: Aluminum, Ag: Silver, Au: Gold, Cu: Copper, Pt: Platinum, Ni: Nickel, Fe: Iron, Ti: Titanium, W: Tungsten

C: Complex structure possibility, X: Intermetallic compound might form, S: Solid solubility, D: Insufficient data, N: No data

that intermetallic phases can be extremely hard, which can cause brittleness and diminish joint usage (Schubert et al., 2001).

Using Nd:Yag and CO_2 laser for dissimilar materials is common, but the use of fiber laser is increasing slowly for dissimilar materials, such as aluminum alloy with carbon steel (Ozaki & Kutsuna, 2009) and steel with titanium alloy (S. J. Park, 2008). Fiber laser is comparatively more advantageous for dissimilar material welding. The most outstanding advantage is the beam quality and possibility to have a small focus diameter, which yields high power density at the workpiece, reduced heat input, smaller heat-affected zone and shorter cycle time (Klages et al., 2003). Badini et al. (2009) researched aluminum alloys AA7XXX and AA2139 when using two continuous wave Nd:YAG lasers with 4kW power and argon mixed with helium as shielding gas in the T-joint configuration. They used Al-Si filler alloy to improve the weldability of the laser welded joint (Badini et al., 2009). With this addition, the filler alloy actually increased the overall cost. Other studies were done with AA6XXX and AA4XXX using filler wire. High power 15kW CO_2 continuous wave laser welding and 3kW Nd:YAG laser were used for simultaneous welding and it was concluded that the welding parameters greatly affect the weld's macrostructure (Li et al., 2011). Dissimilar materials generally have different thermal stress properties, which directly affect any joining process where heat is applied. This type of joining can be complicated and involves bonding through the intermetallic layers that are present during bonding interaction.

2.3   Parameters influencing laser welding

In laser welding, many process parameters need cautious consideration to achieve higher success rates. The success rate of laser welding depends on the appropriate use of various parameters. Many researchers have investigated parameters that influence laser

welding. Researchers from India have proven that laser beam power and welding speed are the major process parameters influencing penetration depth and bead width. Also, an acceptable weld joint is determined by its quality and efficiency. Tensile and weld joint properties were found to be interrelated with the weld joint's microstructure (Balasubramanian et al., 2010). Codigo Do Trabalho (2009) investigated the influence of the weld joint gap when using Nd:Yag laser on stainless steel. It was concluded that butt joint welds are dependent on laser beam diameter, welding speed, duty cycle and material thickness. Thus, butt joints are sensitive to the gap and have strict tolerance (Trabalho, 2009). Researchers from the Georgia Institute of Technology, Atlanta, reported that the HAZ generated by laser heating of steel at various laser scanning speeds changes the microstructure and micro-hardness (Singh et al., 2008). Masoumi et al. (2010) found that the effective pulse energy is the controlling factor of weld joint strength according to an investigation of the effect of frequency pulse, laser energy and welding speed (Masoumi et al., 2010). Paleocrassas (2009) considered laser power, welding speed and focal distance in calculating the weld energy per weld length. They defined the optimum welding speed is between 2 and 3 mm/s for maximum penetration of 1.02 mm (Paleocrassas, 2009). Another finding is that increasing the incident angle decreases the bead length and increases the depth penetration and bead width (Liao & Yu, 2007). Meanwhile, researchers from Pisa, Italy, concluded that the depth of penetration is directly proportional to welding speed, where bead width decreases and depth/width ratio increases with increasing welding speed (Khan et al., 2011). The effects of rising temperature and power density on the workpiece are dependent on various parameters, as explained further subsequently.

2.3.1 Power density and heat input

Equations 2.1-2.5 show the heat input and power density calculations (Nelson & Crist, 2012); (Saleh & Teich, 1991). Accordingly, when the beam diameter decreases, the molten metal flows deeper and faster (Walsh, 2002).

$$\text{Heat Input} = \frac{\text{Power Density}}{\text{Speed}} \qquad\qquad (\text{Eq. 2.1})$$

$$\text{Power Density}, P_d = \frac{\text{Power}}{\text{Spot Area}} = \frac{P}{\pi r^2}, r = W_z \qquad\qquad (\text{Eq. 2.2})$$

$$W_z = W_O \sqrt{1 + \left(\frac{Z}{Z_R}\right)^2}, Z = \Delta FD \qquad\qquad (\text{Eq. 2.3})$$

$$Z_R = \frac{\pi W_O{}^2}{\lambda} \qquad\qquad (\text{Eq. 2.4})$$

$$D = 2W_O = \frac{4\lambda}{\pi}\left(\frac{F_O}{\emptyset_i}\right) M^2 \qquad\qquad (\text{Eq. 2.5})$$

Where λ = laser wavelength, F_O = optimum working distance, M^2 = beam quality factor, W_O = beam waist, FD = focal distance, r = laser beam radius and θ_i = fiber laser input diameter, Z_R = focused focal length and W_Z = laser diameter

2.3.2 Continuous laser power

Increasing the laser beam power allows the fluid to flow faster but shallower (Walsh, 2002). Laser power is measured in Watts (either in nW, mW, W or kW) and refers to the optical power at the laser beam output. The output is classified into continuous wave (CW) or average pulsed (modulated) as shown in Figure 2.6.
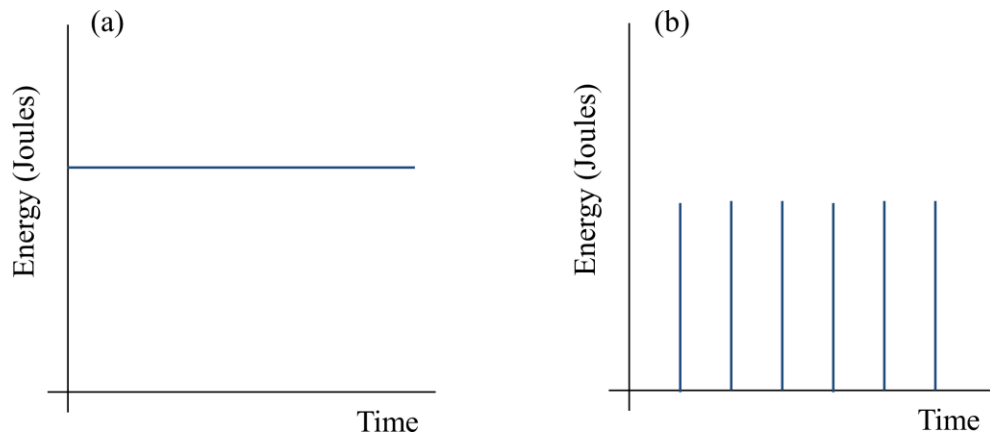
Figure 2.6: a) Continuous wave laser output, b) Average pulsed laser output

2.3.3   Welding speed

As laser welding speed changes, the pool flow pattern and size vary accordingly. At lower speed the pool is large while at higher speed the pool is small. However, slower speed can result in defects like dropout. When welding speed is low, conduction loss occurs through the large base metal. Besides, the vapor cavity also tends to decline, producing less penetration. Welding speed influences the shape and quality of the weld. With increasing speed, welding mode changes from deep penetration to conduction welding. Low speed will cause deeper penetration as the weld pool is deep and narrow, while at high welding speed the keyhole is unstable and penetration is non-uniform (Walsh, 2002).

2.3.4 M^2, the laser beam quality factor

M^2 is a laser's deviation till reaching contiguity with a perfect Gaussian beam. A purely fundamental TEM000 mode structure describes a purely fundamental theoretical beam width that is multiplied to determine the actual beam width. M^2 of 1.0 represents a laser that produces a fundamental mode beam and M^2 is determined through a process

of beam size measurements along the beam path. This process of determining M^2 cannot always be intuitive but may require mapping the beam's propagation in space (Peterman, 2005). M^2 can be defined as the laser beam quality factor.

2.3.5 Rayleigh length to define the focal distance
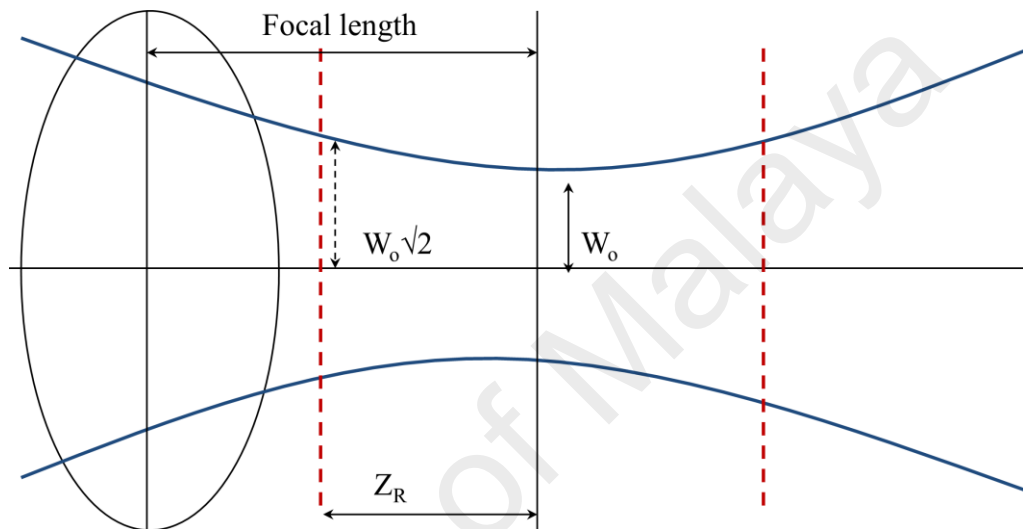
Figure 2.7: The Rayleigh length range of a Gaussian beam

Figure 2.7 shows the Rayleigh length range of a Gaussian beam that used to calculate the focal length. W_O denotes the beam waist radius. The minimum value of W_O is assumed in the plane when z=0 (Saleh & Teich, 1991). The Rayleigh range denoted by Z_R is defined as the distance over the beam radius spreads by a factor of $\sqrt{2}$. The focal length calculated is the range within focus and other ranges are out of focus (Griot, 2009); (Damask, 2005); (Renk, 2012).

2.3.6   Shielding gas

Shielding gas has an important role in laser welding, whereby the gas protects the weld keyhole and molten metal from oxidation, thus helping to avoid porosity. Moreover, shielding gas can protect the laser beam transmission to ensure good weld penetration by minimizing beam expansion and scattering (Dawes, 1992). A small amount of oxygen in the air is enough to oxidize the alloying elements and produce defects. In hot melting, the nitrogen gas from air can be trapped during solidification, leading to brittleness and pore formation. Argon (Ar) gas is the most popular shielding gas due to its properties as an inert gas that has no chemical interactions with other materials. It is suitable for selective materials such as aluminum and stainless steel. Helium (He) is another inert gas like argon that provides more heat input for joining. It can increase the welding speed and facilitate greater penetration for thick materials. However, He is expensive and low-density; therefore carbon dioxide (CO_2) is used for cost savings. CO_2 is safer compared to Ar gas, but it produces large amounts of spatter, which is a drawback of using it fully. Hydrogen (H_2) is sometimes added to increase the heat input and welding speed but poses risk of cracks and can be only used for austenitic stainless steel (Weman, 2003).

2.3.7   Absorption and reflection

During laser contact absorption is a common occurrence, which affects the efficiency and reliability of a process. For opaque materials, reflectivity related to absorptivity is given by the following equation:

$$A = 1 - R$$ (Eq. 2.6)

Reflectivity increases with increasing wavelength, therefore materials with higher wavelengths are considered strong absorbers. This can serve only as guidance, as other factors such as radiation incident angle and the surface condition influence the absorptivity. Another important point to note is that highly reflective materials at low temperatures become highly absorptive at higher temperatures. This principle applies for laser welding, whereby laser can be used even in case of high reflectivity. For Ytterbium fiber laser with 1070 nm wavelength the mean absorptivity is approximately 0.4, but this value varies with laser parameters and surface quality (Yanga et al., 2010); (Dahotre & Harimkar, 2008). However, the material and surface properties can determine the amount of power absorbed (Walsh, 2002).

2.3.8   Overlapping factor

The laser beam overlapping factor also has a significant role in determining the weld joint, particularly for low power laser. The figure below shows the differences between with and without the overlapping factor. For example, when the laser beam spot diameter is set to 0.3 mm and the overlapping factor is 10%, the pitch between the horizontal and vertical spots is:

$$\text{Pitch} = 0.3 - (10\% \text{ of } 0.3)$$

$$= 0.27 \text{ mm}$$

To simply Equation 2.2, assume the laser diameter is 1 mm, therefore the reciprocal of the area will be 127 cm^{-2}.

$$P_d = \frac{\text{Power}}{\text{Spot Area}} = \frac{P}{\pi(0.05^2)\text{cm}} = 127 \text{ x P Wcm}^{-2} \qquad \text{(Eq. 2.7)}$$

According to Equation 2.7, if the laser beam diameter is 2 mm the power density will drop by 4, while if the laser beam diameter is 0.5 mm the power density will increase by 4. Hence, for an arbitrary laser beam size, the formula is stated in Equation 2.8:

$$P_d = 127 \text{x} \frac{\text{Power}}{d^2} \qquad \text{(Eq. 2.8)}$$

For a Gaussian beam profile the beam is uniform and the formula (Equation 2.9) is multiplied by 2, resulting in:
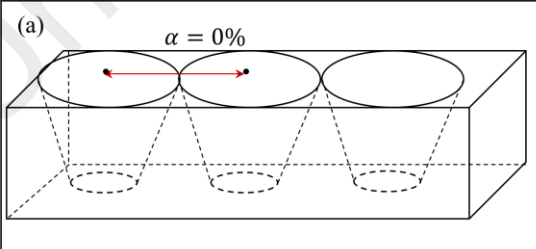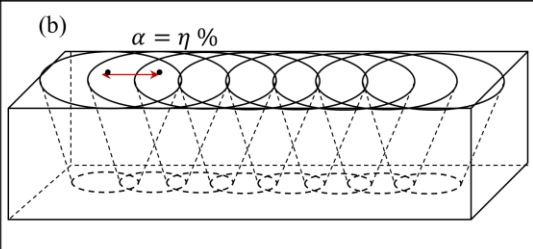
$$P_d = 255 \text{x} \frac{\text{Power}}{d^2} \qquad \text{(Eq. 2.9)}$$

By allowing ~2% error for the power density calculation since the difference is trivial, 250 is used for easy calculation. Therefore, the simplified formula is (Spectra-Physics, 2011):

$$P_d = \text{Power x} \frac{250}{d^2} \qquad \text{(Eq. 2.10)}$$

In this case, the power density with and without the overlapping factor is shown below. Assuming the power is 100 W and the pitch (laser beam diameter) is given, the power density is calculated as per Table 2.3.

Table 2.3: Differences from the overlapping factor denoted as 10%

(a) $\alpha = 0\%$	(b) $\alpha = \eta\ \%$
Without overlapping factor	Laser beam overlapping factor denoted by η
Pitch = 0.3 mm	Pitch = 0.27 mm
$P_d = \text{Power x} \frac{250}{d^2} = 100 \text{ x } \frac{250}{0.3^2} = 278 \text{kW/cm}^2$	$P_d = \text{Power x} \frac{250}{d^2} = 100 \text{ x } \frac{250}{0.27^2} = 343 \text{kW/cm}^2$

According to the above calculation, the power density increases at a point being hit by a laser beam when the overlapping factor increases. Besides, the focused laser beam diameter also has a vital role in determining the power density, as seen in the above equations. A smaller laser beam diameter gives relatively higher power density. From the equations, we can conclude that greater power gives higher power density and lower welding speed, and inversely gives greater heat input. Laser power is one of the main parameters that determine the type of machine and its capability of welding certain materials. Therefore, the overall heat input related to laser power, welding speed and overlapping factor is simplified in Equation 2.11.

$$\text{Heat Input} = \frac{P}{\pi\left(\frac{d-\eta}{2}\right)^2 \cdot v} \tag{Eq. 2.11}$$

Where P = laser power, v = welding speed, d = beam diameter, η = overlapping factor

2.4   Laser welding defects

Due to the mismatch of the thermal coefficient and residual stress between materials, a few types of defects can occur. Some welding defects are lack of fusion within the weld, porosity, cracks, burns, undercutting, oxidation, humping, blowholes, dropout and spatter.

2.4.1   Undercutting and dropout

Dropout, as shown in Figure 2.8, happens when the ferrostatic head is too large for the surface tension to keep the molten pool at the same level. At higher speed, however, a strong flow moves towards the weld center where the keyhole did not have sufficient time to redistribute, thus resulting in freezing at the central ridge, which is called an

undercut (Steen & Mazumder, 2010). Undercutting is a loss of material due to splattering and evaporation. Undercuts are observed when the laser power is too high, which leads to liquid material loss from the weld pool. Furthermore, undercuts can also happen when the gap between the joints are big, but this can be prevented by using a proper clamping system (Katayama, 2013).
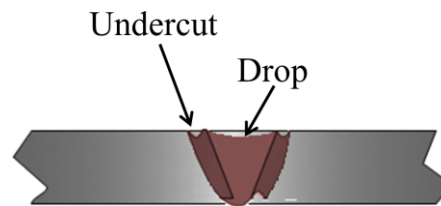
Figure 2.8: Undercut and dropout defects after welding

2.4.2   Cracks

A notable type of crack is hydrogen cracking (cold cracking), which takes place during welding of carbon steels and high-strength low-alloy steels (Figure 2.9). However, hydrogen cracking does not occur in aluminum but hot cracking does. This type of cracking is a mechanism known to occur when hot shortness, solidification or liquation cracking, or hot fissuring happens. This phenomenon can be reduced or eliminated by manipulating the welding parameters (Katayama, 2013).
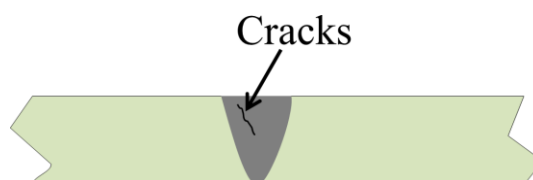
Figure 2.9: Cracks in the weld zone

2.4.3 Porosity and blowholes

A defect that is quite prominent is porosity, which entails the rapid closing of the keyhole that leads to inhibited full penetration. Pores (Figure 2.10) are left in the weld zone due to rapid cooling when the solidifying pool traps the pores before they are released to the surface. Shielding gas is mostly used to protect the weld surface from oxidation and contamination to prevent porosity, but it can also contribute to porosity when gas is trapped by the turbulent welding pool and keyhole (Katayama, 2013). Blowholes are similar to pores and appear on top of weld beads due to keyhole instability, normally at high welding speeds (Walsh, 2002).
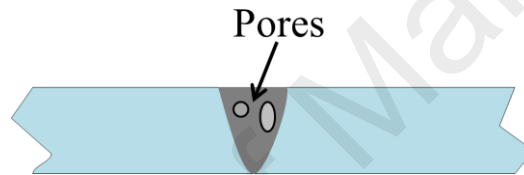
Figure 2.10: Pore defects produced during laser welding

2.4.4 Humping

Humping is a longitudinal weld defect, whereby a hump forms above the weld zone surface level. It is not necessary for full penetration to happen for this defect to occur (Walsh, 2002).

2.4.5 Non-uniformity and surface roughness

Non-uniformity and surface roughness (normally on the micron scale) are sometimes classified as defects. When laser power increases, the weld bead roughness is less noticeable compared to lower laser power. Roughness is also considered less compared

to when low laser power is applied. Meanwhile, lower power indicates instability in the weld pool thermodynamics, which leads to a rapid increase in roughness (Walsh, 2002).

2.4.6   Weld spatter

Weld spatter happens when molten metal droplets are thrown out from the fusion zone. This situation can be handled by reducing the peak power and weld temperature. However, such reduction can also decrease the weld penetration (Walsh, 2002).

2.5   Difficulties in joining dissimilar metals in T-joint configuration

Many industries seek dissimilar metal welding to maximize the production of customized, attractive designs and for weight manipulation. Welding dissimilar materials provides more flexibility to obtain various commercial designs (Harwani, 2014). Such designs can be expensive due to the techniques used and considerations for sound joints (Guo et al., 2014). There is increasing demand for dissimilar materials to create new component functions in various industrial fields, but this is problematic due to the high reliability on strength (Kurakake et al., 2013).

The conventional means of joining the T-configuration is to use rivets with mechanical methods with the possibility for automation. However, adding rivets increases the total weight, which has led to seeking opportunities to eliminate the use of rivets or mechanical joining (A. C. Oliveira et al., 2015). Critical features of the T-joint configuration that require attention include its stiffness and the skin's strength with no significant weight increment (Tavares et al., 2009). Laser beam welding of the T-joint configuration has been studied and often used in industries. The T-joint configuration has important roles in the transportation industry in terms of joining certain vehicle

components and panels. These parts normally undergo heavy-duty vibration during their lifespan and must therefore be fatigue resistant (Fratini et al., 2009). T-joints are normally added to custom clamping fixtures in order to retain the position between the skin and stringer to maintain and preserve precise shapes. Single-sided laser welding is preferred when only one mating side is visible. However, this technique leads to insufficient or excessive penetration, which has encouraged seeking other laser welding techniques (Ventzke et al., 2014). Shanmugan et al. (2010) and Machold et al. (2008) concluded that during single-sided T-joint welding there is non-uniform temperature distribution (Machold et al., 2008; Shanmugam et al., 2010). The aircraft industry has approved both successive and simultaneous double-sided laser beam welding of T-joints as methods for joining skin stringers. This is because symmetric weld seams with fewer defects can be obtained (Enz et al., 2015; Enz et al., 2012; Prisco et al., 2008; Yang et al., 2012). Therefore, low-power fiber laser is used on the T-joint configuration in this study to overcome the drawbacks of other welding techniques.

Nonetheless, most existing studies have focused either on the butt joint or lap joint configuration rather than the T-joint profile, which is also an important configuration in aircraft fuselage manufacturing and the automobile industry. In aircraft fuselage manufacturing, riveting is the dominant technology for joining aluminum alloy skin-stringer joints and the conventional riveting process is usually done in T-joint welding. However, the main drawbacks are low productivity and high cost owing to high residual stress, significant distortion and metallurgical defects that arise during conventional riveting. To address these limitations, laser welding is proposed as an alternative to the riveting process, especially for the T-joint configuration. Aluminum alloy T-weld configuration joining has increased for automotive, railway vehicle, bridge, fuel storage and flying structures. Nickel-based alloys, however, are widely employed for high-temperature applications in aero engines, race car exhaust systems and gas turbines

owing to the thermal fatigue resistance and excellent oxidation resistance characteristics (Shokrani et al., 2012). Meanwhile, titanium alloys are widely used in the aerospace, exhaust system and biomedicine fields (Shen et al., 2015) due to multiple advantages, such as light weight, biocompatibility, toughness, corrosion resistance, high strength-to-weight ratio and high yield stress (Chen et al., 2011). The skin and stringer formed in a T-joint is a complex profile, and metal welded joints are utilized in the fabrication industry. However, T-joint welding defects can occur more easily than in other simple configurations like butt or lap joints, leading to the necessity for advanced joining techniques (Acerra et al., 2010; Xu et al., 2013).

2.6 Bonding strength

This section presents in detail the materials used throughout the research. After heating and cooling, the behavior and microstructure of each alloy differs according to the time taken for the process, which will be explained comprehensively in the next section. The weld pool hardness is normally greater than that of the original base metal due to the changes in microstructure, precipitate formation and intermetallic products (Walsh, 2002).

2.6.1 Fusion zone

The fusion zone (FZ) is a region where the base metal actually melts and the fusion zone depth is the distance over which the fusion extends into the base metal. The workpiece mechanical properties and metallurgical elements change in the fusion zone. The fusion zone's depth-to-width ratio, porosity and cooling rate during the laser beam welding process vary with laser beam power, focal distance and welding speed (Lee et al., 1996).

2.6.2 Heat-affected zone

The heat-affected zone (HAZ) is denoted as the area of the base material that can be either thermoplastic or metal and is not fully melted but is affected by the laser heat. However, the initial properties and microstructure are altered due to the welding effect or intensive heat supply. During the welding process, heating followed by cooling causes weld interface changes to terminate the temperature in the base material. The base material and filler metal properties influence the HAZ properties following heat application. At the same time, the amount of heat input during laser welding and time taken for welding also impact the HAZ. When the thermal diffusivity of the base metal is high, the material cooling rate is also high, leading to relatively smaller HAZ and vice versa. Laser welding involves highly concentrated, limited amounts of heat, which leads to a small HAZ (Weman, 2003).

2.7 Fuzzy logic fundamentals

In 1965, mathematician Lotfi Aliasker Zadeh developed the mathematical theory of fuzzy sets based on a Boolean logic extension. The classical set theory was generalized by introducing the notion of degrees in any condition. This enables conditions that can be in any state other than true of false, making way for inaccuracies and uncertainties. The rules are set in a common language and justification is not needed when using the probabilistic concept (Rojas, 2013; Ross, 2009; Zadeh, 1996). The fuzzy system is summarized in Figure 2.11. A fuzzy system generally reflects human interpretation.
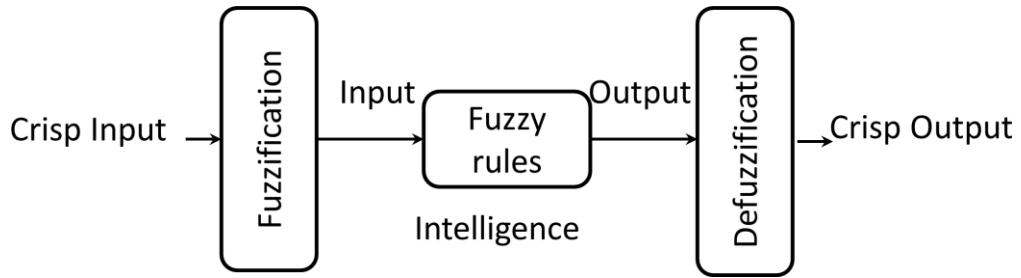
Figure 2.11: Simplified overall fuzzy system

2.7.1 Fuzzy sets and membership functions

Crisp sets allow full or no membership, while fuzzy sets allow partial membership. The crisp set, membership and no membership of element x in set A are described in Equation 2.12. A few types of membership are associated with fuzzy sets, such as triangular, Gaussian curve, trapezoidal, bell-shaped, polynomial curve and sigmoid function. Equations 2.13 and 2.14 represent triangular and trapezoidal memberships respectively (Kumar et al., 2014).

$$y_A(x) = \begin{cases} 1; x \in A \\ 0; x \notin A \end{cases} \qquad \text{(Eq. 2.12)}$$

$$y_A(x) = \begin{cases} \dfrac{x-a}{b-a}, & a \leq x \leq b \\ \dfrac{c-x}{c-b}, & b \leq x \leq c \\ 0 & \text{otherwise} \end{cases} \qquad \text{(Eq. 2.13)}$$

$$y_A(x) = \begin{cases} \dfrac{x-a}{b-a}, & a \leq x \leq b \\ 1, & b \leq x \leq c \\ \dfrac{d-x}{d-c}, & c \leq x \leq d \\ 0 & \text{otherwise} \end{cases} \qquad \text{(Eq. 2.14)}$$

Fuzzy logic is based on the fuzzy set theory while crisp logic is based on the crisp set theory. Figure 2.12 briefly explains the theory of crisp logic, which is a subset of fuzzy logic.
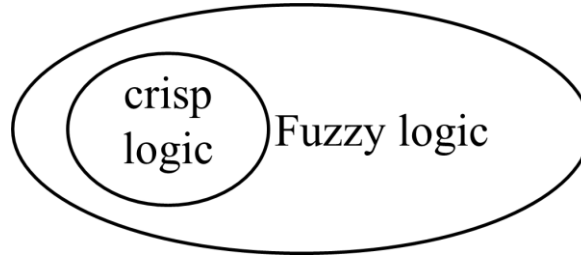
Figure 2.12: Crisp logic is subset to Fuzzy logic (Dernoncourt, 2011)

2.7.2 Logical operations

Fuzzy logic has its own logical operations, with differences in the membership of variables from an ordinary logic extension. Fuzzy logic can be divided into propositional and predicate logic and has several more advantages than ordinary logic. Examples of fuzzy propositional logic are monoidal t-norm, Godel fuzzy logic, product fuzzy logic and rational Pavelka logic, while predicate logic is extended from propositional logic by adding universal and existential quantifiers. Some simple fuzzy operators are shown in Equations 2.15, 2.16 and 2.17 (Zadeh, 1996).

$$\text{NOT } X = 1 - \mu_x(y) \tag{Eq.2.15}$$

$$X \text{ OR } Y = \max(\mu_x(y), \mu_y(y)) \tag{Eq.2.16}$$

$$X \text{ AND } Y = \min(\mu_x(y), \mu_y(y)) \tag{Eq.2.17}$$

2.7.3 Fuzzy inference system – Fuzzification

During fuzzification, the input comprises linguistic values represented by degrees of membership in the fuzzy set. Therefore, the measured numerical values are translated into fuzzy linguistic values, a process simply called fuzzification (Dernoncourt, 2011).

2.7.4 Defuzzification

After fuzzification, the fuzzy system designer will carry out defuzzification using all fuzzy operators. Common methods used include the mean of maxima (MeOM) and center of gravity (COG) methods. Defuzzification is a process where quantifiable results are produced from the fuzzy inference in terms of degrees of membership. The membership degrees are interpreted into specific actions or real values (Dernoncourt, 2011).

2.8 Materials selection

The following subsections describe the materials used in the experiments. The materials used throughout the studies are aluminum, titanium and nickel alloys.

2.8.1 Aluminum alloys

Aluminum alloys are made up of alloying elements such as copper, manganese, magnesium, zinc and silicon. The weight of each element determines the final form. These alloys are categorized into wrought alloys and cast alloys. Wrought alloys are further classified into age-hardenable alloys and non-age hardenable alloys. The nomenclature used to identify these alloys consists of four digits starting from 2000

series to 8000 series which the naming according to International Alloy Designation System, IADS. The 2000 and 7000 series aluminum alloys are both age-hardenable, with the 2000 series having copper element as the main alloying element whereas the 7000 series alloy has magnesium and zinc as the deciding elements. Age hardening is an effective method in hardening mechanism process. Additional codes added at the back of the name indicate any heat treatment process the alloys have gone through. For example, "O" denotes annealed has low strength requirement and T6 means the alloy is treated and artificially aged with optimum strength (Grote & Antonsson, 2009).

Aluminum alloys are highly weld resistant due to their high conductivity and the presence of tenacious high resistance oxide films. Therefore, adequate surface preparations to produce consistent contact resistance should be taken into consideration (Gale & Totemeier, 2004). Table 2.4 shows the chemical composition of aluminum alloys, AA2024-O and AA7075-T6 (from Energy Dispersive X-Ray Spectroscopy (EDX) analysis).

Table 2.4: Chemical composition of Aluminum alloys (mass fraction, %)

Element		Cu	Mg	Mn	Fe	Zn	Cr	Al
Weight (%)	**AA2024-O**	2.9	2.0	0.4	0.3	1.2	0.1	Balance
	AA7075-T6	1.5	5.5	0.7	0.7	9.7	0.5	Balance

Aluminum is an effective substitution solid solution strengthener. The important properties of both the alloys have been characterized and included in software simulation databases. They are presented in Table 2.5.

**Table 2.5: Physical properties of Aluminum alloys (Grote & Antonsson, 2009);
(Gale & Totemeier, 2004)**

Properties	AA2024-O	AA7075-T6
Yield strength (MPa)	76	503
Yield strength (ksi)	11	73
Elongation (%)	20	11
Tensile strength (MPa)	185	572
Tensile strength (ksi)	26.8	83
Hardness (Brinell)	47	150
Density (g/cm^3) at 20°C	2.77	2.81
Liquidus temperature (°C)	638	635
Solidus temperature (°C)	502	477
Specific heat (J/kg. K) at 20°C	875	960
Thermal conductivity (W/m.K) at 20°C	190	130
Poisson's ratio	0.33	0.33
Elastic modulus (GPa)	70-80	71.7

2.8.2 Titanium alloy – Ti6Al4V

Although titanium has been used over the centuries, but it is only in the last 50 years that modern design and applications are favoring towards the material. Titanium has been chosen over other competing materials such as aluminum, superalloys and steels due to its unique density, corrosion resistance and relatively higher strength. Titanium alloys have been used widely in various industries such as biomedical, automotive and aerospace. One of the most widely used titanium alloy is the Ti6Al4V, which has a mixed alpha-beta structure class. This type of structure gives excellent combination of strength and ductility and is stronger than either the alpha or beta individually.

Table 2.6 shows the chemical composition of Ti6Al4V obtained from the EDX analysis. Aluminum is an effective substitution solid solution strengthener (Donachie, 2000). It is added to the alloy as α-phase stabilizer and hardener for its solution strengthening effect. The addition of vanadium stabilizes the ß-phase ductility, which gives hot workability of the alloy. However, machining of titanium is difficult due to its

high strength and low thermal conductivity (Yanga et al., 2010). Ti6Al4V has high

strength to density which makes it suitable for aerospace hardware especially in critical

parts in which failure can result in the loss of the entire system. Important properties of

this alloy have been characterized and are included in many software simulation

databases, as shown in Table 2.7.

Table 2.6: Chemical composition of Ti6Al4V (mass fraction, %)

Element	Ti	Al	V	Fe	N	O
Weight (%)	balance	6.5	3.7	0.2	0.02	0.1

Table 2.7: Physical properties of Ti6Al4V (Donachie, 2000)

Properties	Annealed
Yield strength (MPa)	920
Yield strength (ksi)	133
Elongation (%)	12.5
Tensile strength (MPa)	933
Tensile strength (ksi)	135
Hardness (Brinell)	350-400
Density (g/cm^3) at 20°C	4.43
Liquidus temperature (°C)	1660
Solidus temperature (°C)	1604
Specific heat (J/kg. K) at 20°C	0.5263
Thermal conductivity (W/m.K) at 20°C	6.7
Poisson's ratio	0.342
Elastic modulus (GPa)	113.8

Reaching 1000 °C, standard grade of Ti6Al4V becomes fully beta phase at 4wt% of

vanadium as shown in Figure 2.13 (Dragolich & DiMatteo, 1994; Pederson, 2002).
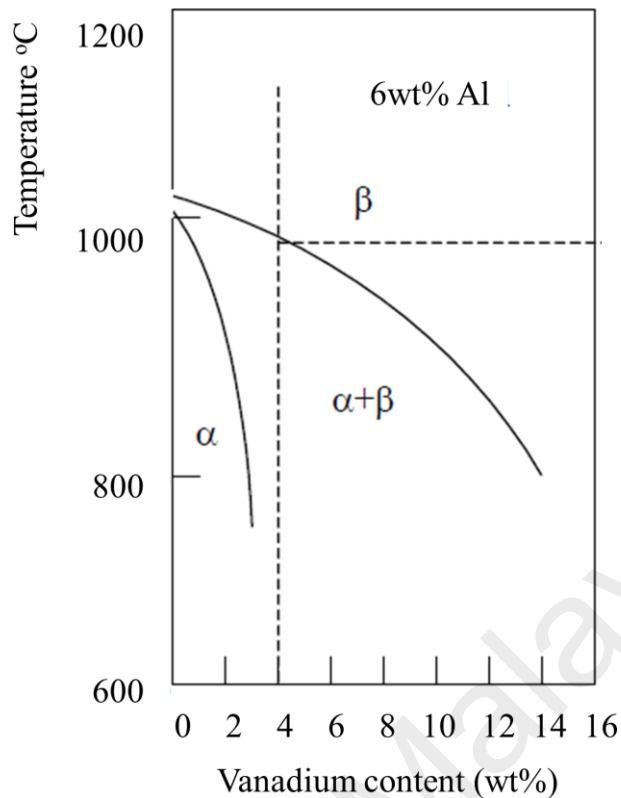
Figure 2.13: Schematic of microstructure occurring in Ti6Al4V at various temperatures (Pederson, 2002)

2.8.3 Nickel alloy – Inconel 600

Inconel 600 has a high content of nickel that provides good resistance towards corrosion in reducing conditions while the chromium content gives resistance under oxidizing conditions. It is also resistant to chloride stress corrosion cracking. Generally, Inconel 600 is used in many applications varying from cryogenic (at very low temperature) to 1000°C (high temperature). Applications that use this alloy include heat treating equipment, aircraft engines, electronics parts and nuclear reactors (Davis, 2000). The composition of Inconel 600 obtained from EDX analysis, is shown in Table 2.8 and its physical properties are listed in Table 2.9.

Table 2.8: Chemical composition of Inconel 600 (mass fraction, %)

Element	Ni+Co	Cr	Fe	C	Mn	S	Si	Cu
Weight (%)	Balance	16.64	9.3	0.02	0.26	0.001	0.15	0.09

Table 2.9: Physical properties of Inconel 600 (Davis, 2000)

Properties	Annealed
Yield strength (MPa)	199
Yield strength (ksi)	28.9
Elongation (%)	49
Tensile strength (MPa)	639
Tensile strength (ksi)	92.7
Hardness (Rockwell)	75HRB
Density (g/cm3) at 20°C	8.42
Liquidus temperature (°C)	1415
Solidus temperature (°C)	1355
Specific heat (J/kg. K) at 20°C	444
Electrical conductivity (%) at 20°C	1.7
Thermal conductivity (W/m.K) at 20°C	14.8
Poisson's ratio	0.29
Elastic modulus (GPa)	207

2.8.4   Filler alloy – BA4047-Al-12Si

BA4047-Al-12Si filler alloy is thin rolled aluminum alloy with silicon content and has a melting point of 580 °C. Table 2.10 shows the chemical composition of BA4047 from EDX analysis. Increased percentage of silicon gives improved fluidity during welding, resulting in the increase of the wettability of the filler. This filler is essential for welding seams of material, such as in the fabrication of heat exchangers. BA4047 filler alloy has reduced solidification cracking, weld leakage rates and higher shear strength in weld joint as compared to BA4043 filler alloys. However, BA4047 has a dark gray post weld appearance and is not recommended for products that required post weld surface treatment. In this research, this filler alloy is used for the double sided

joining of AA2024-0 and AA7075-T6. The as-received material, shown in Figure 2.14 has a diameter 1.2mm with the flux (Alu19FCW-Cs) inside the rod.

Figure 2.14: BA4047 used as filler alloy in joining dissimilar AA024 and AA7075

Table 2.10: Chemical composition of BA4047 (mass fraction, %)

Element	Al	Zn	Fe	Mg	Mn	Si	Cu
Weight (%)	Balance	0.2	0.3	0.05	0.8	11.8	0.15

2.9 Review of joining selected materials and application

In this section, laser welding of the materials selected for this research is discussed and elaborated.

2.9.1 Laser welding of aluminum alloys

The T-weld configuration joining of aluminum alloys is increasingly utilized in the automotive industry, and for railway vehicles, bridges, fuel storage and flying structures. The skin and stringers in the T-joint form a complex profile and welded metallurgical joints are utilized in the fabrication industry. However, welding defects in

aluminum alloy T-joint welding can occur more easily compared to other simple configurations such as butt or lap joints. Therefore, advanced joining techniques are necessary (Acerra et al., 2010; Xu et al., 2013). Significant features of the T-joint configuration are the strength and stiffness of the skin that is reinforced by the stringers without any weight increase (Tavares et al., 2009). The joining of aluminum alloys has been investigated frequently using advanced methods to achieve possibly defect-free welds, followed by numerical analyses. Some researchers have studied solid-state joining methods such as friction stir welding and simulated the material flow of T-joints based on the finite element method (Zhou et al., 2012).

In certain cases with limited accessibility, high laser power has been applied to a single side, which can reduce manufacturing efforts. Enz et al. (2015) used a high-power fiber laser of 8.0 kW on single-sided skin AA2024 and stringer AA7050 with additional filler AA4047 to weld the materials (Enz et al., 2015). However, the single-sided technique can lead to insufficient or one-sided excessive penetration, making way for finding improved laser welding techniques (Ventzke et al., 2014). In this case, either successive or simultaneous double-sided laser beam welding has been approved as a method of joining skin stringer T-joints in the aircraft industry. This is because symmetrical weld seams with fewer defects can be obtained (Enz et al., 2012; Prisco et al., 2008; Yang et al., 2012). However, most studies have been done using high-power fiber laser (Enz et al., 2015), high-power diode laser of 2.8 kW (Sanchez-Amaya, Delgado, De Damborenea, et al., 2009) and high-power diode laser between 1.5 kW and 2.75 kW (Sanchez-Amaya, Delgado, Gonzalez-Rovira, et al., 2009).

Researchers investigating welded T-joints have stated that fatigue failure in structures is due to stress concentrators, which are also the preferred points for crack initiation (Carpinteri et al., 2004). Corrosion properties also need to be studied in detail

to maximize T-joint lifespan (Padovani et al., 2007). Yong Zhao (2014) and team applied the friction stir welding technique to join aluminum alloys using the T-joint configuration. They identified that T-joint fracturing along the skin is due to the mating bond and tunnel defects that contribute to the reducing tensile properties (Zhao et al., 2014).

2.9.2   Laser welding of titanium alloy and nickel superalloys

In the automotive area, manufacturing lighter racing car parts is in high demand with the objective to achieve rapid movement. Specifically, a race car exhaust system, needs to be as light, high-strength and corrosion resistant as possible to enable fast movement during racing. Ti6Al4V and Inconel 600 are best suited for all the characteristics required of a customized exhaust system. Titanium alloy and nickel super alloys help reduce the weight of the race car through the customized design of headers and shafts (MPR., 2012). Besides race cars, titanium alloys and nickel superalloy are widely used in the aerospace industry for the superior corrosion resistance properties and high strength-to-weight ratio (Dahotre & Harimkar, 2008). However, welding these materials is a great concern on account of their weldability. Intermetallic phase formation is a common problem in welding that concerns the thermal joining of dissimilar materials. The main concern is that these phases can be extremely hard, which can lead to brittleness and decreased joint ability (Schubert et al., 2001).

Besides, dissimilar metal welding of titanium alloys and nickel-based super alloys is of particular interest in the aerospace industry because they are attractive as lightweight structural materials that help achieve high performance and efficiency. The combination of low density, high strength-to-weight ratio, excellent corrosion resistance and mechanical properties encourages the extensive usage of titanium alloys, especially

Ti6Al4V in the aerospace industry as static and rotating components in turbine engines, as well as blades and casings of compressor stages in turbojets. Meanwhile, owing to their superior mechanical properties and excellent oxidation resistance at elevated temperatures, nickel-based super alloys such as Inconel 718, Inconel 628 and Inconel 600 are also broadly employed in the aerospace industry, and are particularly suitable for manufacturing components in the high-temperature regions of aero engines and gas turbines (Chen et al., 2011). Welding alloys that contain titanium and nickel has also been studied by many groups of researchers.

Some researchers have attempted to weld titanium to nickel alloy either with or without TiNi filler. In welding titanium to nickel, weld metal grows from the base metal have been detected, with Ti_2Ni dendrites growing towards the base metal at the Ti fusion interface. Meanwhile, at the Ni side, a solid nickel solution phase appeared with additional layers of Ni_3Ti, Ni_3Ti+NiTi eutectic and NiTi (Chatterjee et al., 2006; Chatterjee et al., 2008) as shown in Figure 2.15. With higher laser power and welding speed, crack-free welds can be obtained on Ti6Al4V and Inconel 718 weld joints using 1kW fiber laser. Less hardness variation and fewer cracks are generated when the laser beam is offset at approximately 35 μm from the Inconel 718 side. This method has proven to suppress the formation of Ti-Ni intermetallic brittle phases (Chen et al., 2011).
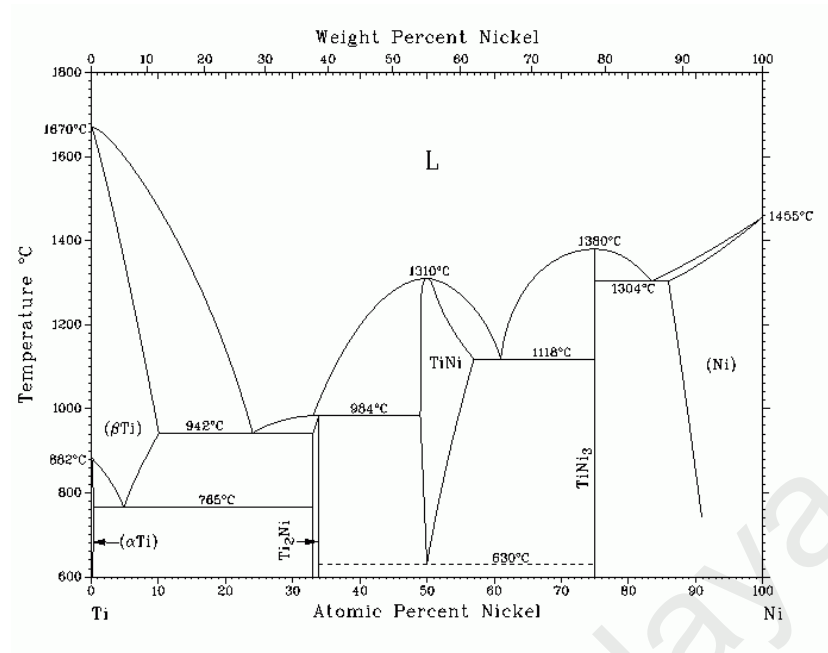
Figure 2.15: Phase diagram of Ni-Ti system

2.10 Summary

This chapter presented a literature review of conventional and contemporary (laser welding and parameters) welding methods. Two types of laser welding are conduction and keyhole welding of similar or dissimilar materials. Many parameters influence the penetration of laser welding, such as laser power, welding speed, M^2, Rayleigh length, shielding gas, overlapping factor, and workpiece's reflection, all of which contribute to the power density and heat input. Manipulating the parameters can decrease the possibility of defects in laser welding, for instance undercuts, drops, cracks, humps, pores and blowholes. During laser welding, a fusion zone is created where the laser beam hits, while the surrounding area affected by the heat from the laser is called the heat-affected zone. Fuzzy systems for prediction data analysis are used to reduce the time for preliminary testing. Finally, applications of dissimilar materials like aluminum alloys, titanium alloys and nickel-base alloys were discussed. Based on the literature review, aluminum, titanium and nickel based alloys are used in the research.

CHAPTER 3: METHODOLOGY

3.1 Introduction

This chapter describes the methodology used in this research. Figure 3.1 shows the flowchart of the experimental procedures taken.
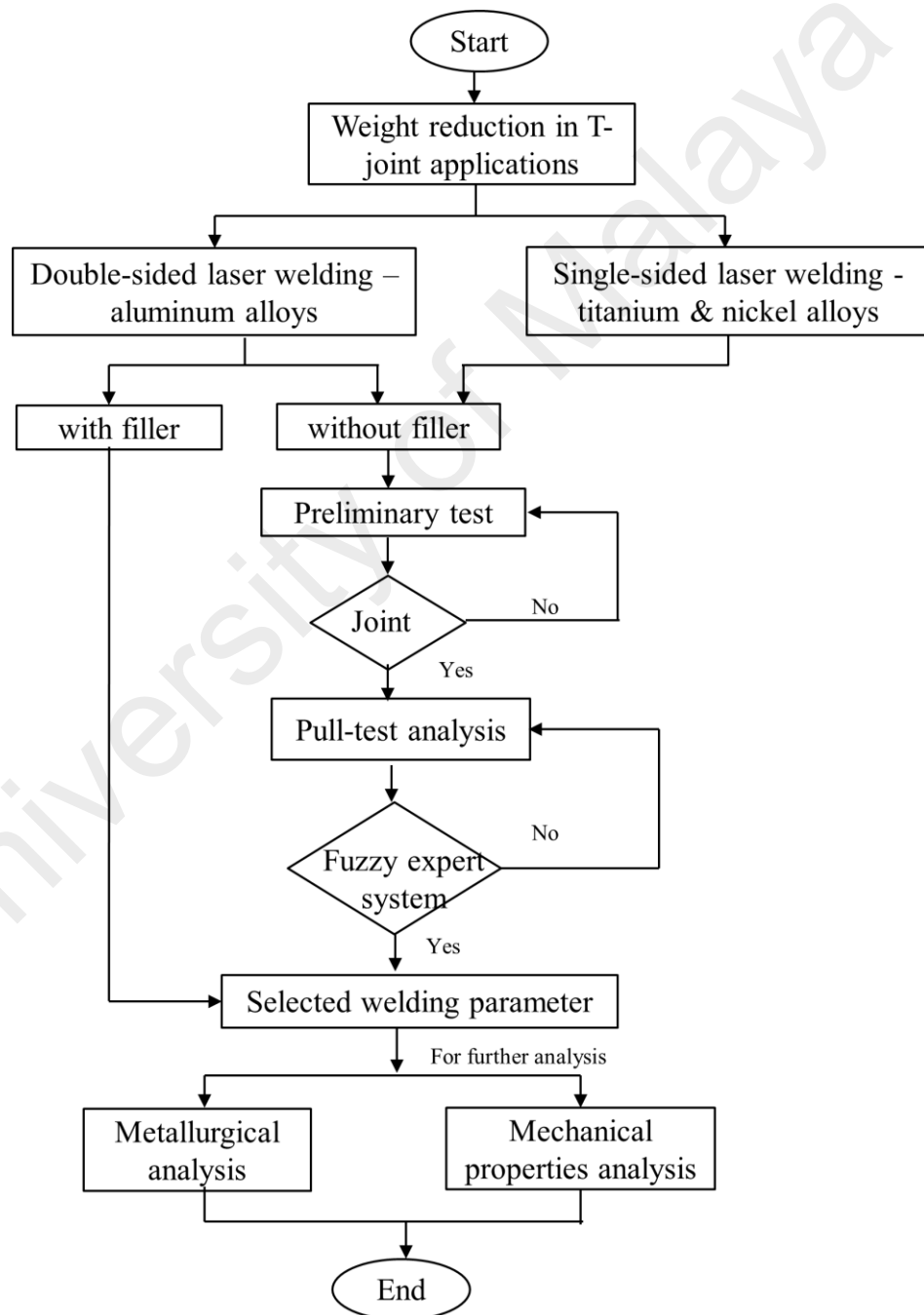
Figure 3.1: Flowchart on the experimental procedure

3.2 Experimental setup

The experimental setups for the studies are presented in the following subsections. The setup has been clearly discussed and explained in detail.

3.2.1 Sample preparations

The base metals were first mechanically polished using silicon carbide (SiC) abrasive paper (No. 600 grit size) to remove any pre-cut edges burr. Prior to laser welding, all the samples were cleaned with acetone to remove all surface contaminants. The experiments were conducted in normal atmospheric conditions with the laser scanner head fixed. The general dimensions of the prepared sample are shown in Figure 3.2.
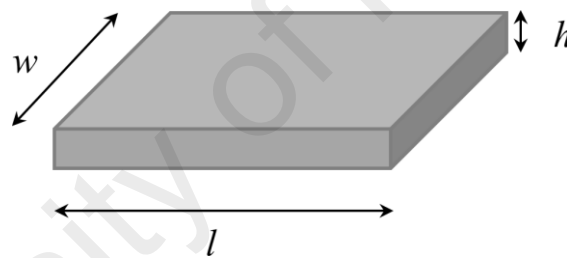
Figure 3.2: Schematic diagram of materials used for LBW

3.2.1.1 Part I: Double-sided laser welding of AA2024-O and AA7075-T6

Sheets of AA2024-O with dimensions of 20mm (*l*) x 10mm (*w*) x 3mm (*h*) as the skin and AA7075-T6 with dimensions of 20mm (*l*) x 10mm (*w*) x 2mm (*h*) as the stringer were used in this experiment. These dissimilar sheets were double sided laser welded in a T-joint configuration. The chemical compositions of AA2024-O and AA7075-T6 are described in subsection 2.8.1. The workpieces were placed at a tilted angle of 45 degree during laser welding. The laser beam with a spot diameter of 100 μm would hit, in succession, both the seams of the skin and stringer clamped with a fixture

jig in a T-joint configuration, as shown in Figure 3.3. Argon gas was used as a shielding gas to prevent oxidation of the weld surface during welding. Table 3.1 shows the welding parameters used for determining the optimized combination.
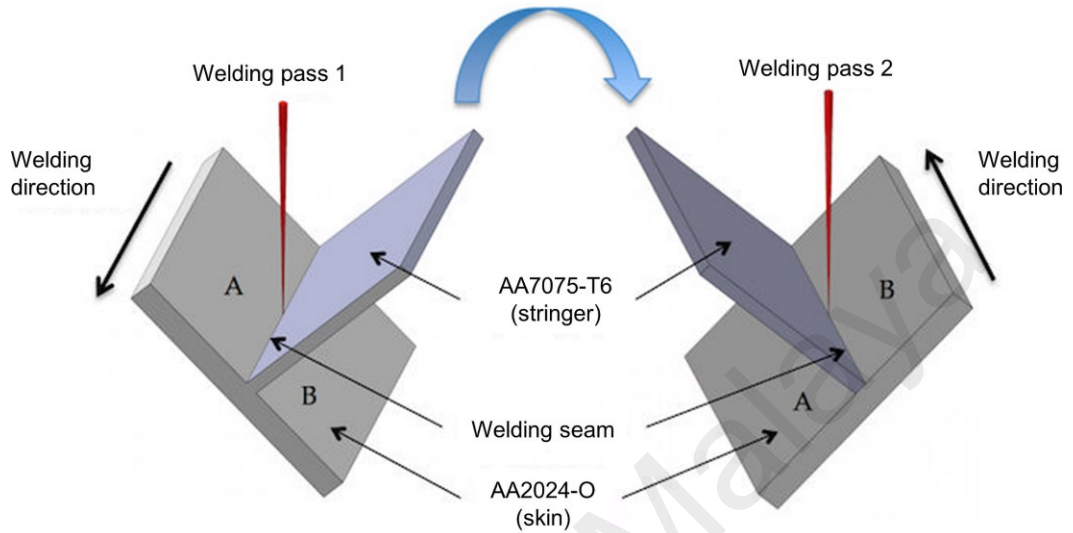
Figure 3.3: Schematic diagram of T-joint configuration using double-sided LBW

Table 3.1: Preliminary input variables and their levels used in the double-sided laser welding of AA2024-O and AA7075-T6

Laser Parameters	Level 1	Level 2	Level 3	Level 4	Level 5	Units
Laser Power: LP	250	260	270	-	-	Watt
Welding Speed: WS1	9	12	15	18	21	mm/s

3.2.1.2 Part II: Double-sided laser welding of AA2024-O and AA7075-T6 with filler alloy BA4047-Al-12Si

For the second set of experiments, sheets of AA2024-O with dimensions of 20mm (*l*) x 10mm (*w*) x 3mm (*h*) as the skin and AA7075-T6 with dimensions of 20mm (*l*) x 10mm (*w*) x 2mm (*h*) as the stringer were used with the addition of filler alloy BA4047-

Al-12Si (15mm x 1.2mm). The filler alloy is placed at both sides of the welding seam. The workpieces were tilted 45 degree and a laser beam with a spot diameter of 100 μm would successively hit the filler alloy at the seams of the skin and stringer clamped with a fixture jig in a T-joint configuration, as shown in Figure 3.4. Argon gas was not used as shielding gas since the flux inside the filler alloy would prevent oxidation of the weld surface during welding. The welding parameters used in these experiments were taken from the optimized results of Part I, and is shown in Table 3.2.
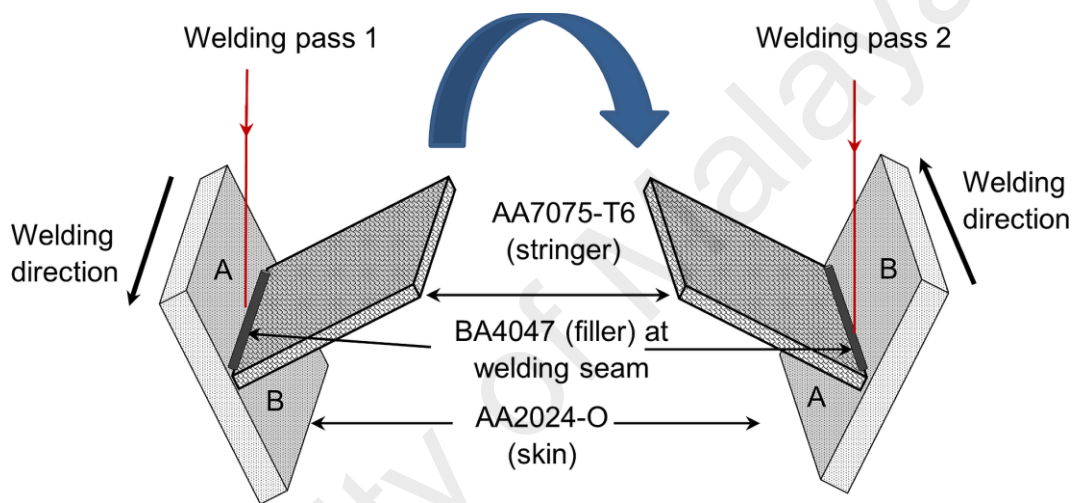
Figure 3.4: Schematic diagram of T-joint configuration using double-sided LBW with filler alloys at welding seam

Table 3.2: Laser welding parameters used in the double-sided laser welding of AA2024-O and AA7075-T6 with filler alloy BA4047

Parameters	Settings
Laser Power	270W
Welding speed	9,12,15,18 and 21 mm/s
Filler addition	BA4047

3.2.1.3 Part III: Single-sided laser welding of Ti6Al4V and Inconel 600

In this study, Inconel 600 sheets with dimensions of 20mm (*l*) x 20mm (*w*) x 1mm (*h*) were used as the stringer and Ti6Al4V sheets with dimensions of 20mm (*l*) x 20mm

(*w*) x 0.5mm (*h*) were used as the skin. The chemical composition of Inconel 600 and Ti6Al4V has been presented in subsection 2.8.2 and 2.8.3. The laser focal distance was kept constant at 346 mm between the scanner and the workpiece. Single-sided laser welding experiments of these dissimilar workpieces were conducted in a T-joint configuration at a tilted angle of 45°. Figure 3.5 shows the schematic diagram of the welding experimental setup where the samples were clamped in a T-joint configuration using a clamping fixture jig. Argon gas was used as a shielding gas to prevent oxidation of the weld surface during welding. Table 3.3 shows the welding parameters used in the experiments.
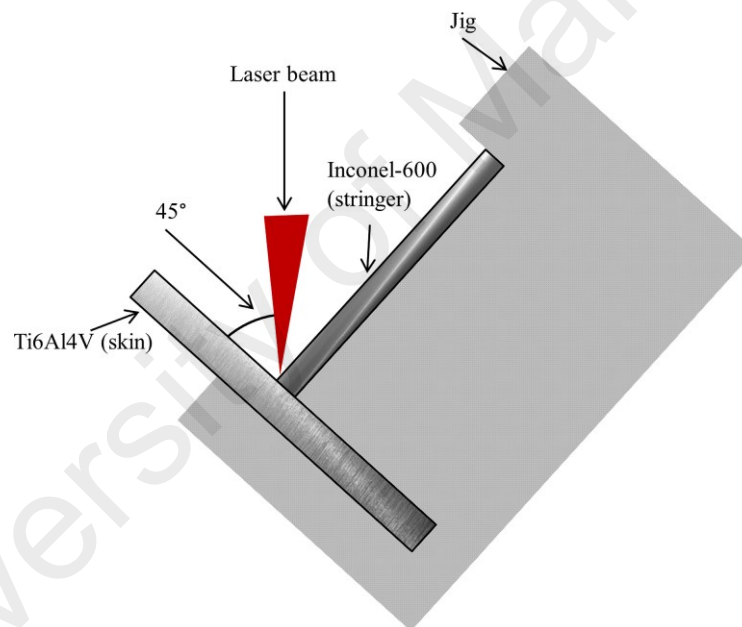
Figure 3.5: Schematic diagram of the welding experiment setup for single-sided laser welding

Table 3.3: Preliminary input variables and their levels used in the single-sided laser welding of Ti6Al4V and Inconel 600

Laser Parameters	Level 1	Level 2	Level 3	Units
Laser Power: LP	250	260	270	Watt
Welding Speed: WS2	40	50	-	mm/s
Overlapping Factor: OF	30	40	50	%

3.2.2 Welding process – Starfiber 300 Fiber laser welding machine

For the laser welding process, the laser machine used is a StarFiber 300 from ROFIN-SINAR Technologies Inc., Germany. It is a diode pumped laser Ytterbium fiber at central emission with Gaussian beam at M^2=1.05, as shown in Figure 3.6. Its minimum and maximum powers are 30W and 300W, respectively. It is a continuous modulated mode of operation with random polarization, having a wavelength range of 900nm to 1200nm with the central emission wavelength of 1070nm. The power modulation rate is 50kHz. It has an assisting 1mW pilot laser, which is used as a positioning aid that can be safely viewed with the naked eye. The laser beam is transmitted along a 10m long step-index optical glass fibre of 0.6mm diameter terminated with collimating optic. The beam is reflected to the workpiece by a mirror inclined at 45° at the bending cube. The laser beam is focused on the T-joint with a focusing lens of 346 mm focal length.

With the given, M^2 =1.05, $\lambda = 1070$nm, F_O =346mm, $\emptyset_i$=5mm (Rofin Starfiber 300 specification), the beam diameter, D and focused focal length, Z_R can be calculated from Equation 3.1 and 3.2.

$$D = 2W_O = \frac{4\lambda}{\pi}\left(\frac{F_O}{\emptyset_i}\right) M^2 \qquad\qquad (Eq.3.1)$$

$$= \frac{4(1.07um)(0.346)\times 1.05}{(3.142)(0.005)} \approx 100 \; \mu m$$

$$Z_R = \frac{\pi W_O{}^2}{\lambda} \qquad\qquad (Eq.3.2)$$

$$= \frac{(3.142)(50um)^2}{1.07um} = 7.34mm$$

Focus range is calculated by adding and subtracting 7.34mm from 346mm shown in Equation 3.3.

Focal range = Fo - Z_R (Eq.3.3)

Thus, the in-focus focal range lies between 338.66 to 353.34 mm, and other ranges are considered as out of focus.
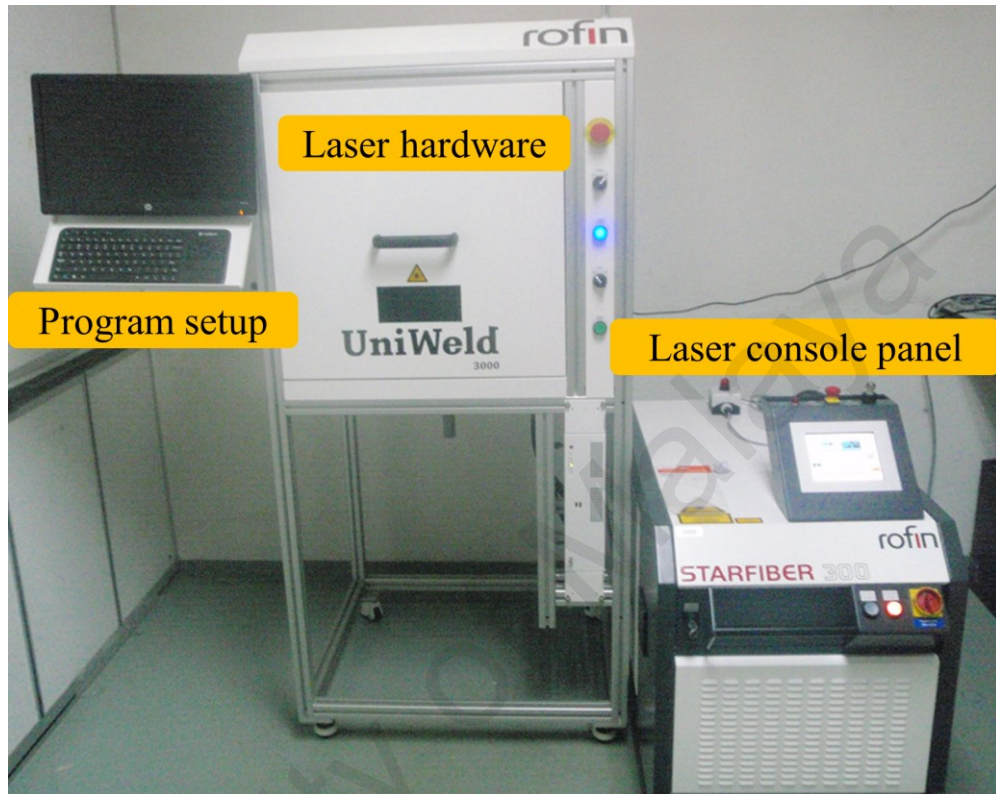
Figure 3.6: StarFiber laser 300 used throughout this study for laser welding

3.2.3 Pull test analysis

In accordance to Badini et al (2009), the pulling method was used to evaluate the strength of the joints in these studies and was carried out successfully (Badini et al., 2009). Figure 3.7(a) shows the schematic diagram of a test sample in the pulling test jig. The customized jig was required to conduct the pulling test on a T-joint welded specimen, as shown in Figure 3.7(b).
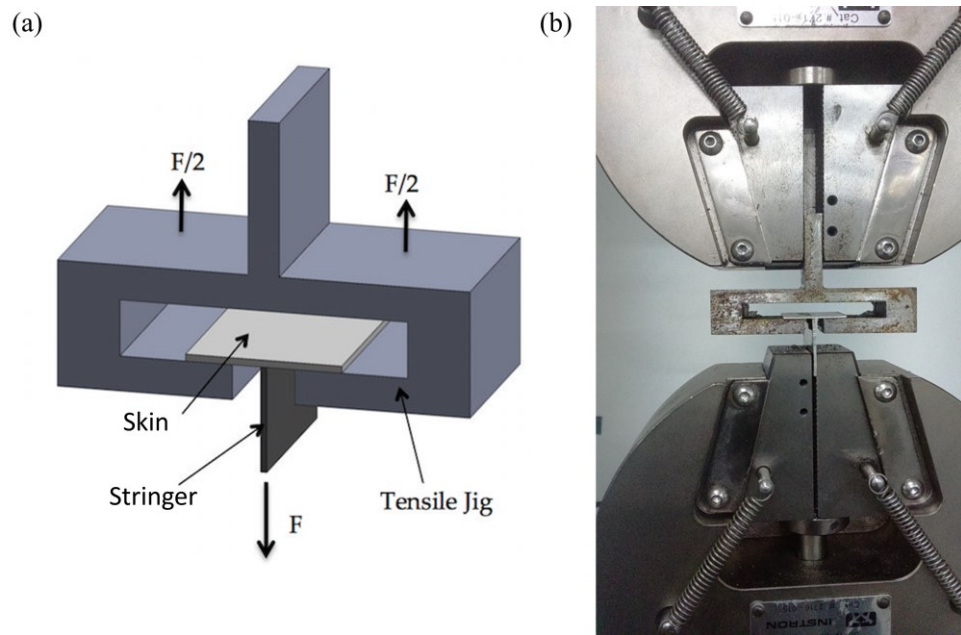
Figure 3.7: (a) Schematic diagram of pulling test for T-joint configuration of dissimilar materials (b) Customized jig used for pulling test

The pull test was performed using a universal testing machine (INSTRON, Model: 3369, Necomb Sdn. Bhd.), at room temperature with the crosshead speed of 5 mm/min and a loading of 10 kN. The results of welding strengths were determined from the average value of three different samples. From the results, the higher the fracture force, the stronger the weld strength is and this combination parameters are identified as optimized parameters to evaluate the metallurgical and hardness values.

3.3   Safety requirements

During the whole experimental work, safety issues were handled with care. The Rofin Starfiber 300 is categorized under Class 4 which has high risk for eyes and skin. During installation, the machine has been equipped with safety precautions such as protection quartz window. Intensive training were provided before handling the laser machine and only authorized users were allowed to run the machine. Warning labels

were placed outside the room as well as inside. The fibers attached to the machine should be in coiled with at least 1m diameter. Standard operating procedure will be always shown and placed at the machine for easy references. The machine is placed 1m away from the wall for ventilation purpose.

3.3.1 Prior to laser welding

Before using the machine, operators must make sure the lens is clean from debris and vicinity of the machine is cleaned. Operators need to wear mask, safety goggles and switch on the exhaust fan (for ventilation from welding fume and shielding gas). The users need to close the chamber in order for the machine to work. The safety precaution taken where machine will not work until the doors are closed.

3.3.2 During laser welding

During laser welding, operators are not advised to look through the quartz window to avoid short term blindness unless necessary. The users must wear goggles to protect their eyes in the case where they need to see through the window. In case of emergency such as fire or explosion, users are educated to press the emergency button. This will stop the machine totally.

3.3.3 Post laser welding and cleaning

After welding has taken place, the samples might be hot and users should use gloves to remove the samples. Before switching off the machine, users must clean the machine

and its vicinity. The debris must be collected in the designated dustbin to avoid mishandling wastage.

3.4   Fuzzy logic

Section below will explain the fuzzy logic prediction for each part of research compared to the pull test results. Fuzzy logic is used to predict the real time experiments after setting a range of data from the training data. Through fuzzy expert system, fracture force results from laser welding of materials with similar properties can be predicted as well. Next, the testing data and experiment data are compared to evaluate the effectiveness of the pull test. The sample preparations are the same as shown in previous subsections. In these up-coming subsections, the fuzzy logic input variables, levels and proposed fuzzy models were shown.

In fuzzy logic, variables are defined as linguistic values that can be conveyed as synthetic language, words or sentences (Ross, 2009). Welding strengths can be analyzed using fuzzy logic to eliminate unnecessary parameters combinations. In this study, the weld strength prediction was conducted using MATLAB R2009b software, with more membership function included to obtain the results. Generally, in fuzzification, two membership functions are used; triangle and trapezoidal membership function (Pedrycz, 1994), with the triangular membership function being the simpler of the two (Klir & Yuan, 1995). From the prediction results, the optimized parameters samples were further analyzed for metallurgical and hardness properties. The output results in the form of the fracture force values needed to break the weld were obtained as fuzzy variables. Therefore, defuzzification process was needed to convert the fuzzy output into a relative value. The centroid method was used for the defuzzification in order to

determine the non-fuzzy value (Klir & Yuan, 1995) and expressed in the following Equation 3.4.

$$Z_O = \frac{\sum_{i=1}^{n} \mu(x_i) h}{\sum_{i=1}^{n} \mu(x_i)} \qquad \text{(Eq.3.4)}$$

where Z_O is the crisp value of the fracture force, h is the position of the singleton and $\mu(x_i)$ is the firing level of i rule when $i = 1,..., n$.

During defuzzification, truth degree of rules was calculated based on the minimum two independent rules with the maximum between two working rules. Rajasekaran and Vijayalakshmi (2003) attested that if the output is presented as a single scalar, the decision is more accurate (Rajasekaran & Pai, 2003). In addition, method goodness of fit, *n,* for prediction of fracture force can be calculated, as shown in Equation 3.5 (Hossain et al., 2016);

$$n = R^2 = \sqrt{1 - \frac{\sum_{i=1}^{k}(x_i - \widehat{x_i})^2}{\sum_{i=1}^{k}(x_i - \overline{x_i})^2}} \qquad \text{(Eq.3.5)}$$

Relative error, ε is given is Equation 3.6 as follows (Hossain et al., 2016):

$$\varepsilon = \sum_{i=1}^{k} \left| \frac{\overline{x_i} - \widehat{x_i}}{\overline{x_i}} \right| \times \frac{100\%}{k} \qquad \text{(Eq.3.6)}$$

where k is the total experiment number, x_i is the experimental value, $\widehat{x_i}$ is fuzzy logic predicted value, $\overline{x_i}$ is the average of the experimental value.

In each study, the laser power was set at three levels of 250W, 260W and 270W. Three linguistic values were used for input variable (Low, Medium and High) as shown in Equation 3.7 and a triangular membership function was used.

$$LP(i_1) = \begin{cases} i_1, & 250 \le i_1 \le 270 \\ 0, & otherwise \end{cases} \qquad \text{(Eq.3.7)}$$

where i_1 = laser power

3.4.1   Part I: Double-sided laser welding of AA2024-O and AA7075-T6

In this particular evaluation, 5 linguistic values (Level 1 to Level 5) were used (Low, Medium-Low, Medium, Medium-High and High) to describe the welding speeds, as shown in Table 3.1. The proposed fuzzy model is presented in Table 3.4.

Table 3.4: Details of proposed fuzzy model for laser welding of AA2024-O and AA7075-T6

Type of fuzzy inference system (FIS)	Mamdani
Inputs/output	2/1
Input membership function types	Triangular
Output membership function types	Triangular
Rules weight	1
Number of fuzzy rules	15
And method	min
Implication method	min
Aggregation method	max
Defuzzification method	centroid

For fracture forces, the output has 14 linguistic values (mf1, mf2, mf3, mf4, mf5, mf6, mf7, mf8, mf9, mf10, mf11, mf12, mf13, mf14). In this study, Triangle membership function was used for both welding speed and fracture force. IF-AND rules were built using 15 experimental data and the rules were then set. In this dissimilar double-sided T-joint low power fiber laser, fuzzification of the linguistic parameters were made using Equation 3.7, 3.8 and 3.9 (Kumar et al., 2014):

$$WS1(i_2) = \begin{cases} i_2, & 9 \leq i_2 \leq 21 \\ 0, & otherwise \end{cases} \qquad \text{(Eq.3.8)}$$

$$FF(o_1) = \begin{cases} o_1, & 0 \leq o_1 \leq 650 \\ 0, & otherwise \end{cases} \qquad \text{(Eq.3.9)}$$

where i_2 = welding speed for double-sided laser welding of AA2024-O and AA7075-T6 and o_1 = fracture force for double-sided laser welding of AA2024-O and AA7075-T6.

An aggregation process was used to analyze the implication results, generating a single fuzzy set. The linguistic fuzzy sets of laser power (LP) and welding speed (WS1) can be defined into Low, Medium-Low, Medium, Medium-High and High as shown in Equation 3.10 to 3.14:

$$Low = \begin{cases} 240 \le i_1 < 260 \\ \quad i_2 = 9 \end{cases} \tag{Eq.3.10}$$

$$Medium - Low = \begin{cases} i_1 = na \\ i_2 = 12 \end{cases} \tag{Eq.3.11}$$

$$Medium = \begin{cases} 250 \le i_1 < 270 \\ \quad i_2 = 15 \end{cases} \tag{Eq.3.12}$$

$$Medium - High = \begin{cases} i_1 = na \\ i_2 = 18 \end{cases} \tag{Eq.3.13}$$

$$High = \begin{cases} 260 \le i_1 < 280 \\ \quad i_2 = 21 \end{cases} \tag{Eq.3.14}$$

Figure 3.8 shows the membership functions for two inputs; laser power and welding speed with the fracture force as the main output. Figure 3.8(a) and Figure 3.8(b) show the membership functions for input variables whereas Figure 3.8(c) shows the membership function for output variable. Figure 3.9 shows the rules set for all 15 data used in this study.
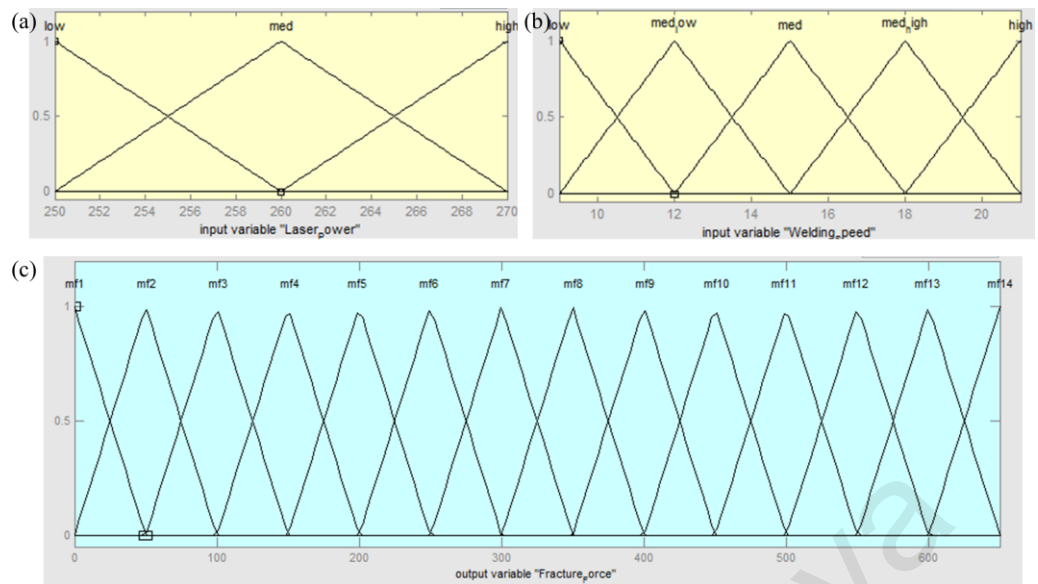
Figure 3.8: Membership functions for (a) Input variable laser power (b) Input variable welding speed (c) Output variable Fracture force
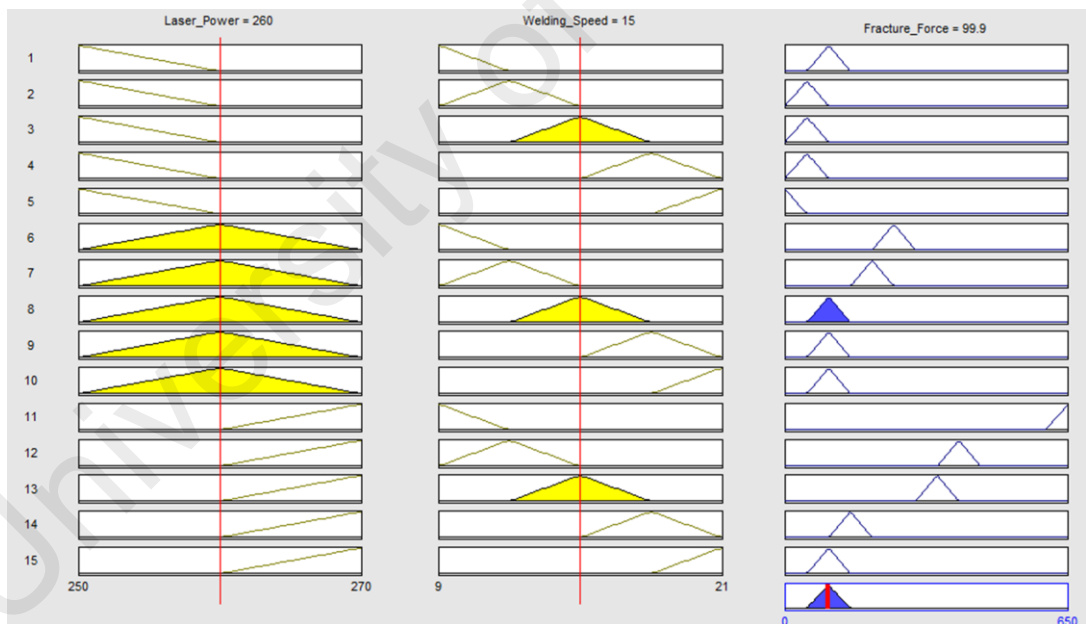
Figure 3.9: Rules set for all the data used in the study

3.4.2 Part II: Double-sided laser welding of AA2024-O and AA7075-T6 with filler alloy BA4047

In this part of the study, fuzzy logic was not necessary as the results from the preliminary test in Part I was sufficient to select range of parameters for further analysis.

3.4.3 Part III: Single-sided laser welding of Ti6Al4V and Inconel 600

In this study, for overlapping factor, 3 linguistic values were used for input variable (Low, Medium and High). Meanwhile, for laser welding speed, only 2 linguistic values were used (Low and High) as shown in Table 3.3. The proposed fuzzy model is shown in Table 3.5.

Table 3.5: Details of proposed fuzzy model for single-sided laser welding of Ti6Al4V and Inconel 600

Type of fuzzy inference system (FIS)	Mamdani
Inputs/output	3/1
Input membership function types	Triangular/Gaussian
Output membership function types	Triangular
Rules weight	1
Number of fuzzy rules	18
And method	min
Implication method	min
Aggregation method	max
Defuzzification method	centroid

For fracture force, the output has 14 linguistic values (ff1, ff2, ff3, ff4, ff5, ff6, ff7, ff8, ff9, ff10, ff11, ff12, ff13, ff14). Triangle membership function was used for overlapping factor while a Gaussian membership function was used for welding speed.

IF-AND-AND rules were built using 18 experimental data and the rules were then set. In this dissimilar single-sided T-joint low power fiber laser, fuzzification of the linguistic parameters was made by the following Equation 3.7, 3.15, 3.16 and 3.17:

$$WS2(i_3) = \begin{cases} i_3, & 40 \leq i_3 \leq 50 \\ 0, & otherwise \end{cases} \tag{Eq.3.15}$$

$$OF(i_4) = \begin{cases} i_4, & 30 \leq i_4 \leq 50 \\ 0, & otherwise \end{cases} \tag{Eq.3.16}$$

$$FF(o_2) = \begin{cases} o_2, & 10 \leq o_2 \leq 160 \\ 0, & otherwise \end{cases} \tag{Eq.3.17}$$

where i_3 = welding speed for single sided laser welding of Ti6Al4V and Inconel 600 , i_4 = overlapping factor for single sided laser welding of Ti6Al4V and Inconel 600 and o_2 = fracture force for single sided laser welding of Ti6Al4V and Inconel 600.

An aggregation process was used to analyze the implication results, generating a single fuzzy set. The linguistic fuzzy sets of laser power (LP), welding speed (WS) and overlapping factor (OF) can be defined into low, medium and high as shown in Equation 3.18, 3.19 and 3.20:

$$Low = \begin{cases} 240 \leq i_1 < 260 \\ i_3 = 40 \\ 20 \leq i_4 < 40 \end{cases} \tag{Eq.3.18}$$

$$Medium = \begin{cases} 250 \leq i_1 < 270 \\ i_3 = na \\ 30 \leq i_4 < 50 \end{cases} \tag{Eq.3.19}$$

$$High = \begin{cases} 260 \leq i_1 < 280 \\ i_3 = 50 \\ 40 \leq i_4 < 60 \end{cases} \tag{Eq.3.20}$$

Figure 3.10 shows the membership functions for three inputs; laser power, overlapping factor and welding speed with fracture force as the main output. Figure 3.10(a), (b) and, (c) are the input variables of the membership functions meanwhile

64

Figure 3.10(d) is the output variable membership function. Figure 3.11 shows the rules set for all the 18 data used in this study.
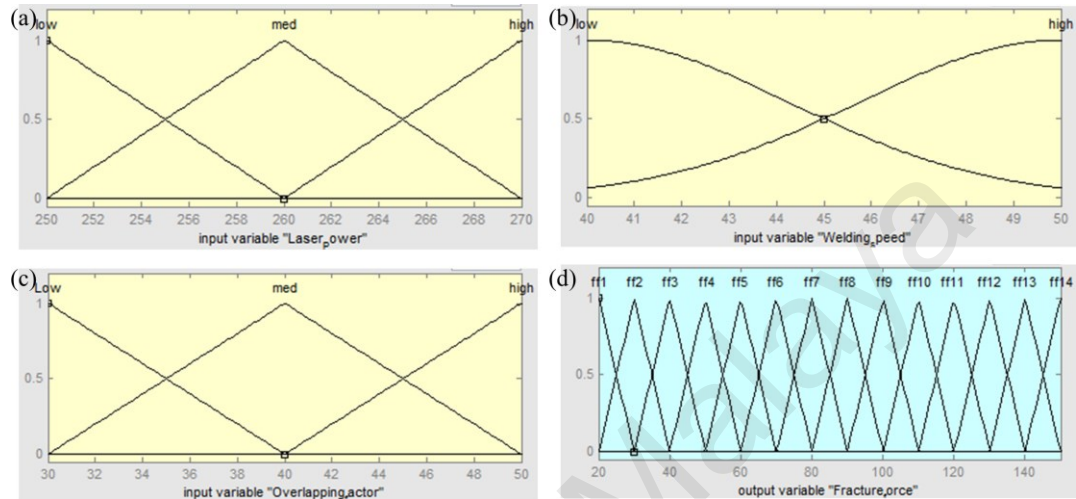
Figure 3.10: Membership functions for (a) Input variable laser power (b) Input variable welding speed (c) Input variable overlapping factor (d) Output variable Fracture force
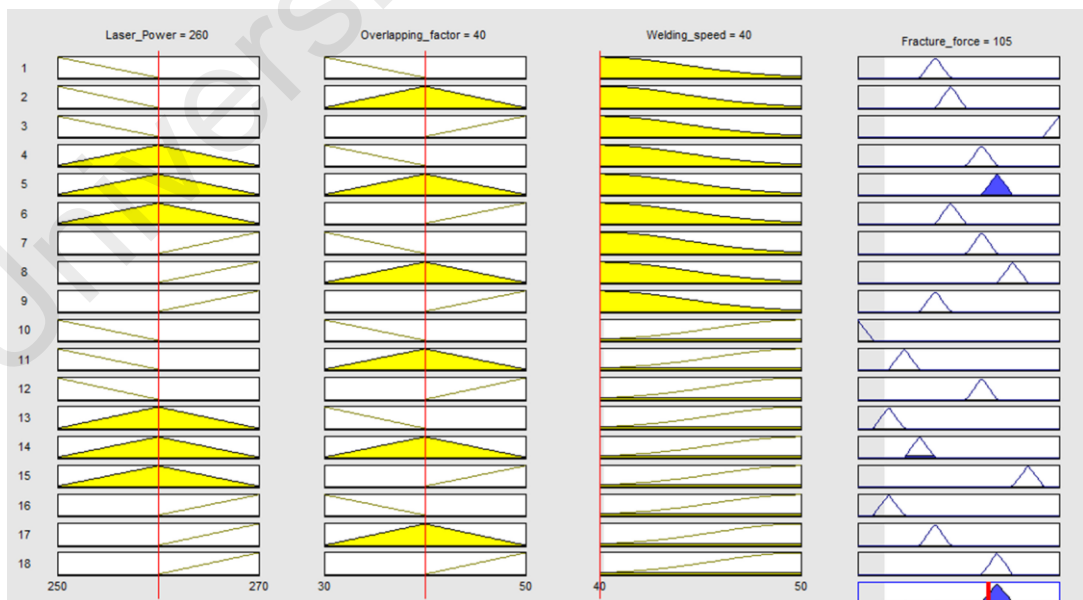
Figure 3.11: Rules set for all the data used in the study

3.5   Metallurgical analysis setup

The techniques used in the material preparation for metallurgical analysis are discussed in this section. The setup consists of cold mount technique, cutting process, grinding, polishing and etching.

3.5.1   Cold mount technique

The welded samples were cold mounted prior to cutting to prevent defects from the cutting stresses. Epoxy resins and fast cure hardener from Extec Corp with a weight ratio of 5:1 were mixed for approximately 3 minutes to obtain a clear solution. The solution was then poured into the molding cups holding the specimens and was left to cure for a minimum 12 hours to ensure complete curing of the mixture. Figure 3.12 shows the all the necessary items needed for cold mounting and curing samples.

Figure 3.12: Epoxy, hardener and necessary equipment to mix the cold mounting solution and curing

3.5.2 Cutting process

A linear precision saw with a diamond cutter was used to cut the molded samples transversely/perpendicularly to obtain the cross sections of the joining region. The rotational and blade speeds used for cutting aluminum alloys and titanium-nickel based alloys joint are listed in Table 3.6 and the machine used is shown in Figure 3.13. Lower speeds were used to cut the harder materials to avoid burr formation, as recommended by the manufacturer.

Table 3.6: Blade rotational speeds and blade feed rates used to cut the weld-joint samples

Materials	Blade rotational speed (rpm)	Blade feed rate (mm/min)
Aluminum alloys	4500	3.0
Titanium-nickel base alloys	3000	1.5
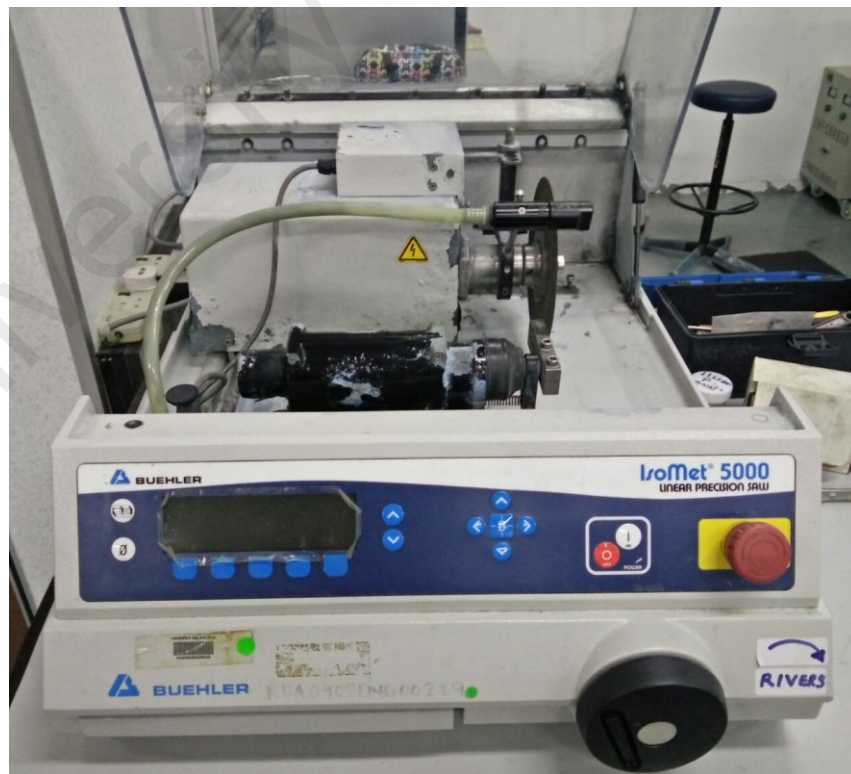
Figure 3.13: Linear precision saw cutter used to cut the molded samples (Model: Isomet 5000, Buehler)

3.5.3   Grinding, polishing and etching process

Standard metallographic methods were utilized to prepare the samples for microstructural observations. The cross-sections of the weld were sequentially grounded using emery paper of increasing grit sizes from 120, 400, 600, 1200 up until 2000. Then, the samples were polished with diamond polishing suspension of 6 μm followed by 1μm particle sizes to obtain a surface mirror finish. The grinding and polishing were conducted using the grinder as shown in Figure 3.14 whereas Figure 3.15 shows the diamond polishing suspension from Extec Corp used to in the final polishing stage.

Figure 3.14: Grinding machine (Model: Metapol-2 Rax Vision) used for grinding and polishing

Figure 3.15: Diamond suspension used for polishing

The polished samples were etched with suitable chemical etchants, as listed in Table 3.7, to reveal the microstructure of the metals. After etching, the samples were washed immediately with distilled water and air dried prior to analysis.

Table 3.7:Chemical etchants used to reveal the microstructure of the base metals, FZ and HAZ

Metals	Etchant used	Etchant composition	Method
Aluminum alloys (AA2024 and AA7075)	Keller's reagent	190ml distilled water 5ml Nitric acid (HNO3) 3ml of hydrochloric acid (HCl) 2ml of hydrofluoric acid (HF)	Swab for 30 seconds and wash with distilled water
Titanium alloys and Nickel alloys (Ti6Al4V and Inconel 600)	Kroll's reagent	92 ml of distilled water (H_2O), 6 ml of Nitric acid (HNO_3) 2 ml of hydrofluoric acid (HF)	Swab for 20 seconds and wash with distilled water

3.6 Material Characterization Equipment

The microstructural properties of the weld were evaluated using various characterization methods which are described in the subsequent subsections.

3.6.1 Imaging – Optical Microscope

The surfaces of the cross sections were initially observed using an Optical Microscope, OM (model: Olympus, Tokyo, Japan), as shown in Figure 3.16, with magnifications of 5x, 10x, 20x and 50x. The optical microscope creates magnified images of the specimen for microstructural observations. The utilization of the optical microscope enables rapid evaluation of the surface quality of the specimens, which determines the necessity for additional polishing and etching process to obtain a satisfactory image quality (Komvopoulos, 2010); (Corporation, 2010) before it can be used in subsequent stages of analysis.

Figure 3.16: Optical microscope used to observe the microstructure at low magnifications.

3.6.2   Scanning Electron Microscope and Energy Dispersive X-Ray Spectroscopy

Scanning electron Microscope (SEM) was used to observe the specimen surface using irradiation of fine electron beam. During irradiation, secondary electrons will be emitted from the workpiece surface. Figure 3.17 shows the SEM (Model: Phenom Pro X, Crest System (M) Sdn. Bhd., Eindhoven, The Netherlands) used to observe the surface morphology. In addition, Energy Dispersive X-Ray Spectroscopy (EDX) (Model: PhenomPro X, Crest System (M) Sdn. Bhd.,Eindhoven, The Netherlands) was used to characterize the elemental compositions and formation of intermetallic phases of the weld.

Figure 3.17: The SEM apparatus used for surface morphology evaluation

3.6.3   X-Ray Diffraction

The formation of intermetallic phases in the weld was characterized by an X-ray diffraction system (XRD), (Model: PaNalytical Empyrean, DKSH Holdings (Malaysia) Bhd., Almelo, The Netherlands) as shown in Figure 3.18 using CuKα radiation in the 2 theta (2θ) diffraction angle range from 30° to 80°. The XRD analysis enables the identification of the atomic arrangements and is important for solid state

characterization. The diffraction data was analyzed using X'Pert HighScore Plus software.

Figure 3.18: X-ray diffraction system

3.7   Mechanical test

Mechanical testing is essential to evaluate the performance of the joined specimens. Mechanical evaluation usually involved the applications of forces onto the specimens, either dynamically or statically. Mechanical testing, such as hardness measurements and pulling tests will also reveal whether the weldment is suitable for its intended applications.

3.7.1   Hardness test

The hardness values of the base metal (BM), fusion zone (FZ) and heat affected zones (HAZ) were measured using a Vickers microhardness tester (Model: HMV 2T E, SHIMAZDU, Kyoto, Japan) using a pyramidal diamond indenter with a load of 200g for a dwell time of 5s. Figure 3.19 illustrates the hardness distribution profile taken of the weld geometry. Nine indentations at an interval of 100 μm were made perpendicular

across the stringer-skin weld seam to measure the variations of hardness values across the FZ, HAZ regions and the base metals. The microhardness measuring system used in the evaluation is shown in Figure 3.20.
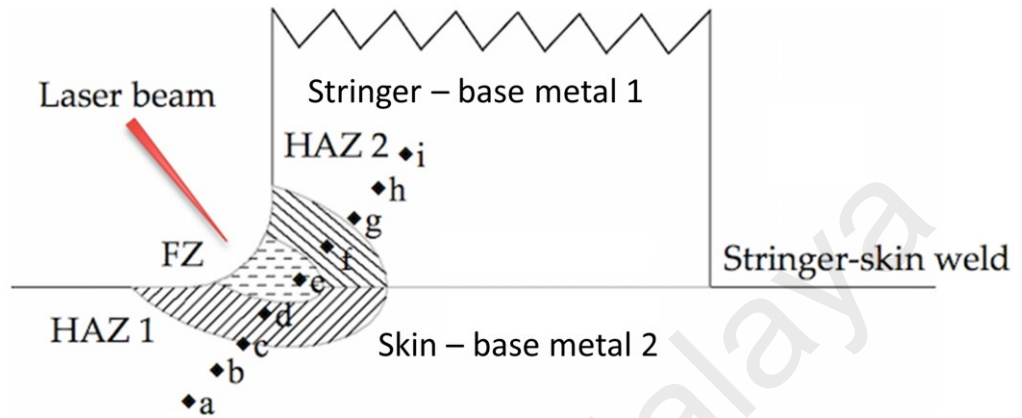
Figure 3.19: Schematic diagram of hardness distribution on the weld geometry
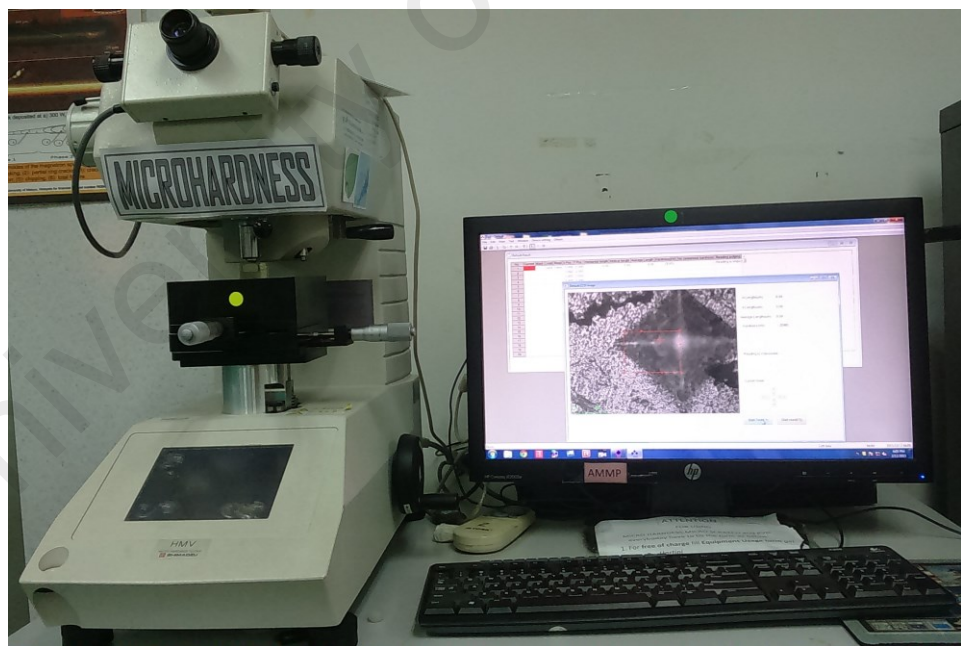
Figure 3.20: Vickers micro-indenter connected to computerized monitor

3.8   Summary

In this chapter the methods and materials used in the experiments for three welding studies were described. The three materials, namely the aluminum, titanium and nickel-based alloys, and the filler material used were presented. Next, the experimental setup, comprising of sample preparations, setup for individual experiments, welding process, preliminary test setup using fuzzy logic, mounting, cutting, grinding, polishing and lastly etching were defined accordingly. Material characterization using optical microscope, SEM and XRD were also described. Finally, the mechanical testing comprising of the hardness and tensile pull test were outlined for the performance analysis of the weldments.

CHAPTER 4: RESULTS AND DISCUSSION

4.1   Introduction

This chapter presents the results and a discussion of the experiments conducted throughout this research. Before determining the parameters for each experiment, the heat input is calculated for the preliminary test. With the equations in subsections 2.3.1 and 2.3.8 the heat input can be calculated to determine suitable parameters to run the preliminary experiments.

4.2   Heat input calculation for the preliminary testing of double-sided laser welding of AA2024-O and AA7075-T6

Figure 4.1 shows the heat input for 200 W to 280W laser power and welding speeds varying from 9 to 27 mm/s applied to aluminum alloys AA2024-O and AA075-T6. Sound joint weldment is shown within the green boundary, while other areas represent defects or no weld.
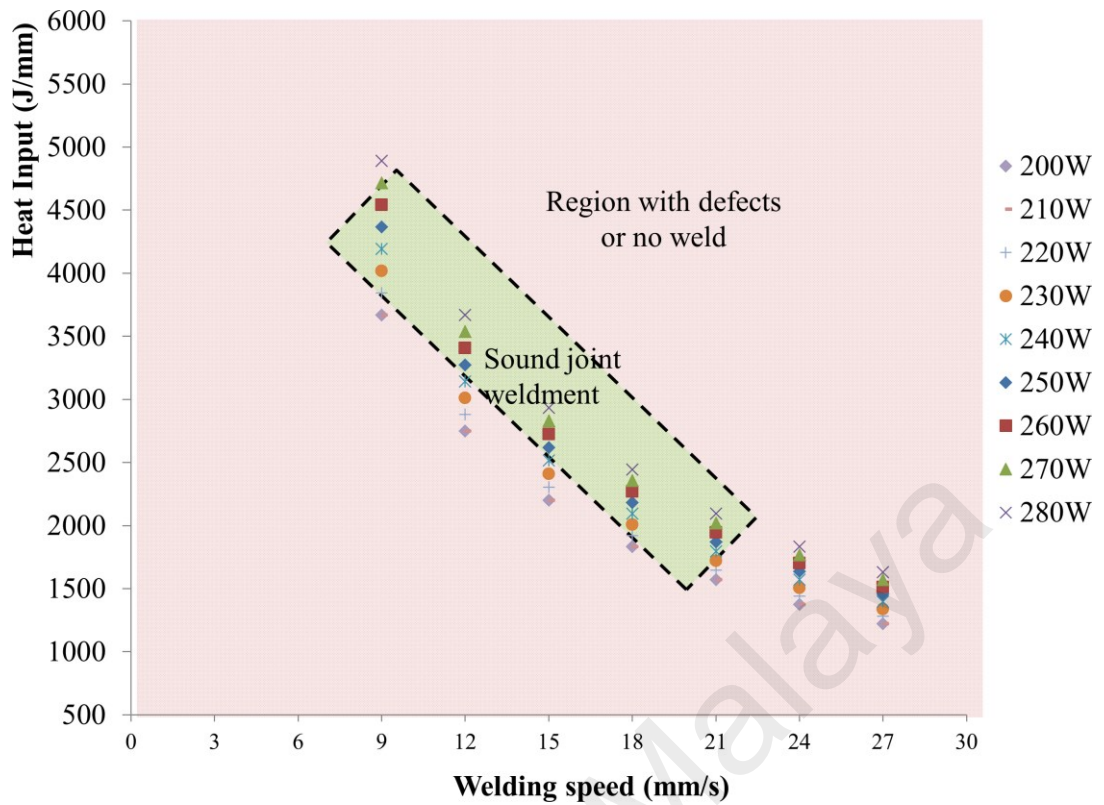
Figure 4.1: Heat input calculated for AA2024-O and AA7075-T6 in the preliminary test

For each input combination, the heat input was calculated using Equation 2.1. However, rapid heating and cooling rates during welding result in decreasing heat input per unit length (Ribic et al., 2009). Heat input is inversely proportional to welding speed. Therefore, higher welding speed gives lower heat input.

4.3   Part I: Double-sided laser welding of AA2024-O and AA7075-T6

From Figure 4.1, the preliminary testings were obtained to narrow down the parameters for double-sided laser welding of AA2024-O and AA7075-T6.

4.3.1   Pull test results and analysis

Pull test experiments were done on a range of parameters as shown in Table 4.1. The suitable parameter range were chosen for metallurgical and microhardness analyses.

Table 4.1: Preliminary parameters in welding AA7075-T6 and AA2024-O

No.	Power (W); P	Welding Speed (mm/s); v
A1	250	9
A2	250	12
A3	250	15
A4	250	18
A5	250	21
B1	260	9
B2	260	12
B3	260	15
B4	260	18
B5	260	21
C1	270	9
C2	270	12
C3	270	15
C4	270	18
C5	270	21

The effects of various laser welding speeds on weld bead fracture force are presented in Figure 4.2, Figure 4.3 and Figure 4.4. By comparing samples A1 to C5, it is observed that the weld bead's fracture force decreased with increasing welding speed. In the present study, the maximum breaking force was achieved for sample C1 when the welding speed was 9 mm/s with constant laser power of 270 W. The decrease in force is mainly because laser welding at higher welding speed induces lower heat input, thus forming a narrow fusion zone with shallow penetration. Therefore, lower breaking force is needed to fracture the sample. The results are correlated with the metallurgical characterization results obtained, where heat input is the main factor affecting the

geometry and strength of the weld joint. Lower welding speed gives higher heat input, as theoretically proven in Equation 2.11. The highest heat input calculated for sample C1 is approximately 4715 J/mm, which requires 642.79 N to break the joint.
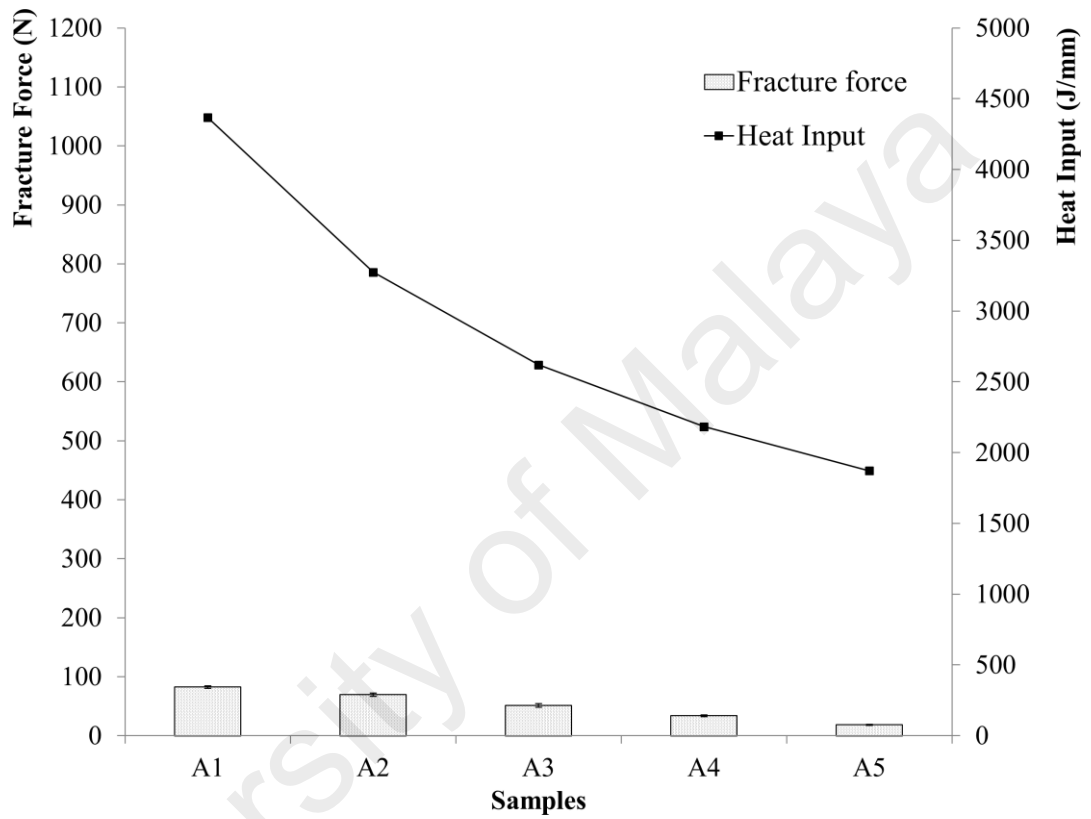
Figure 4.2: Fracture force and heat input for samples A1 to A5
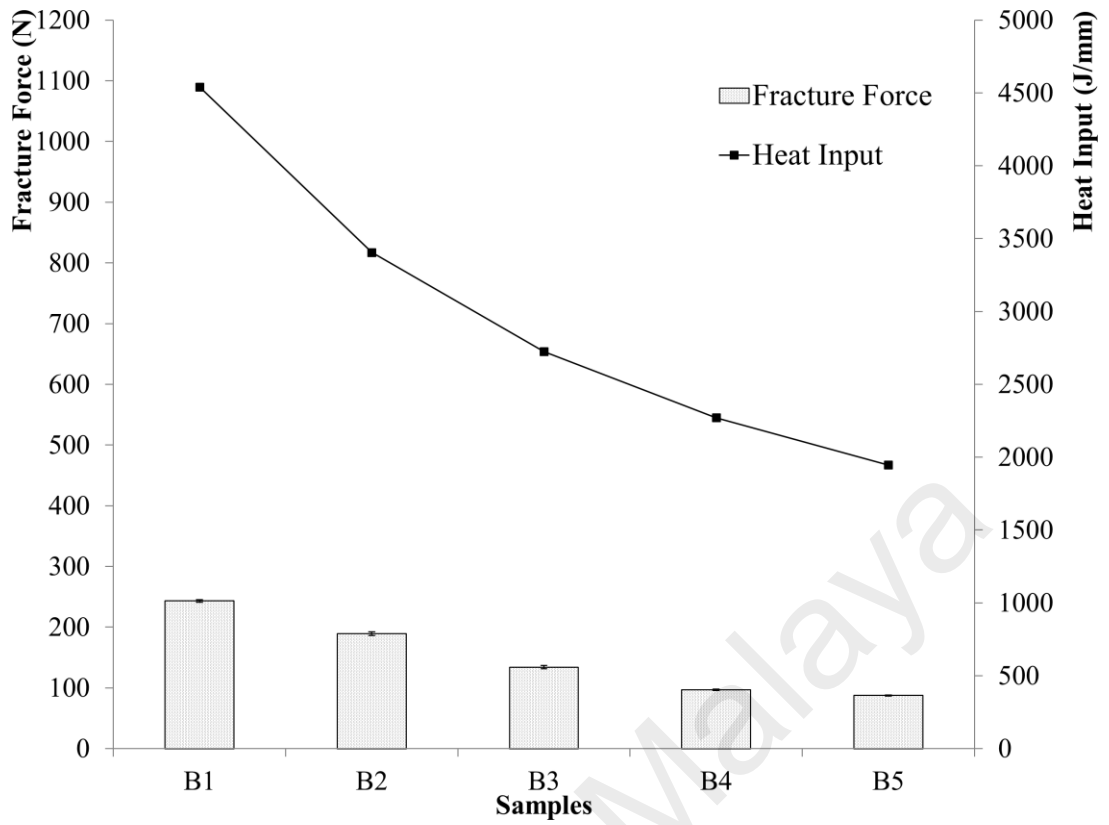
Figure 4.3: Fracture force and heat input for samples B1 to B5
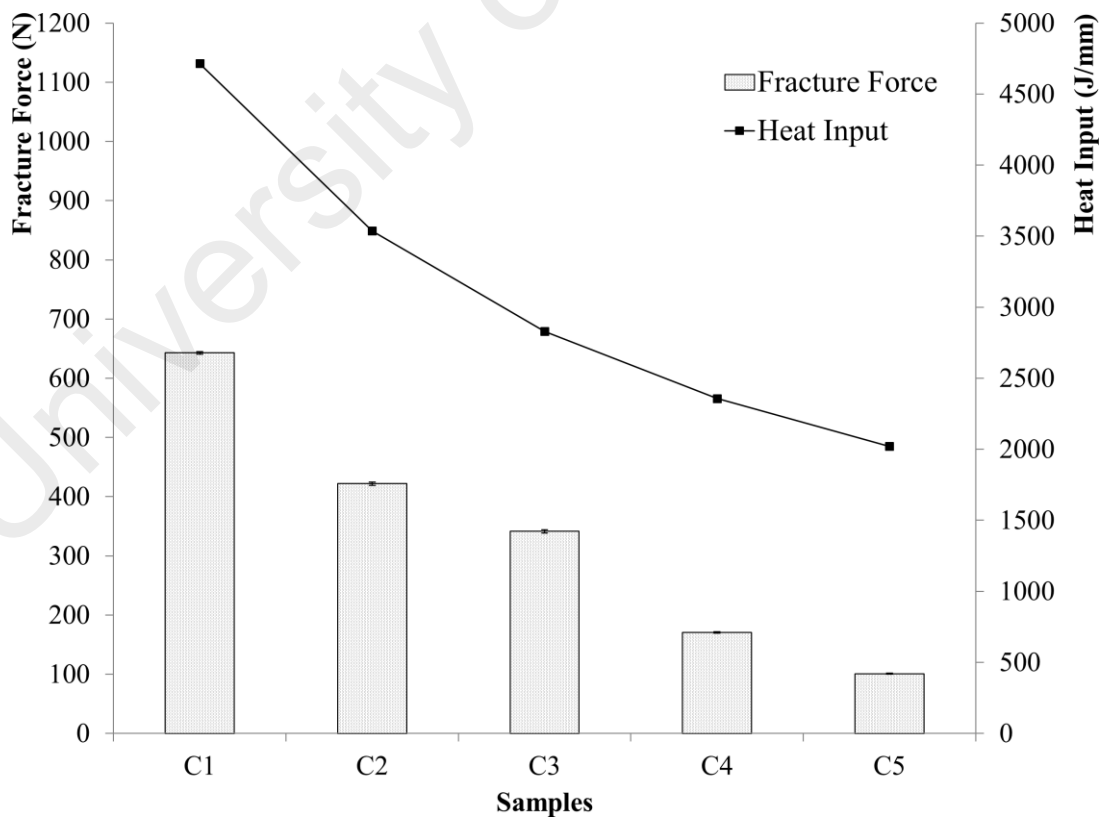
Figure 4.4: Fracture force and heat input for samples C1 to C5

The fractured area for sample C1 were shown in Figure 4.5 with (i) indicates the melted area after laser beam hits the first seam and (ii) indicated the melted area after laser beam hits the second seam. All the samples had the same pattern of fracture and the gap between the weldment is the same as the gap line calculated. The residual stress was negligible as the welded samples were not warped at obvious angles.
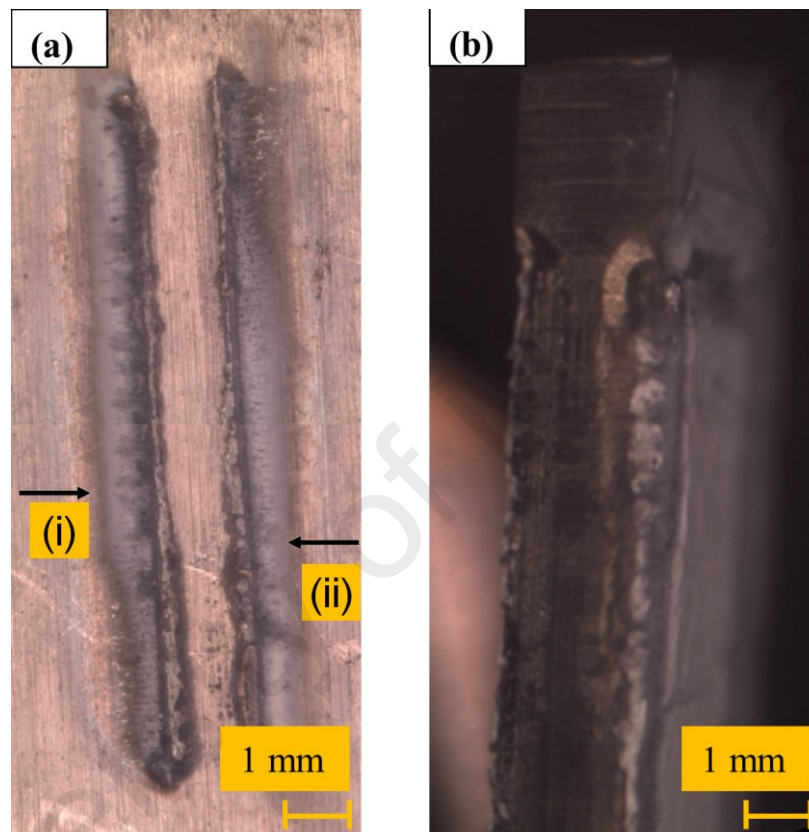
Figure 4.5: Fractured samples after pull test at (a) skin (b) stringer

With 270W laser power and laser welding speeds varying from 9 to 21 mm/s, a range of higher fracture forces were obtained. To further confirm the fracture force prediction results, they were simulated using MATLAB R2009b -- a fuzzy logic development made based on the Mamdani technique.

4.3.2   Fuzzy smart model for selecting parameter range

According to the pull test results, a fuzzy logic model was developed successfully for selecting range of parameter in double-sided laser welding of AA2024-O and AA7075-T6. The effects of laser power and welding speed were used to determine the weldment penetration strength. The heat input gained during laser welding affects the weld joint's strength, which is influenced by welding parameter variation (Unt & Salminen, 2015). Twenty (20) experiments were carried out; from which fifteen (15) were used for training from Table 4.1 and five (5) were applied to test and validate the smart model developed. Table 4.2 shows the testing parameters that were chosen randomly to determine the effectiveness of this fuzzy logic model for double-sided laser welding of AA2024-O and AA7075-T6.

Table 4.2: Parameters tested upon developed fuzzy logic model for double-sided laser welding of AA2024-O and AA7075-T6

No.	Power (W); P	Welding Speed (mm/s); v
1	254	9
2	258	11
3	260	17
4	263	18
5	267	21

Figure 4.6 and Figure 4.7 shows the difference between the training and testing data with predicted values together with error of percentage respectively. Relative errors, ε as discussed in Equation 3.5 were calculated for training and testing data. The values were 7.85% and 5.58% respectively with the calculation shown in Equation 4.1 and Equation 4.2. The relative error is less than 10% and considered acceptable, as supported by Nukman et al. (2013) (Nukman et al., 2013).
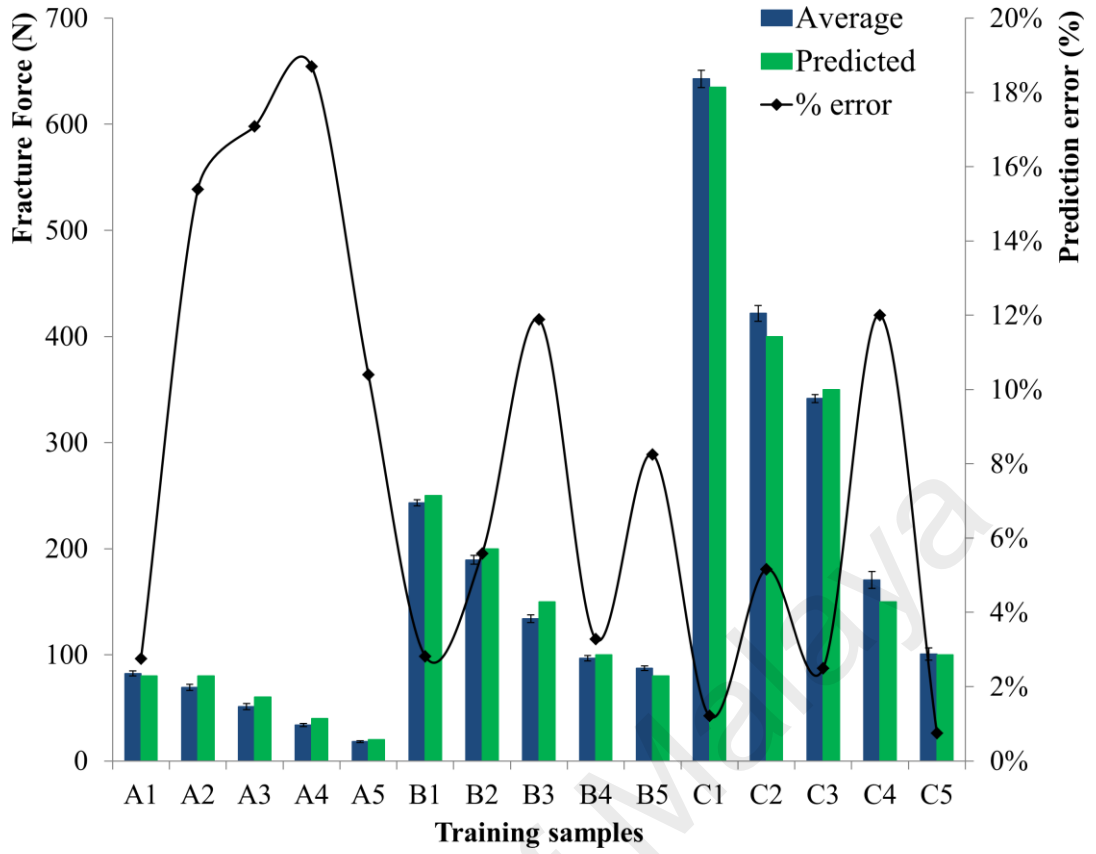
Figure 4.6: Training results and fuzzy logic prediction values as error percentages for the double-sided laser welding of AA2024-O and AA7075-T6

$$\varepsilon_{training} = \sum_{i=1}^{15} \left| \frac{\overline{x_i} - \widehat{x_i}}{\overline{x_i}} \right| \text{ x } \frac{100\%}{15} \qquad = \frac{1.177}{15} \text{ x } 100 = 7.85\% \qquad \text{(Eq.4.1)}$$

$$\varepsilon_{testing} = \sum_{i=1}^{5} \left| \frac{\overline{x_i} - \widehat{x_i}}{\overline{x_i}} \right| \text{ x } \frac{100\%}{5} \qquad = \frac{0.279}{5} \text{ x } 100 = 5.58\% \qquad \text{(Eq.4.2)}$$

where $\widehat{x_i}$ is fuzzy logic predicted value, $\overline{x_i}$ is the average of the experimental value.
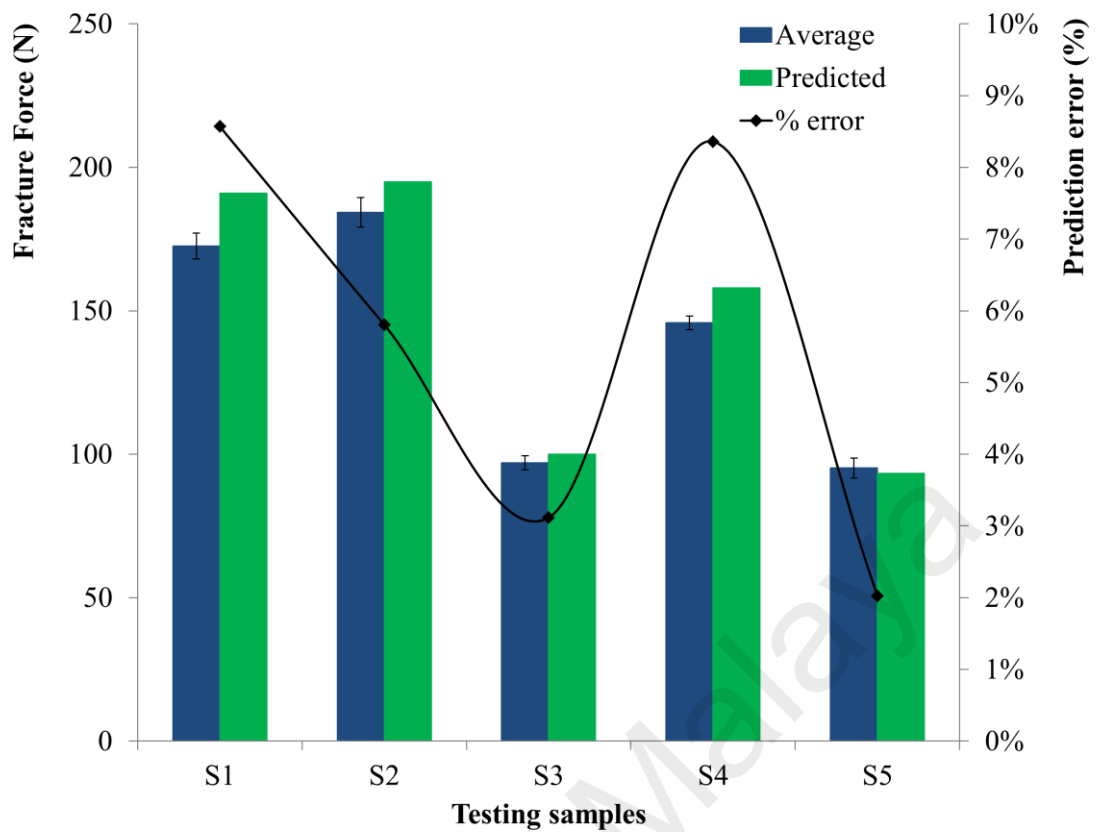
Figure 4.7: Testing results and fuzzy logic prediction values as error percentages for the double-sided laser welding of AA2024-O and AA7075-T6

For higher laser power or lower welding speeds, the affected areas are exposed to more accumulated heat input that would result in increased facture force. By comparing samples S1 to S5, high laser power with lower welding speed will have higher strength of weldment and needs higher fracture force, conforming to previous explanation. Regression graphs are plotted in Figure 4.8 to compare both experimental and prediction values. In the graphs, the goodness of fit (R^2) values in training and testing are 0.9963 and 0.9956 respectively.
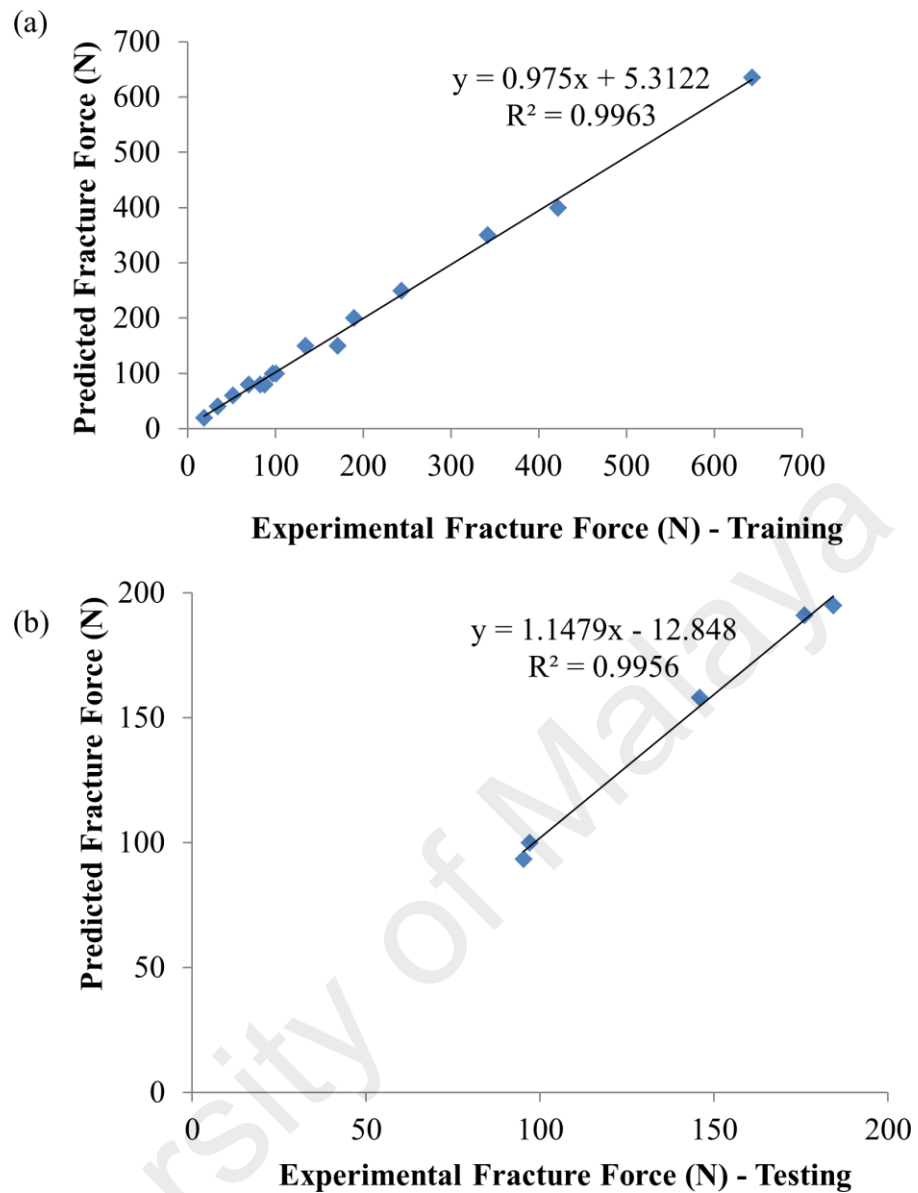
Figure 4.8: Correlation between experimental and fuzzy logic-predicted fracture force (N) in double-sided laser welding of AA2024-O and AA7075-T6, in (a) training and (b) testing

In the surface plot in Figure 4.9, the factors influencing weld strength are determined. When the welding speed decreased, the fracture force increased due to the higher heat input generated and stronger weld penetration. Meanwhile, increasing the laser power resulted in higher fracture force. Overall, the prediction was successful and the next evaluation can be done.
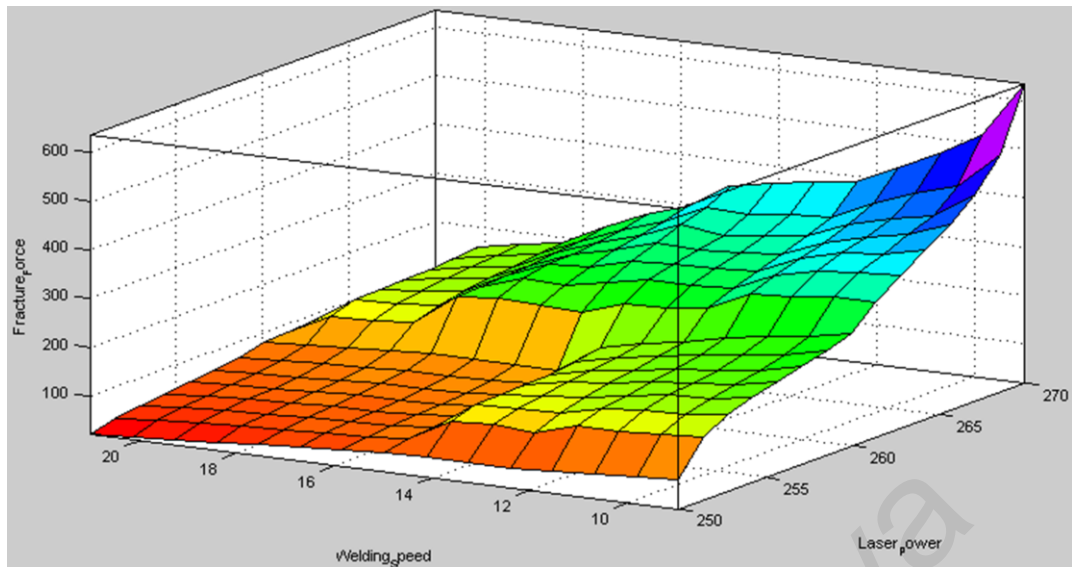
Figure 4.9: Fuzzy inferring system control surface: effect of laser power and welding speed on fracture force

4.3.3 Metallurgical characterization

In the next step, the metallurgical characterization was evaluated by keeping the laser power constant at 270 W and varying the welding speed and focal distance. This setting was chosen from the preliminary pull test that showed a suitable range of parameter. Figure 4.10 displays OM images of T-joint weldment cross sections at various welding speeds, 270W laser power and constant focal distance of 346 mm between the scanner and workpiece.

Undercuts and pores were observed on sample C1 at welding speed of 9 mm/s (Figure 4.10(a)) as more molten metal was produced and evaporation occurred at lower welding speed due to the high heat input. At lower welding speeds, increasing amounts of metals melted and evaporation level rose, leading to deeper penetration. Rapid cooling during the solidification of the metal pool may trap gas vapor, forming pores in the joining region.
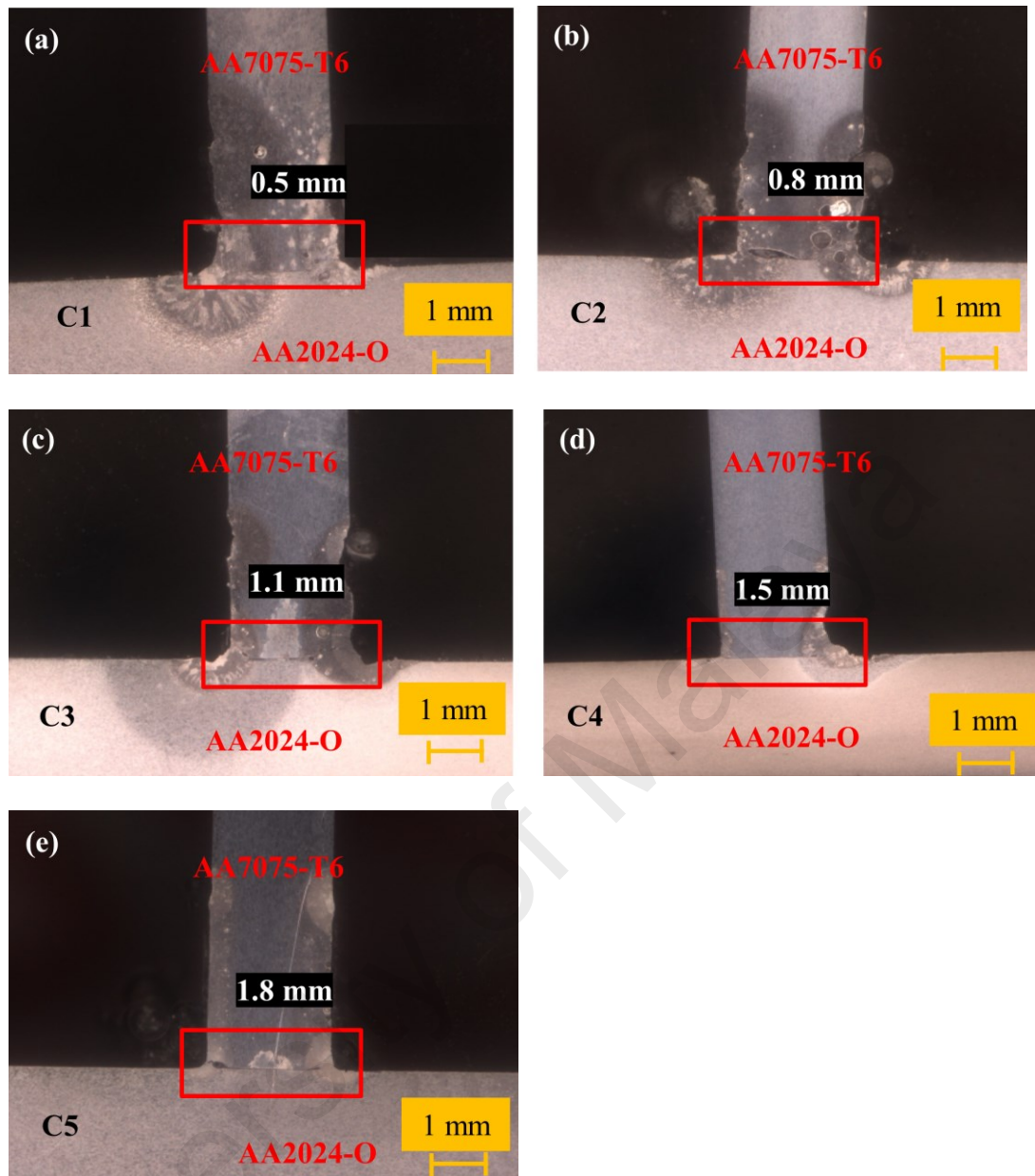
Figure 4.10: Micrographs at 270W laser power and welding speeds of (a) 9 mm/s, (b) 12 mm/s, (c) 15 mm/s, (d) 18 mm/s and (e) 21 mm/s

The argon gas used to protect the weld surface from oxidation and contamination may contribute to the formation of porosities as the gas gets trapped by the turbulent welding pool and keyhole (Katayama, 2013). Manipulating the laser welding speed influences the desired heat input and can help determine the stringer material's penetration into the skin. As the heat input decreases with increasing welding speed, the gap line increases. When higher welding speed is applied, insufficient heat input causes

less penetration towards the weld seam and thus leads to a larger gap line. The gap line is defined as the partition between the two alloys, AA2024-O and AA7075-T6, as shown by the schematic in Figure 4.11. The gap line observed on the joints increased from 0.5 to 0.8, 1.1, 1.5 and 1.8 mm when the welding speed increased from 9 to 12, 15, 18 and 21 mm/s respectively, as shown in Figure 4.12 proving the penetration has become lesser.
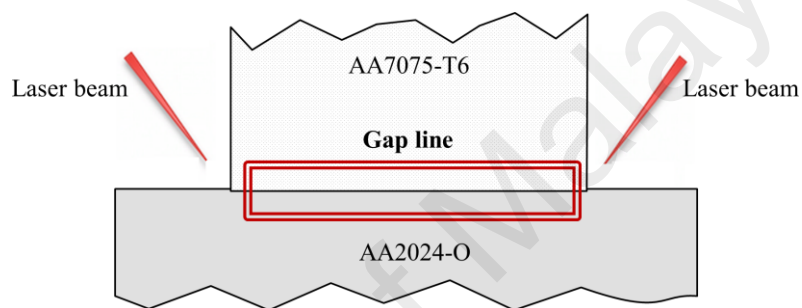
Figure 4.11: Schematic diagram of two base metals welded together and the gap line defined
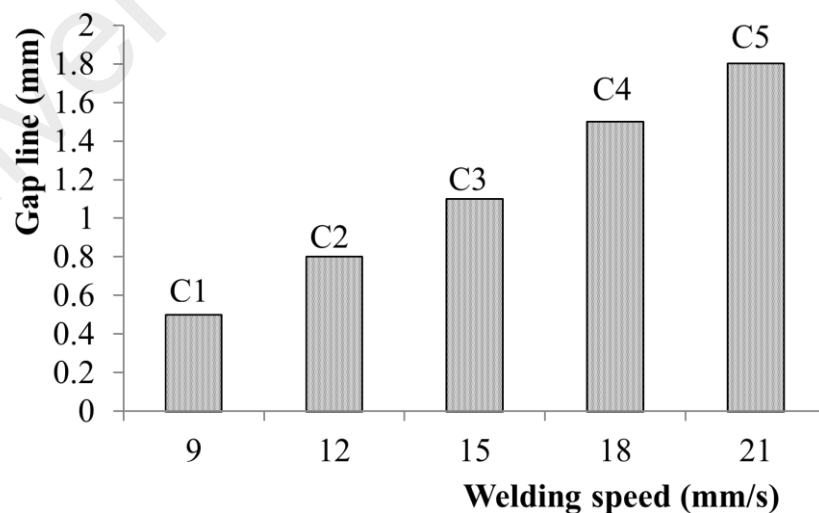
Figure 4.12: Gap line when welding speed increases from 9 to 21 mm/s

The next step was to keep the laser power and welding speed constant with varying the focal distance. The effect of laser focal offset was investigated for a constant laser speed of 18 mm/s and laser power of 270 W. For the laser focal offset, the focal distances evaluated at -1, 0 and +1 from the reference focal distance of 346 mm at 338 mm and 354 mm respectively, were calculated using the Rayleigh length Equations 3.1 and 3.2. As mentioned earlier, the focal range was 338.66 to 353.34 mm. Therefore, for offset of -1, a value of 338 mm was chosen while 354 mm was chosen for +1 offset. Table 4.3 shows the varying focal distance to evaluate the gap line in the AA2024-O and AA7075-T6 weld.

Table 4.3: Varied focal distance to evaluate the gap line in the AA7075-T6 and AA2024-O weld

No.	Focal distance (mm), f	Offset
C4	346	0
C6	338	-1
C7	354	+1

Figure 4.13 indicates that the gap line decreased when both focal distances were defocused at +1 and -1 offset. However, a significant reduction was obvious when the focal distance was offset at +1. When defocused, the laser beam irradiated a larger workpiece area, as seen in Figure 4.14. The heat from the laser beam melted a larger area and penetration increased, resulting in a shorter gap line. The area irradiated with laser beam is larger for C7 compared to C6, hence the penetration of laser beam is more and stronger weldment was produced at C7. Therefore, the gap line for C7 is shorter (0.41mm) compared to gap line in C6 (1.43mm). However, from Figure 4.15, it is proven that even though the gap line is reduced, the fracture force was still low due to

the low heat input. As explained earlier, heat input plays vital role in determining the strength of the weldment.
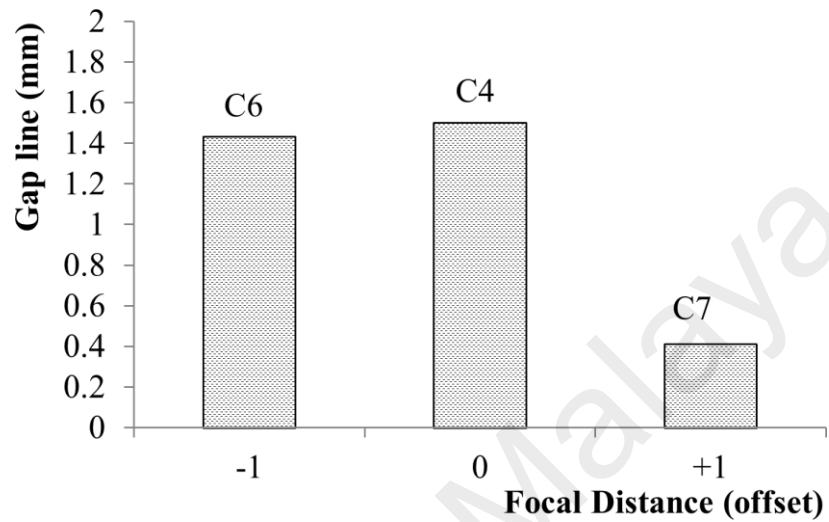
Figure 4.13: Decreasing gap line with focal distance varying from -1 to +1 at constant welding speed of 18 mm/s
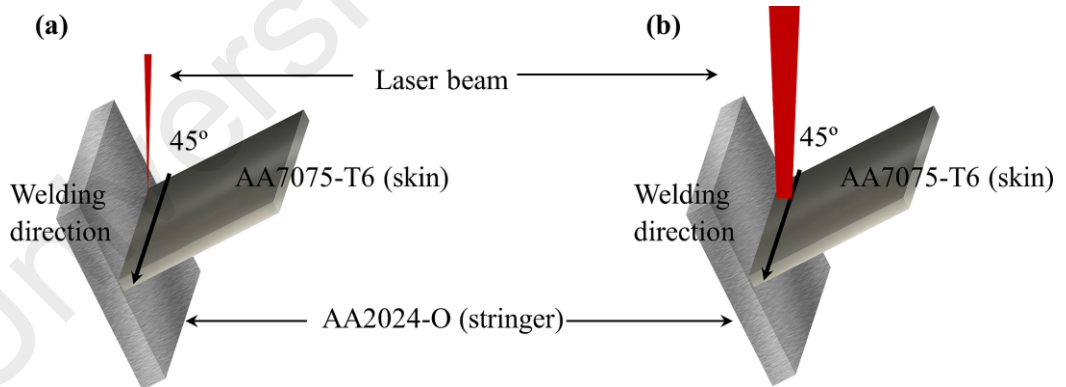
Figure 4.14: Schematic diagram when the focal distance is (a) focused, offset at 0, and (b) defocused, offset at +1
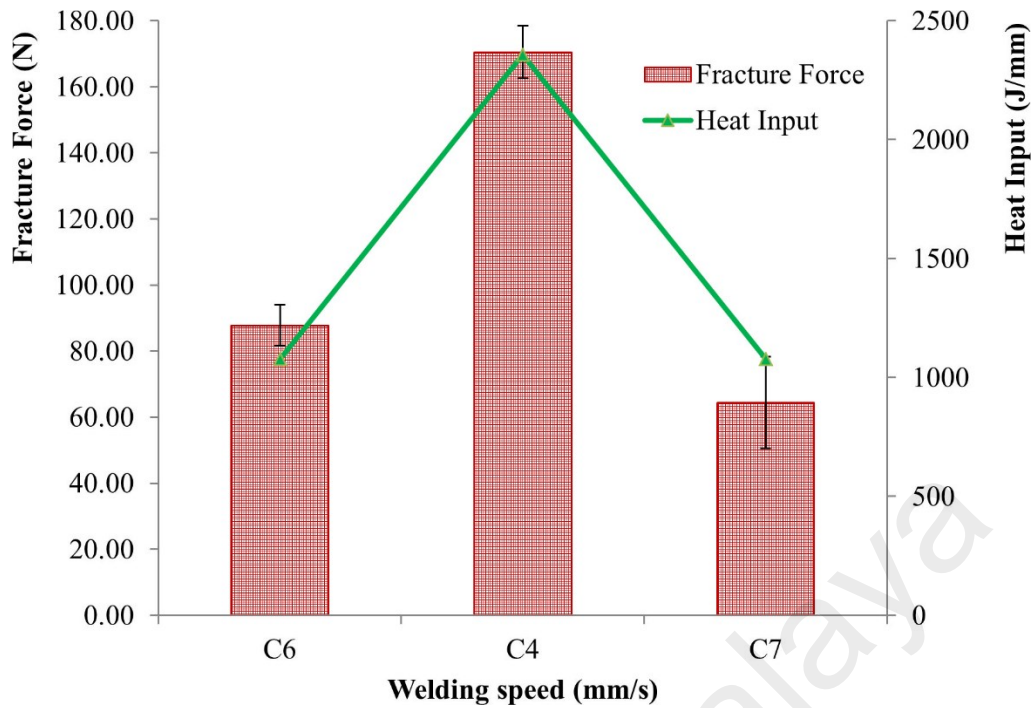
Figure 4.15: Fracture force for focal distance offset -1, 0 and +1

4.3.4 Microstructural analysis

Figure 4.16 is a general schematic diagram of the FZ, HAZ1, HAZ2 and base of the AA2024-0 and AA7075-T6 sample. Figure 4.17(a) and Figure 4.17(b) show the microstructure of the AA2024-O and AA7075-T6 base metals respectively.
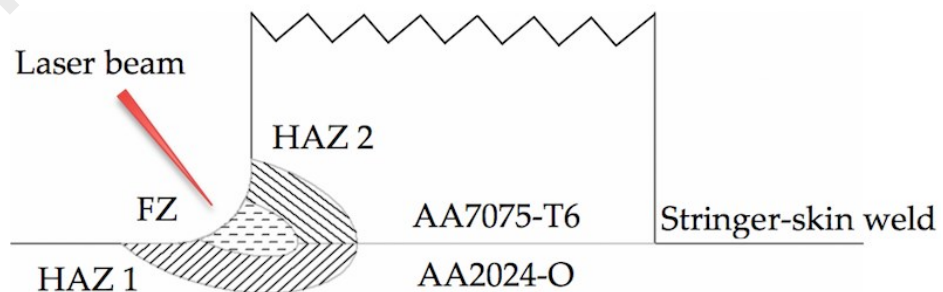
Figure 4.16: Schematic diagram of the FZ, HAZ1, HAZ2 and base of the sample
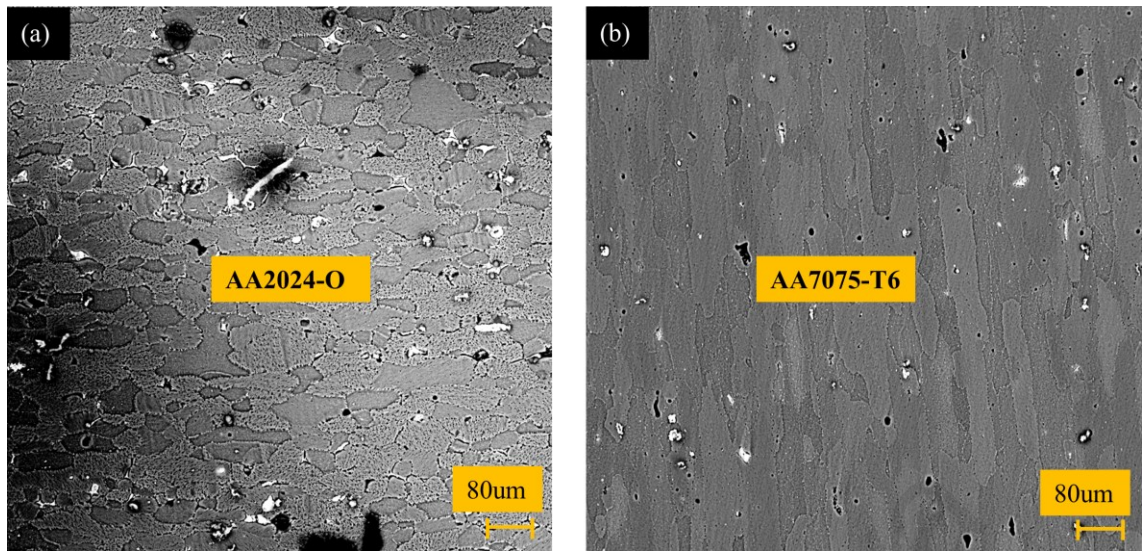
Figure 4.17: SEM micrographs at 1000x magnification: (a) AA2024-O base and (b) AA7075-T6 base

Figure 4.18 shows the microstructures at the interface between the FZ and HAZ of AA2024-O (denoted as HAZ1) and AA7075-T6 (denoted as HAZ2) in the sample C1 cross section. It is observed that the microstructures of the different welding speed beads show similar patterns in all welding conditions studied. The major differences are in the fusion zone width and depth values with varying welding speed. Such phenomenon could be attributed to rapid solidification when the grains in the microstructure are rather small (Norris et al., 2011). In all welded samples, the microstructure in the fusion zone consists of fine Mg precipitates of the second phase in solid solution from aluminum alloy (Sanchez-Amaya, Delgado, De Damborenea, et al., 2009).
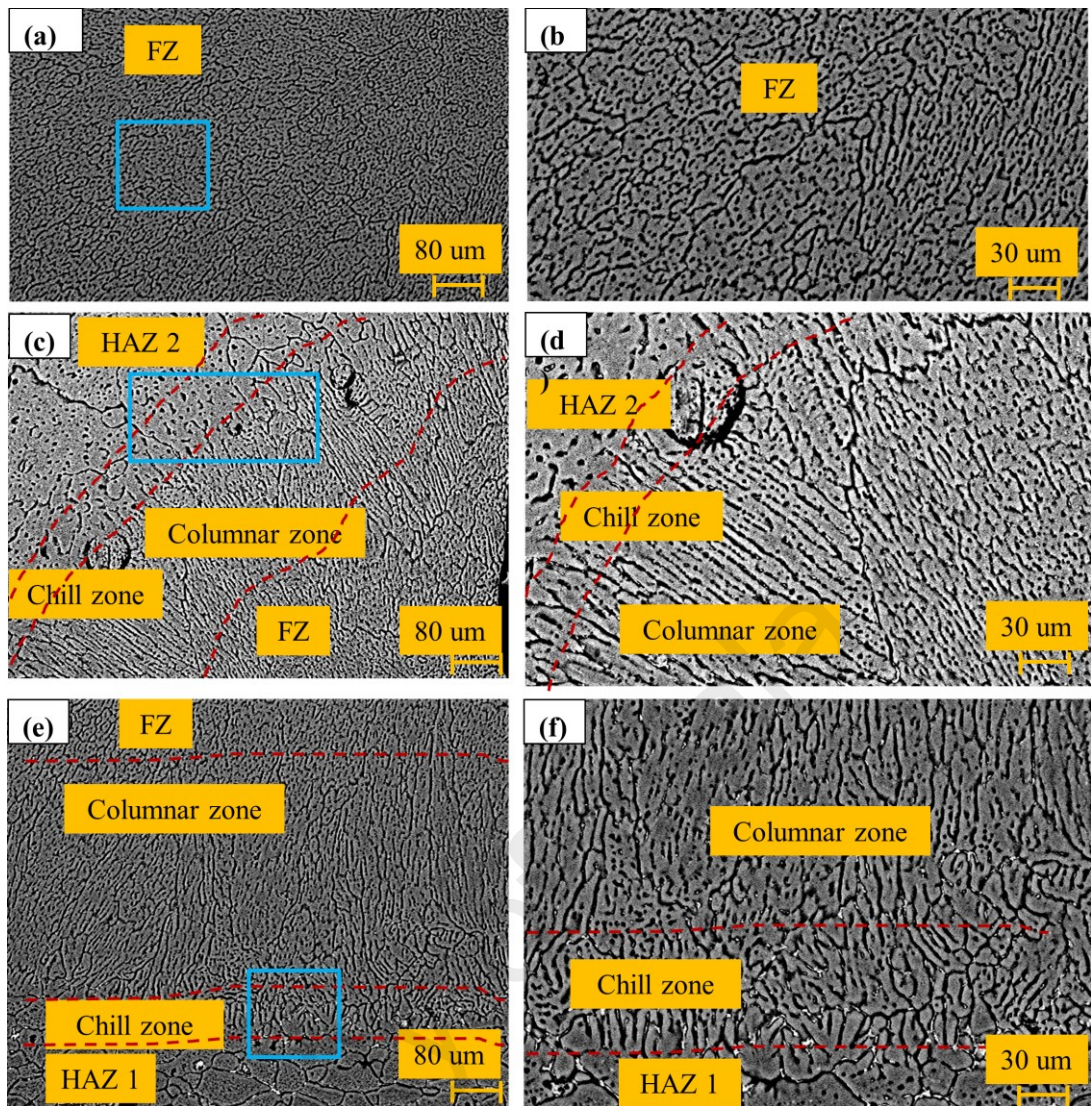
Figure 4.18: Sample C1: (a) SEM of FZ at 1000x magnification, (b) SEM of FZ at 2000x magnification, (c) SEM of FZ and HAZ2 at 1000x magnification, (d) SEM of FZ and HAZ 2 at 2000x magnification, (e) SEM of FZ and HAZ1 at 1000x magnification, (f) SEM of FZ and HAZ1 at 2000x magnification

Several distinct microstructural zones are identified starting from the FZ to the BM (dotted lines in Figure 4.18). It can be seen that the fusion zone microstructure differs from the base metal, having fine cellular-dendrite structures corresponding to high solidification rates, as shown in Figure 4.18(a) and Figure 4.18(b). Columnar zones are also observed, which are parallel dendrites, growing along the heat flow direction. The columnar zone direction follows the laser beam direction at the weld seam and the

differences in arrangements can be seen for HAZ1 and HAZ2 in Figure 4.18(c)-(f). In the FZ, the cellular dendrites are found to be shifting parallel to the dendrites near the end of the FZ. In the vicinity of the parallel dendrites, the aluminum alloys melted with a high undercooling level, forming fine equiaxed grains and creating a chill zone. Adjacent to the chill zone is the HAZ denoted by HAZ1 for BM AA2024-O and HAZ2 for BM AA7075-T6. The grains in HAZ were affected by the thermal cycle and were coarser than those in FZ. HAZ1 consisted of an over-aged zone where the precipitates were smaller than in HAZ2, which consisted of a partially melted zone. The HAZ1 region was at the border of BM AA2024, which had higher thermal conductivity that promoted the formation of smaller grains compared to the grains formed within the partially melted zone in HAZ2 near the border of BM AA7075-T6. These results are in good agreement with Min Li et al. (2011) and Sanchez-Amaya et al.'s (2009) findings from their respective studies (Li et al., 2011; Sanchez-Amaya, Delgado, De Damborenea, et al., 2009). Comparing with MIG welding, the grains formed within the weld bead are rather large due to slow cooling of the molten pool (Bradley & James, 2000). Therefore, it is proven laser welding gives stronger structure due to smaller grains.

4.3.5   EDX Analysis

The alloying elements in both alloys (Zn, Cu and Mg) resulted in precipitation hardening when heat from laser beam welding was applied. Figure 4.19 shows the EDX analysis of the skin up to the stringer for sample C1. The percentage of magnesium and zinc was lower whereas the percentage of copper was higher at skin level, indicating alloying elements in AA2024-O. Nearer to the weld zone, the percentage of zinc increased and the copper level decreased, indicating alloying elements in AA7075-T6.

The alloying elements appeared well-mixed during the process of laser welding, leading to precipitate hardening.
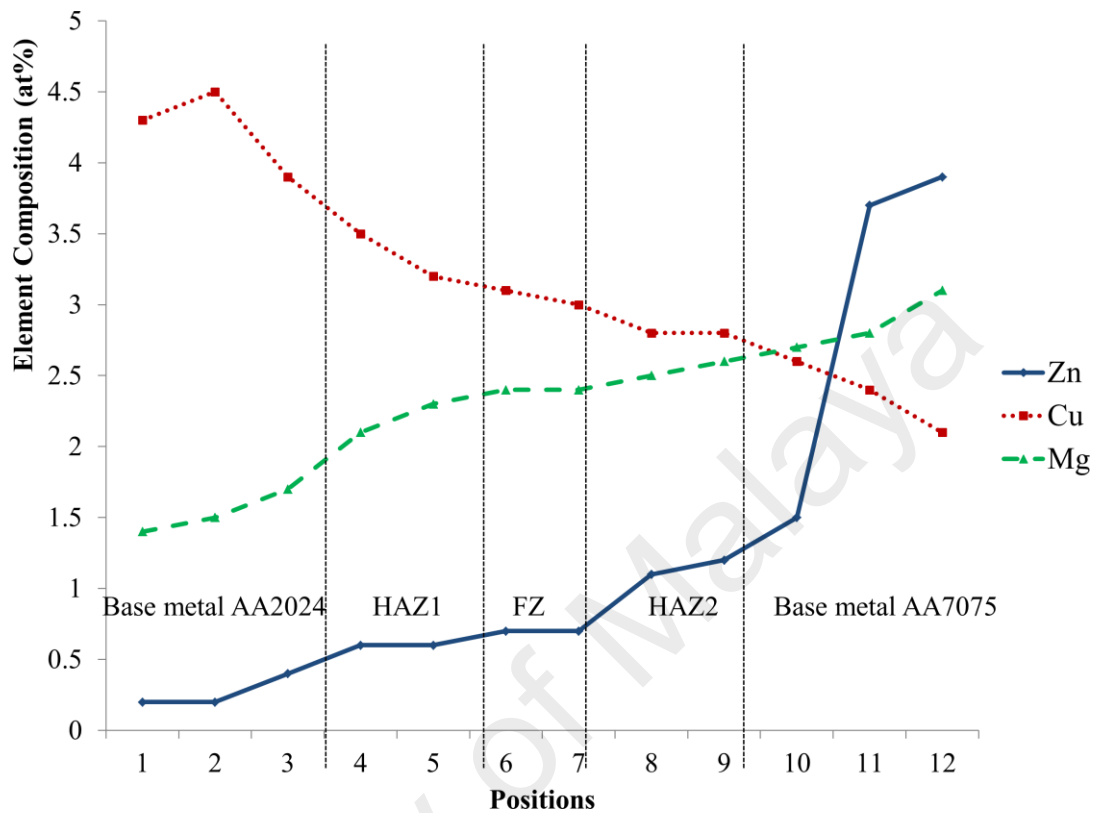
Figure 4.19: EDX analysis of alloying elements from the skin up to the stringer for sample C1

4.3.6 Weld bead microhardness measurement

Figure 4.20 depicts the effects of welding speed and focal distance on the hardness distribution of the weld bead. Hardness measurements were conducted across the entire length of the weld bead profile (including BM, HAZ and FZ). The Vickers hardness of the as received AA2024-O base material was approximately 60 HV, whereas that of the as received AA7075-T6 base material was about 100 HV. As welding speed increased, the FZ and HAZ1 hardness increased more than for the AA2024-O base metal. The two trends are evident from the results. For samples C1 to C5 the hardness values at the FZ and HAZ2 were lower compared to the AA7075-T6 base metal. Both the skin and

stringer were heat-treated by annealing prior to welding. The heat input from the laser beam resulted in smaller grain sizes in HAZ1 and coarser grains in HAZ2, in accordance with the respective BM thermal conductivities. Thus, the lower FZ hardness value than for AA7075-T6 base metal suggests that the laser welding reduced the effect of the original heat treatment of T6 (Sanchez-Amaya, Delgado, Gonzalez-Rovira, et al., 2009). The difference in hardness values for each zone was about 10 HV. Comparable studies have been conducted in the past to evaluate similar areas/zones for hardness measurement (Atabaki et al., 2014). Similar welding using MIG also proved there was not any improvement in the microhardness post welding. This proves that any techniques that induces heat to the workpiece will not improve the microhardness (Bradley & James, 2000).
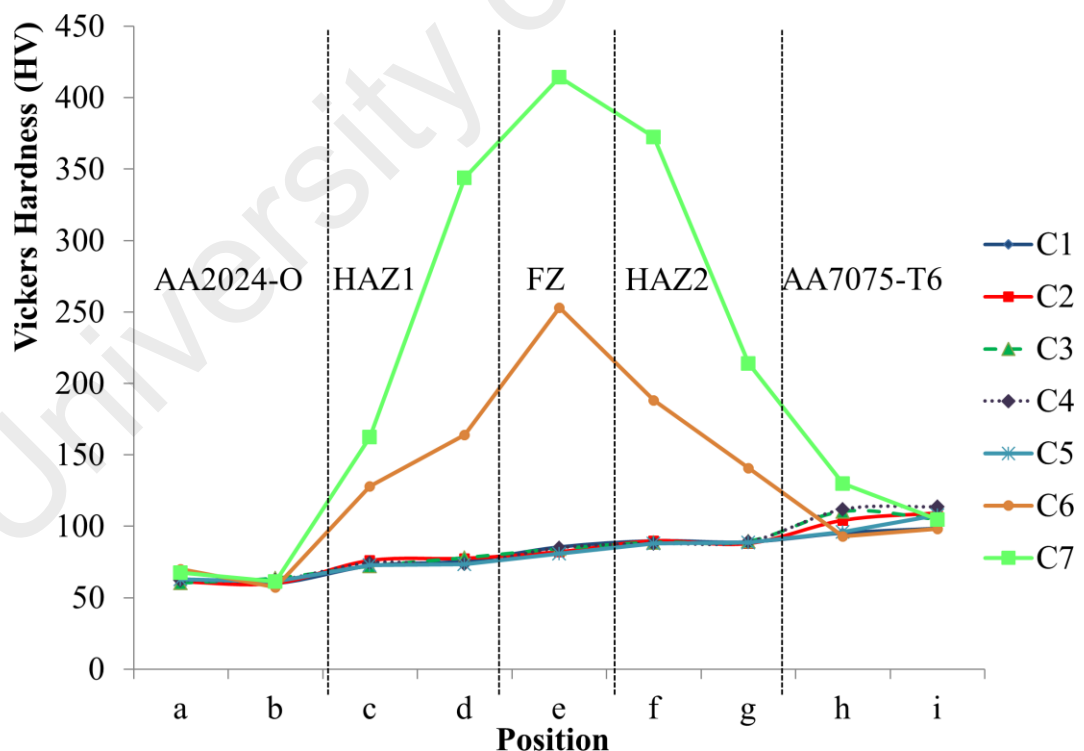
Figure 4.20: Vickers hardness for samples C1 to C7

All samples (C1 − C5) exhibited similar hardness results at different welding speeds (Figure 4.20). However, it seems the hardness results obtained at the joint areas were not satisfactory, thus a further study on focal distance was proposed to improve the results. Offsetting the focal distance to -1, as observed for sample C6, resulted in greater FZ hardness up to 253 HV. The hardness of HAZ1 also increased from 127 HV to 164 HV, while the hardness of HAZ2 increased from 140 HV to 188 HV for sample C6. An offset focal distance of +1 resulted in the highest hardness value of 414 HV in the FZ of sample C7. The HAZ1 hardness also increased from 162 HV to 344 HV, while the HAZ2 hardness increased from 214 HV to 373 HV. During laser welding of samples C6 and C7 the heat input calculated was 1078 J/mm, which was the lowest among all samples due to the larger beam diameter and high welding speed (18 m/s). This resulted in a fast cooling rate that led to the formation of a fine dendritic microstructure in the FZ (Ezazi et al., 2015). The results proved again that heat input has an important role in determining the weldment penetration. According to Equation 2.11, increasing the focal distance increased the laser beam diameter, resulting in lower heat input. In the upcoming subsection, filler alloy was added and experiments were redone to evaluate the influence of filler alloy and the improvement.

4.4 Part II: Double-sided laser welding of AA2024-O and AA7075-T6 with BA4047 filler alloy addition

According to the previous results, the influence of filler alloy is studied in this section. Filler alloy, BA4047 is added to evaluate the influence and the changes happened in the metallurgical and mechanical properties.

4.4.1 Pull test results and analysis

The preliminary experiments showed that C1 to C5 produced satisfying results with constant laser power and focal distance. In order to improve the mechanical properties and fracture force results, filler alloy was added to each side of the weld seam. Consequently, t-joints were successfully welded with low power fiber laser (270 W), welding speed from 9 mm/s to 21 mm/s and added filler alloy. Figure 4.21 shows the pull test results for samples welded with and without BA4047 filler alloy. From the comparison, fracture force was reportedly the highest when laser welding speed was 9 mm/s and filler was added. With the presence of filler, the fracture force increased from 643 N to 2704 N. As the welding speed increased, the fracture force reduced in both cases, with and without filler alloy (Y. W. Park et al., 2010). It was also observed that at each welding speed the fracture forces increased by approximately 250-350% when filler alloy was added.
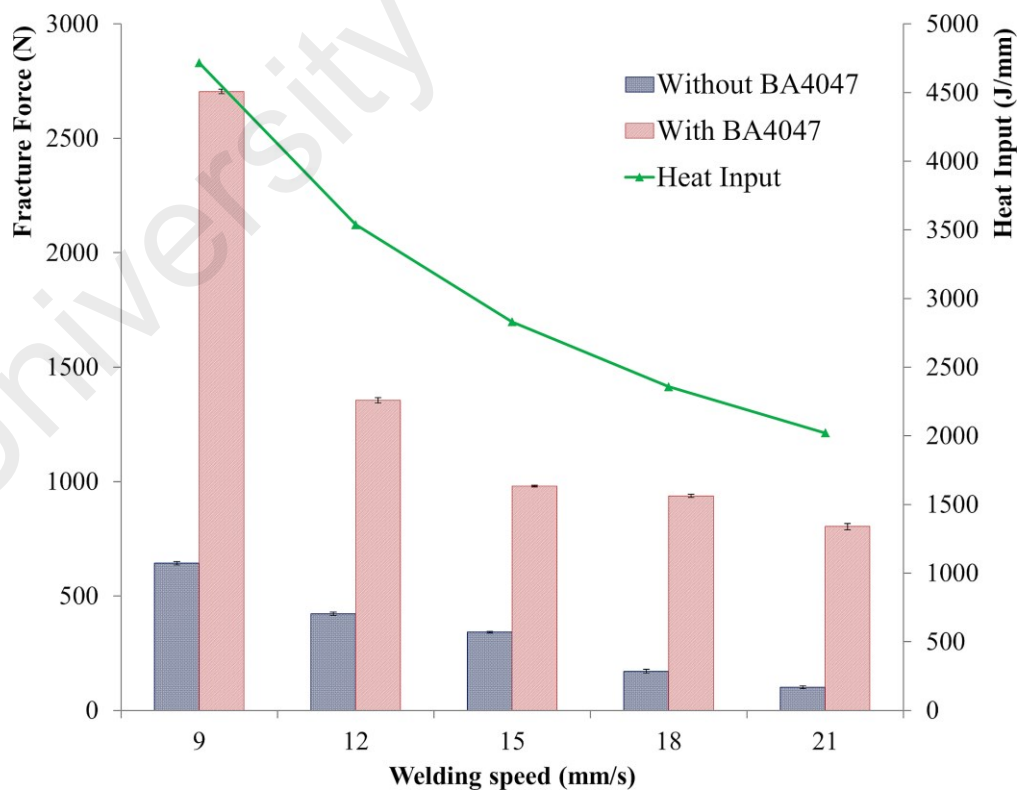
Figure 4.21: Fracture force and heat input at various welding speeds from 9 mm/s to 21 mm/s with and without filler

4.4.2   Metallurgical characterization

In previous studies, it has been shown that an optimal joint was made with low-power laser welding at 9 mm/s welding speed. Therefore, in the present study, the effect of BA4047 filler wire addition on weld geometry obtained using this optimal welding condition is examined and micrographs of a T-joint weld cross section are shown. Typical micrographs of weld cross sections at 9mm/s welding speed, with and without filler, are shown in Figure 4.22. For the same heat input of 4716 J/mm at 9mm/s welding speed and 270W laser power, the seam penetration seems to be deeper in a weld joint without filler addition. When filler was placed at the weld seam, the laser beam hit and melted the filler, hence less heat penetrated towards to workpiece. Therefore, the heat-affected zones were not as wide as those obtained for workpieces without filler, although the fracture force results showed that filler addition increased the weld joint strength. Generally, weld penetration did not influence the HAZ width. During laser beam welding, the filler wire was melted by direct laser irradiation. Therefore the laser's energy and power partially passed through the filler wire and created a molten pool. A mushroom plasma cloud also formed at the weld molten pool during laser welding, which was another source of melting energy. The filler melting behavior affects welding process stability, providing good appearance with continuous weld formation and less spatter (Tao et al., 2013). As seen in Figure 4.22, micro cracks and porosity are observed at the interface of the fusion zone and AA7075 base material when no filler was added during laser welding. In addition, a larger heat-affected zone and more metal vaporization are also noticed in the T-joint weld without filler wire. High level of Mg affected the metal vaporization in the AA7075 alloy. The T-joint welds with BA4047 filler wire appeared free from cracks and porosities with a smaller heat-affected zone and less metal vaporization. During the segregation of silicon from filler alloy to the grain boundary, the strengthening effect of intragranular reduced in the

weldment (D. Zhang et al., 2012). Therefore, it can be said that micro cracks and porosity were avoided with BA4047 filler wire due to the high silicon level from filler present in this alloy.
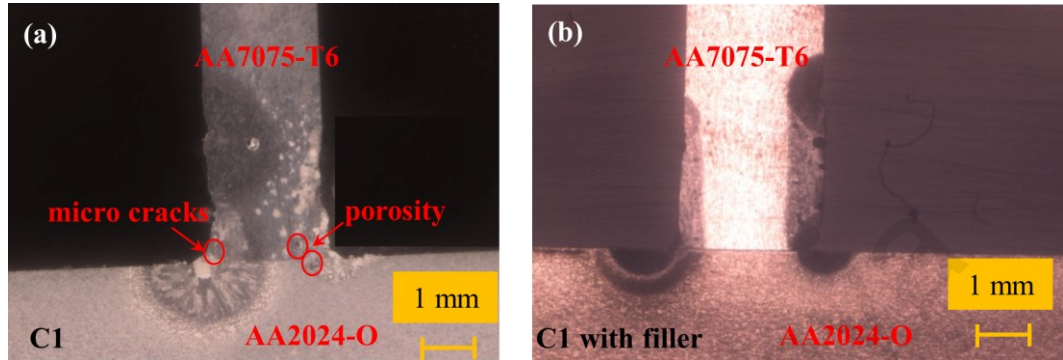
Figure 4.22: OM micrographs of sample at 9mm/s welding speed (a) without filler and (b) with BA4047 filler

4.4.3 Microstructural observation

Figure 4.23(a) illustrates a schematic of a welded T-joint consisting of distinct zones with different microstructures. In the present study, only the microstructure of the welded joint produced under optimized laser welding parameters (welding speed of 9 mm/s with BA4047 filler wire addition) is characterized, and the microstructure zones are shown in Figure 4.23(b)-(e). The HAZ between the FZ and the AA2024-O skin is denoted as HAZ1 while the heat-affected zone between the FZ and the AA7075-T6 stringer is denoted as HAZ2. The different microstructures are due to the different cooling rates and heat transfer directions realized in each zone. At the center of the fusion zone, cellular dendrites with formations of fine equiaxed grains (cellular zone) were observed due to the absence of a marked undercooling, as seen in Figure 4.23(c). From the FZ towards the fusion line near both HAZs, the microstructure changed from cellular dendrites to parallel dendrites (columnar zone) as seen in Figure 4.23(d) and Figure 4.23(e). It is also noticed that the parallel dendrites elongated along the heat flow

direction during laser welding, which is the thermal gradient direction. The morphology of the solidification structures developed in the fusion zone was controlled by parameter GL/R, where GL is the thermal gradient in the liquid and R is the solidification growth rate (Yang et al., 2012). According to the literature by Yang et al. (2012) parameter GL/R varies from a minimum value at the FZ to a maximum value near the HAZ, leading to a change in microstructure from equiaxed dendrites to parallel dendrites, which is in accordance with the results. Besides, coarsened grain boundaries were observed adjacent to the fusion line in both HAZs, indicating the partial melting of the base aluminum alloys near the fusion line during laser welding.
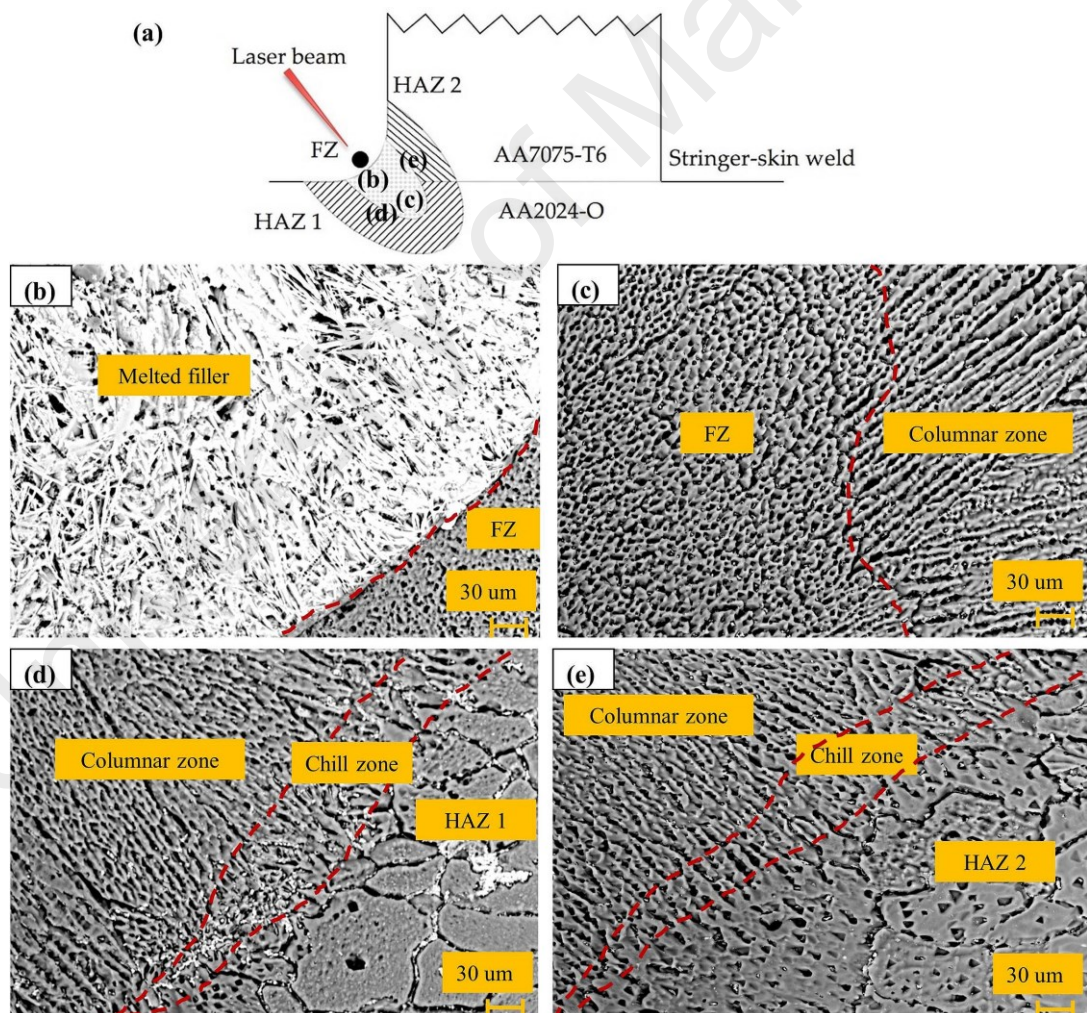
Figure 4.23: Welding speed of 9 mm/s with BA4047 filler; (a) schematic diagram of FZ, HAZ1 and HAZ2, (b) SEM of filler and FZ at 2000x magnification, (c) SEM of FZ at 2000x magnification, (d) SEM of FZ and HAZ 1 at 2000x magnification, and (e) SEM of FZ and HAZ2 at 2000x magnification

4.4.4 Weld bead microhardness measurement

Figure 4.24 shows the effects of welding speed on the hardness distribution of the welded bead at 9 to 21mm/s welding speeds with BA4047 filler addition. The microhardness measurements were conducted across the entire length of the weld bead profile, including the base metal, heat-affected zone and fusion zone. The hardness distribution for the workpiece without filler was similar at all welding speeds as discussed in section 4.3.6, but when filler was added, the microhardness changed at different welding speeds. The base materials of AA2024-O and AA7075-T6 had approximately 60 and 100 HV Vickers hardness, respectively as discussed earlier. With increasing welding speed, filler addition improved the hardness throughout the FZ, HAZ1 and HAZ2. The highest microhardness value of 668 HV in the FZ was obtained at welding speed of 9 mm/s, which is 1200% higher than for samples without filler. When filler was not added, the hardness value in the FZ and HAZ2 were lower compared to the AA7075-T6 base metal. This is because both skin and stringer in this study were heat-treated by annealing prior to welding. The lower hardness value in the FZ compared to the AA7075-T6 base metal suggests that the laser welding reduced the effect of the original heat treatment of T6 (Sanchez-Amaya, Delgado, Gonzalez-Rovira, et al., 2009). The elevated temperatures in the zones cause microstructural modifications (Pinto et al., 2010). Therefore, the grain refinement with reduced solidification shrinkage and an increased interdendritic liquid quantity with high content of silicon has increased microhardness after welding (Holzer et al., 2015). Increased microhardness is recommended during laser welding as it improves the mechanical properties of weldment.
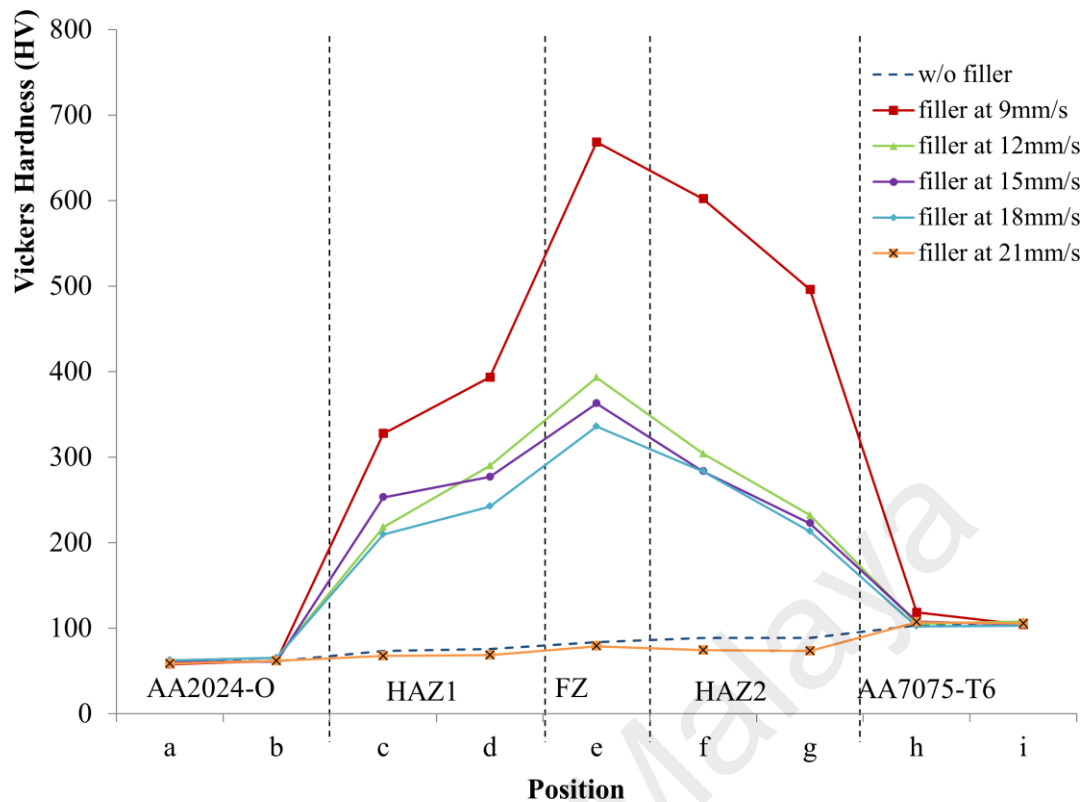
Figure 4.24: Microhardness of workpiece with and without filler at various welding speeds

4.4.5 Influence of filler alloy addition on experimental results

Overall, better results were obtained with filler addition for both pull and microhardness tests. High silicon content in combination with low magnesium and copper content of this alloy supports the prevention of hot cracks during welding (Ion, 2000). Laser welding induces high power density, which causes the vaporization of alloying elements, magnesium. This is because these elements have low fusion points and higher equilibrium vapor pressure than the aluminum base material. Vaporization can happen in keyhole as well as conduction welding. The vaporization mechanism has three levels. In the first level, the vaporization element is transported from the bulk to the molten weld pool surface. In the second level, vaporization happens at the liquid-vapor interface, meanwhile in the third level, the vaporized elements are transferred to the surrounding gas phases. However, by controlling the power density during laser

welding can minimize alloying element loss from the influence of the molten metal temperature in the welding pool (Cao et al., 2003a, 2003b). As a secondary option, the losses can be reduced by adding filler material to the gap. This can control the weld bead's metallurgy and guarantee weld quality (Ion, 2000). The low viscosity in this filler decreases the superficial tension of the molten pool and subsequently reduces hot cracking (Cicala et al., 2010). Using filler wire enables the compensation of volume loss generated by evaporation and spatter formation during laser welding (Pinto et al., 2010). With the addition of filler alloy, the fracture force and microhardness results improved, leading to better weld strength properties compared to the studies without filler alloy.

4.5 Heat input calculation for preliminary testing of single-sided laser welding of Ti6Al4V and Inconel 600

Figure 4.25 and Figure 4.26 show the heat input of 200 W to 280 W at overlapping factors of 10% to 60% for dissimilar materials Ti6Al4V and Inconel 600 at fixed welding speeds of 40 mm/s and 50 mm/s respectively. The same as the previous graph in Figure 4.1, the green boundaries show sound joint weldment. According to this graph, a preliminary test was done and suitable parameters were chosen to run the experiments. For each input combination, the heat input was calculated using Equation 2.11, similar to Figure 4.1, where the heat input is inversely proportional to welding speed. Therefore, higher welding speed gives lower heat input.
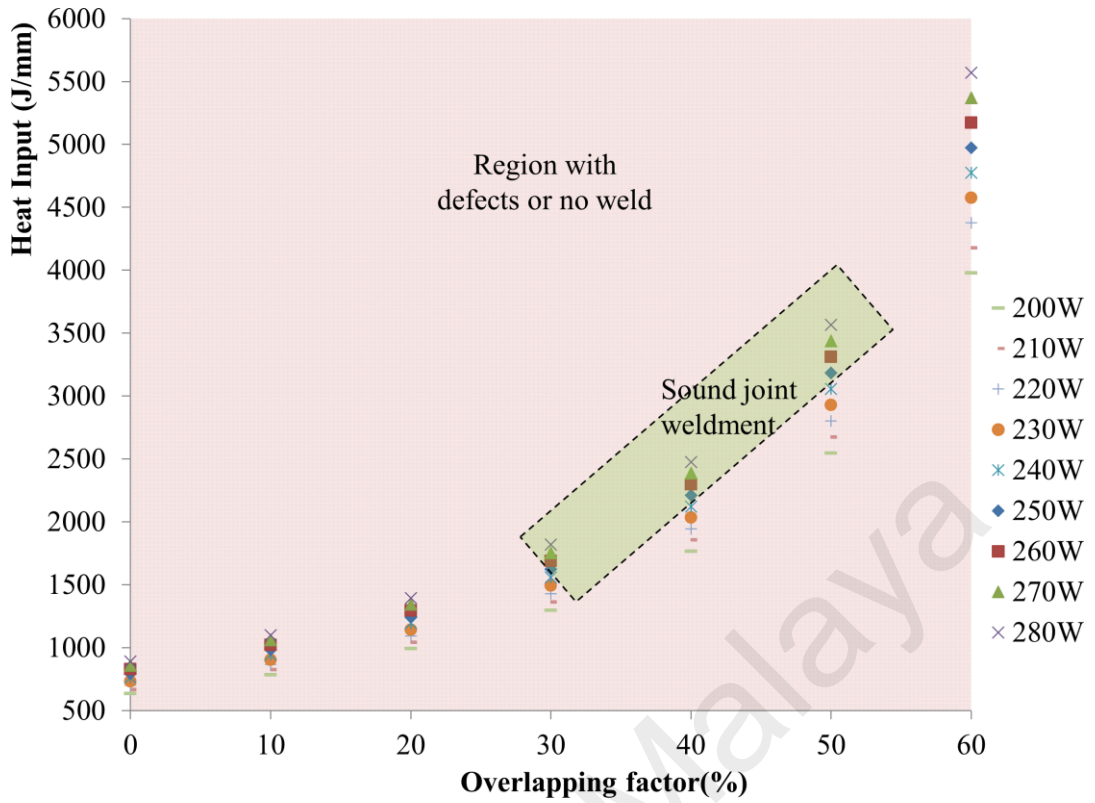
Figure 4.25: Heat input calculated for Ti6Al4V and Inconel 600 at welding speed of 40 mm/s
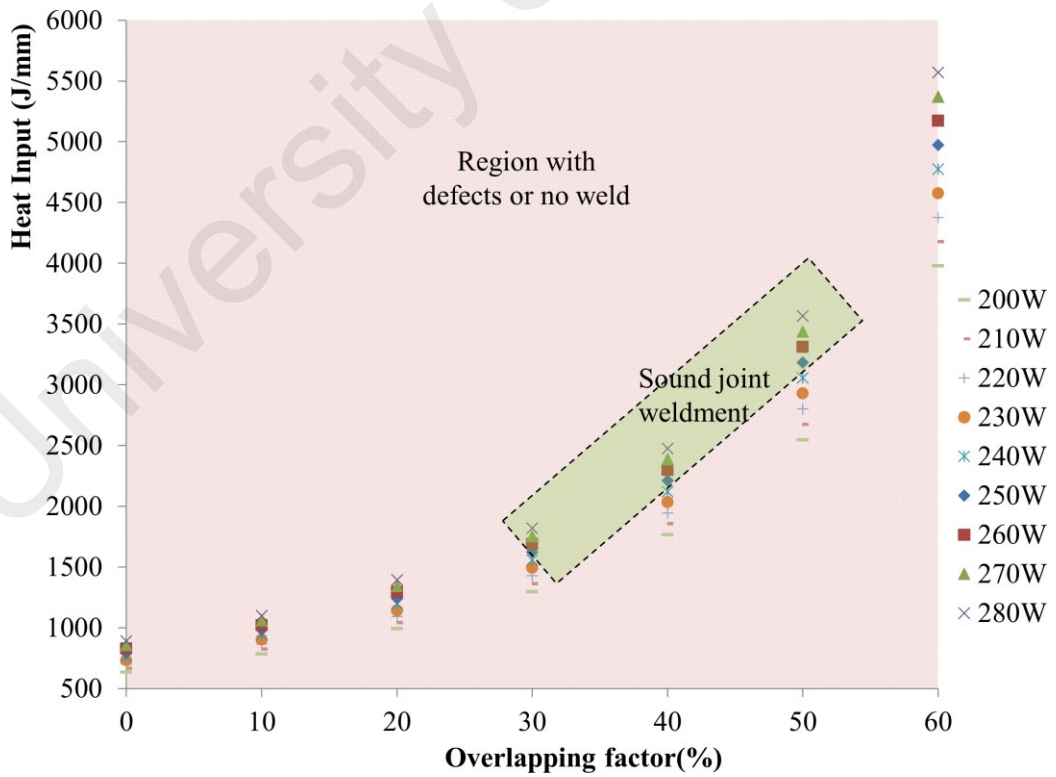
Figure 4.26: Heat input calculated for Ti6Al4V and Inconel 600 at welding speed of 50 mm/s

4.6 Part III: Single-sided laser welding of Ti6Al4V and Inconel 600

According to Figure 4.25 and Figure 4.26, preliminary testing was done to narrow down the parameters for single-sided laser welding of Ti6Al4V and Inconel 600.

4.6.1 Pull test results and analysis

Table 4.4 presents the list of parameters selected for preliminary testing to determine the most suitable parameters for metallurgical and microhardness analysis of laser welding Ti6Al4V and Inconel 600. The effects of overlapping factor and welding speed on the weld bead's fracture force are presented in Figure 4.27 and Figure 4.28.

Table 4.4: Preliminary parameters for welding Ti6Al4V and Inconel 600

No.	Power (W); P	Welding Speed (mm/s); v	Overlapping factor (%); η
D1	250	40	30
D2	250	40	40
D3	250	40	50
D4	260	40	30
D5	260	40	40
D6	260	40	50
D7	270	40	30
D8	270	40	40
D9	270	40	50
E1	250	50	30
E2	250	50	40
E3	250	50	50
E4	260	50	30
E5	260	50	40
E6	260	50	50
E7	270	50	30
E8	270	50	40
E9	270	50	50
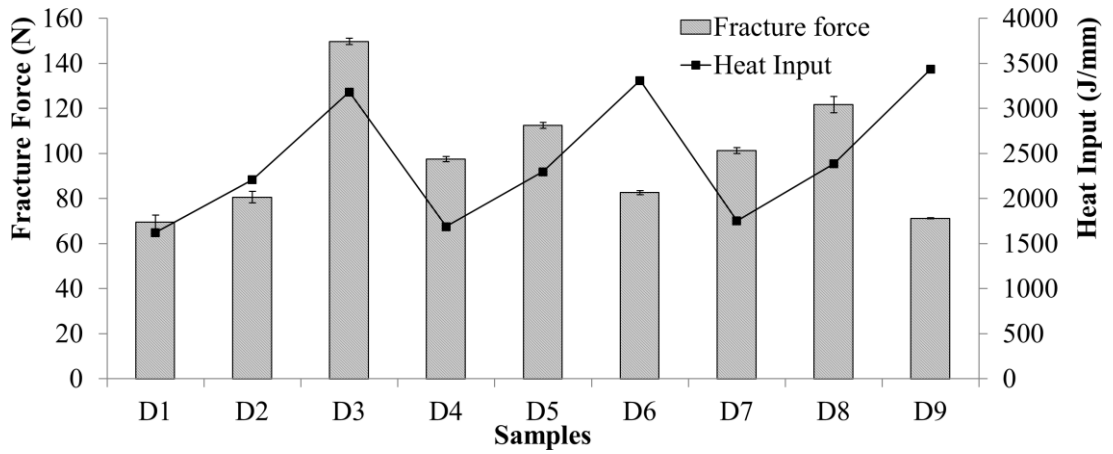
Figure 4.27: Fracture force needed to break samples and heat input for samples D1 to D9
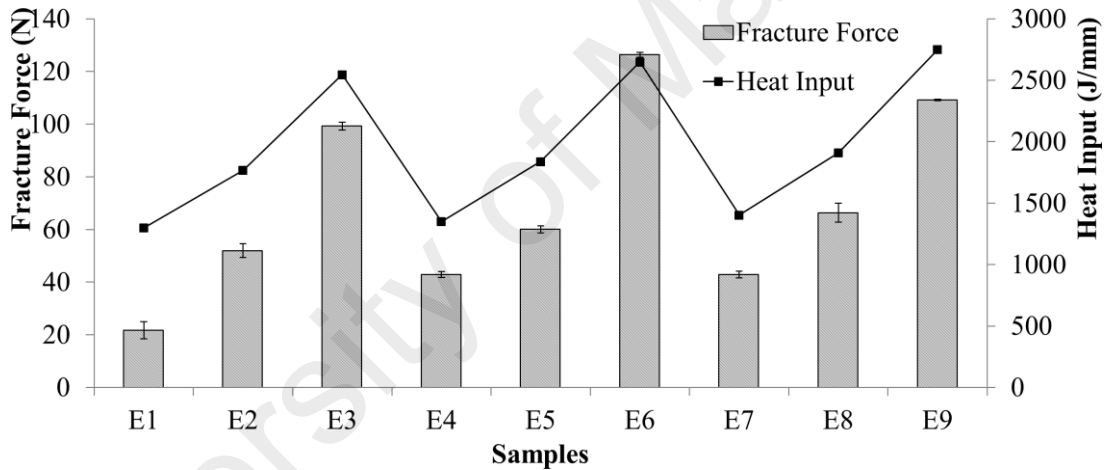
Figure 4.28: Fracture force needed to break samples and heat input for samples E1 to E9

By comparing the samples, it is noticed that the fracture force increased with increasing overlapping factor, as observed in D1 to D3, E1 to E3, E4 to E6 and E7 to E9. However, as the heat input increased with increasing laser power, the fracture force reduced due to metal evaporation. High heat input produced defects that led to weak joints and less force, as seen in samples D4 to D9. For high overlapping or lower welding speeds, the affected areas are exposed to more accumulated heat input that

would result in increased facture force. However, when both laser power and overlapping factors are high, the accumulated heat would tend to create cracks during solidification (Gao et al., 2014; Ribic et al., 2009). Samples D1, D2, D3 and E3 were chosen for metallurgical characterization and microhardness analysis. Meanwhile, the opposite trend was observed regarding the effect of welding speed, whereby the force needed to fracture the samples decreased with increasing welding speed. Figure 4.29 shows the optical microscope images for fracture at skin for sample D3 (Figure 4.29(a)), fracture at stringer for sample D3 (Figure 4.29(b)), fracture at skin for sample E1 (Figure 4.29(c)) and fracture at stringer for sample E1 (Figure 4.29(d)). The details in the image indicates (i) fracture hole seen due to strong weldment, (ii) fractured debris attached to stringer, (iii) not fully melted sample leaving residue of weldment and (iv) some part of fractured debris attached to stringer.
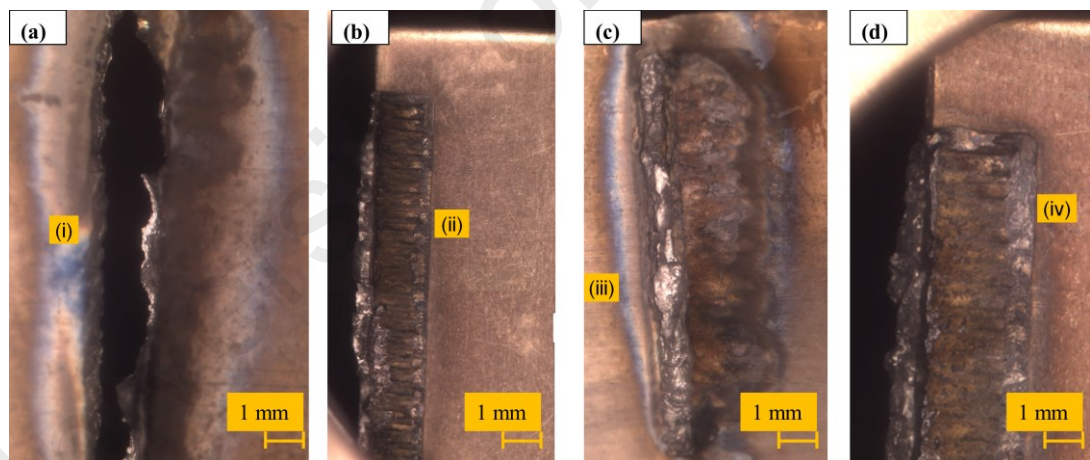
Figure 4.29: Optical microscope (a) Fracture at skin for sample D3 (b) Fracture at stringer for sample D3 (c) Fracture at skin for sample E1 (d) Fracture at stringer for sample E1

The maximum force was achieved for sample D3 when the overlapping factor was 50% and the welding speed was 40 mm/s at a constant power of 250 W. The increase in force was mainly because laser welding at higher overlapping factor and lower welding

speed induced greater heat input and thus a wider fusion zone with deeper penetration that requires higher breaking force. The experiments were performed in two separate series to investigate the overlapping factor and welding speed effects on weld quality. Even though the thickness of samples were thin (less than 0.8mm for Ti6Al4V), the residual stress was negligible as the welded samples were not warped at obvious angles.

4.6.2   Fuzzy smart model for selecting parameter range

A fuzzy logic model for selecting a range of parameter in single-sided laser welding of Ti6Al4V and Inconel 600 was developed successfully from the pull test results. The effects of laser power, welding speed and overlapping factor were used to determine the weldment penetration strength. The heat input gained during laser welding affects the weld joint's strength, which is subsequently influenced by varying the welding parameters (Unt & Salminen, 2015). Twenty-four (24) experiments were carried out, of which eighteen (18) were used for training from Table 4.4 and the remaining six (6) were applied to test and validate the smart model developed. Table 4.5 shows the testing parameters that were chosen randomly to determine the effectiveness of this fuzzy logic model for single-sided laser welding of Ti6Al4V and Inconel 600.

Table 4.5: Parameters tested after fuzzy logic model was developed for single-sided laser welding Ti6Al4V and Inconel 600

No.	Power (W); P	Welding Speed (mm/s); v	Overlapping factor (%); η
1	255	45	50
2	258	45	40
3	265	40	45
4	263	40	37
5	260	43	48
6	268	49	45

Figure 4.30 and Figure 4.31 shows the differences between the experimental training and testing data with predicted values and error percentage respectively. Relative errors, ε as discussed in Equation 3.5 were calculated for training and testing data. The values were 6.95% and 3.20% respectively with the calculation shown in Equation 4.3 and Equation 4.4. The relative error is less than 10% and considered acceptable, as supported by Nukman, Y. et al. (2013) (Nukman et al., 2013).

$$\varepsilon_{training} = \sum_{i=1}^{18} \left| \frac{\overline{x_i} - \widehat{x_i}}{\overline{x_i}} \right| \ x \ \frac{100\%}{18} \qquad = \frac{1.251}{18} \ x \ 100 = 6.95\% \qquad \text{(Eq.4.3)}$$

$$\varepsilon_{testing} = \sum_{i=1}^{6} \left| \frac{\overline{x_i} - \widehat{x_i}}{\overline{x_i}} \right| \ x \ \frac{100\%}{6} \qquad = \frac{0.192}{6} \ x \ 100 = 3.20\% \qquad \text{(Eq.4.4)}$$

where $\widehat{x_i}$ is fuzzy logic predicted value, $\overline{x_i}$ is the average of the experimental value.
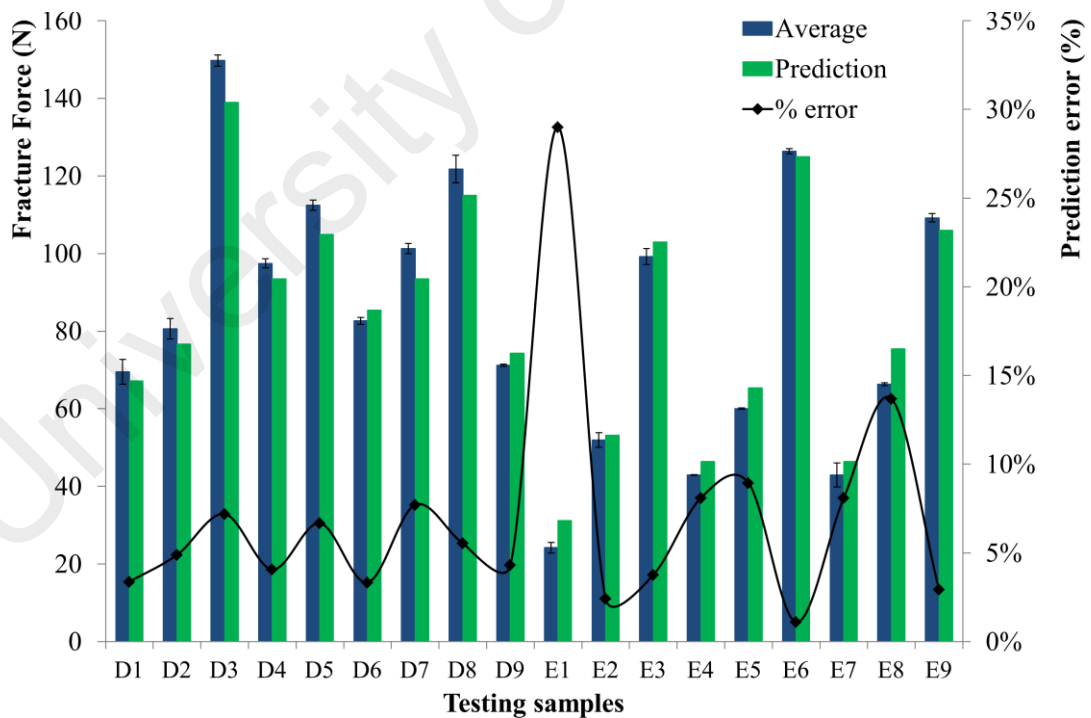
Figure 4.30: Training results and fuzzy logic prediction values in terms of prediction error percentage for single-sided laser welding of Ti6Al4V and Inconel 600
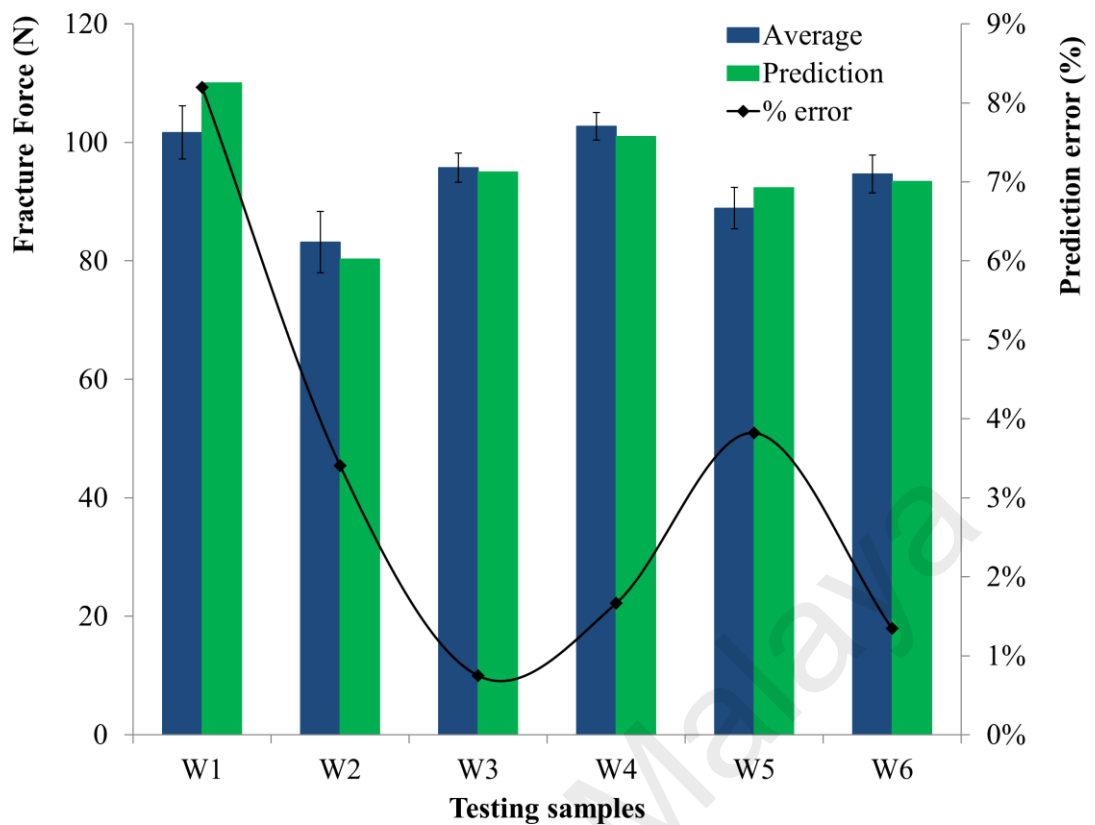
Figure 4.31: Testing results and fuzzy logic prediction values in terms of prediction error percentage for single-sided laser welding of Ti6Al4V and Inconel 600

By comparing samples W1 to W6, higher laser power with moderate or high overlapping factor would reduce fracture force, conforming to previous explanations. Regression graphs were plotted to compare both experimental and prediction values obtained (Figure 4.32). The graphs show that the goodness of fit (R^2) values for training and testing were 0.9849 and 0.8404 respectively.
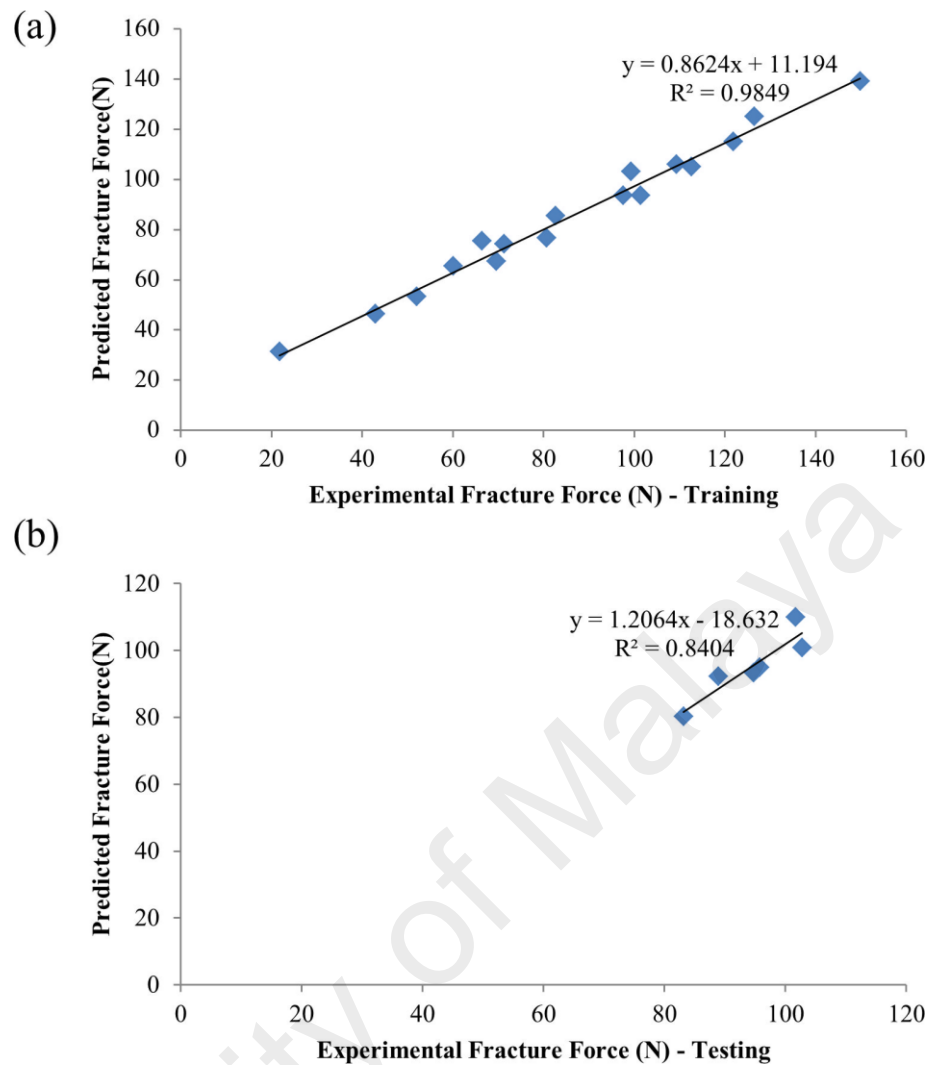
Figure 4.32: Correlation between experimental and fuzzy logic predictions of fracture force (N) in (a) training and (b) testing

From the surface plot in Figure 4.33 it is possible to determine the factors that influence fracture force. According to Figure 4.33(b) and (c), increasing the overlapping factor increased the weld strength, which led to higher fracture force. When the welding speed decreased, the fracture force increased due to the higher heat input generated and stronger weld penetration (Figure 4.33(a) and (c)). Increasing the laser power increased the fracture force, as seen in Figure 4.33(a) and (b). Overall, the overlapping factor had the highest influence on determining the fracture force, followed by welding speed and

laser power. Prediction was generally successful and the next evaluation can be done. From this fuzzy logic model, a range of parameters was chosen to do next evaluation.
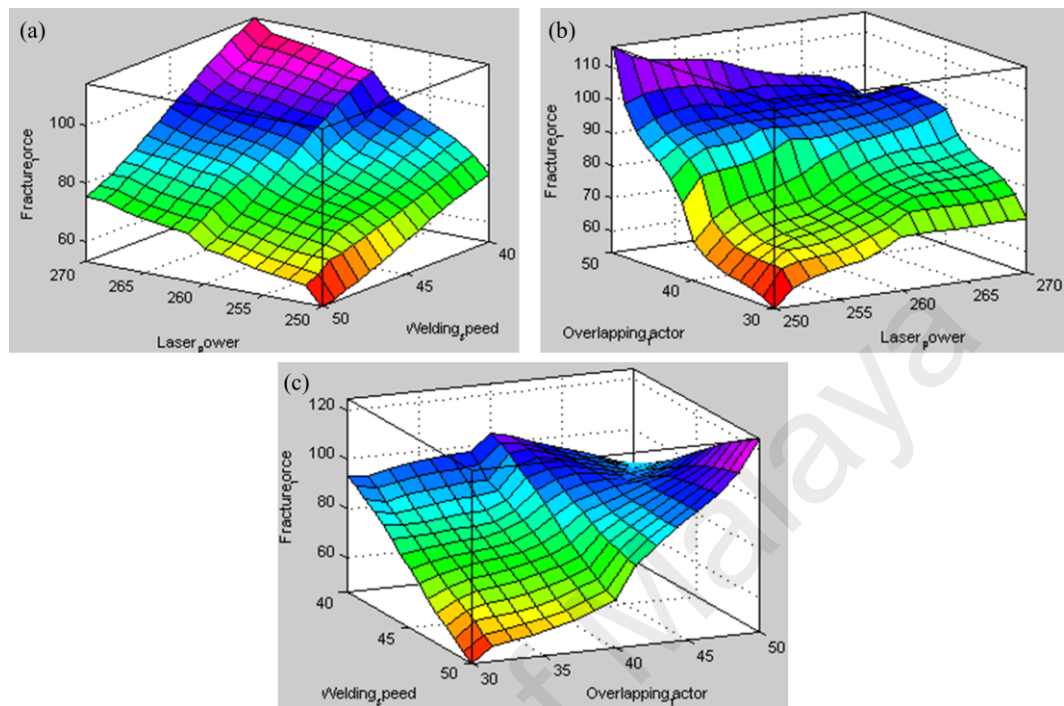
Figure 4.33: Control surface of the fuzzy inference system: effect of (a) laser power and overlapping factor on fracture force; (b) laser power and welding speed on fracture force; (c) welding speed and overlapping factor on fracture force

.

4.6.3   Metallurgical characterization

Optical micrographs of the weld bead cross sections of samples D1, D2, D3 and E3 are presented in Figure 4.34 to evaluate the influence of overlapping factor and welding speed when the laser power is constant. An asymmetric welding seam was observed in every sample because only one side was welded. The welded area where the laser beam was introduced exhibited a concave shape, whereas a slightly convex shape was observed in the non-welded area. This observation is typical for single-sided laser welding and has been reported in other studies (Enz et al., 2015). As shown in Figure 4.34, the weld pools displayed a certain asymmetry and a greater extent of melting was observed on the Ti6Al4V skin. This is because the thermal diffusivity of Ti alloy is

lower than Ni alloy, resulting in localized heating and greater melting of Ti6Al4V during welding (Chatterjee et al., 2008).
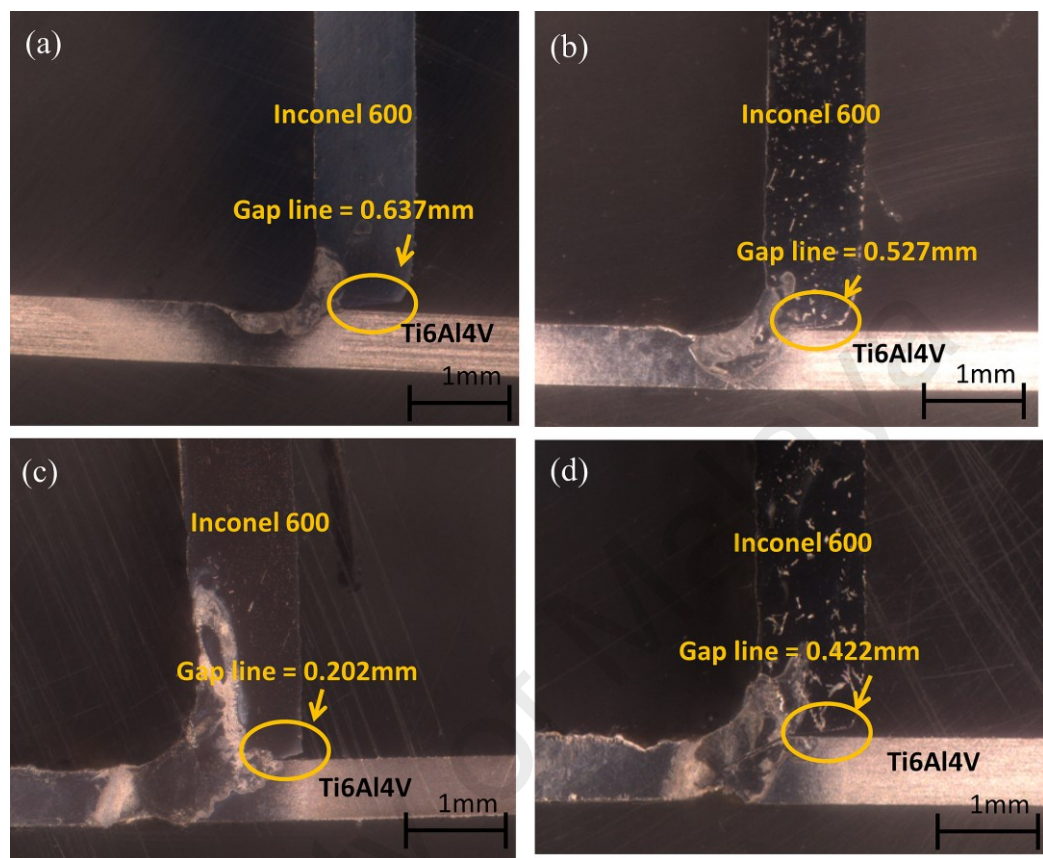
Figure 4.34: Optical micrographs of samples (a) D1, (b) D2, (c) D3 and (d) E3

A sound joint was obtained when the welding speed was 40 mm/s and the overlapping factor was 50%. This is proven by the minor gap line of 0.202 mm indicated by sample D3 in Figure 4.34(c). However, decreasing penetration depth and increasing gap line length were observed on the weld bead samples D1, D2 and E3, which possessed either lower overlapping factors or higher welding speeds. The gap lines were 0.637 mm, 0.527 mm and 0.422 mm long for samples D1, D2 and E3, respectively. Therefore, it can be concluded that the gap line length increased and the penetration depth decreased as the welding speed increased (comparing samples D3 and E3) while the overlapping factor decreased (comparing samples D1, D2 and D3).

Optimum welding was achieved for sample D3 because the heat input in this welding condition was sufficient to produce a sound T-joint with satisfactory penetration between the skin and stringer. The amount of heat input reportedly determines the degree of dilution and cooling rate in the weld. Insufficient heat input during the welding process results in a faster cooling rate, thus causing limited melting between the skin and stringer and thereby leading to insufficient penetration. Heat input is critical in defining the joint's geometry and can be manipulated by varying the welding parameters (Unt & Salminen, 2015).

Moreover, the color of the Ti6Al4V base metal remained consistent for all samples, whereas color variation was observed on the Inconel 600 base metal from one sample to another as indicated in Figure 4.34. The reason for this is that Kroll's reagent is a recommended etchant for titanium alloys but not for nickel alloys. It has been reported that the nitric acid in Kroll's reagent acts as an oxidizing agent and reacts with the nickel in Inconel 600 to produce Ni^{3+}. Therefore, it can be inferred that the color variation of Inconel 600 is due to the intensity difference of Ni^{3+} production (Rebak & Crook, 2000).

Among the parameters, laser welding speed and laser beam overlapping factor are commonly referred to as the most notable variables affecting the heat input. In this study, the heat input is calculated according to the previous Equation 2.1 and 2.11. From the equations, it is theoretically shown that the reduced laser beam diameter and welding speed increase the heat input. It is also noted that the laser beam diameter is directly affected by the overlapping factor and this relation is explained in Figure 4.35. The laser beam diameter decreases when the overlapping factor increases, thus increasing the heat input accumulated in the welded area (Gao et al., 2014; Ribic et al., 2009).
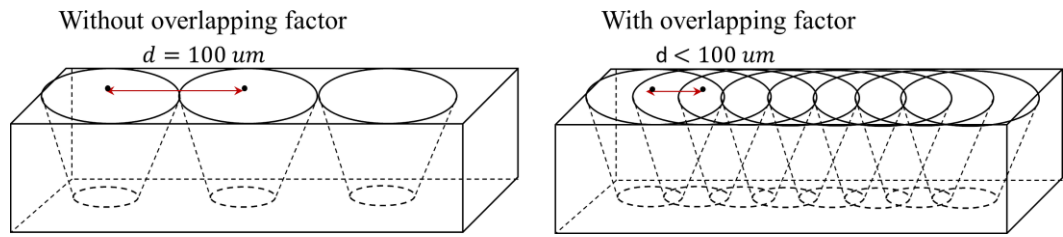
Figure 4.35: Schematic diagram showing the effect of the overlapping factor on laser beam diameter

4.6.4 Weld bead microstructural observation and elemental composition analysis

Inconel 600 alloy has an average grain size of 19 μm (±3μm) while Ti6Al4V has an average grain size of 20 μm (Rotella & Umbrello, 2014). Figure 4.36 shows the microstructure of the interface between the FZ and HAZ of Ti6Al4V (denoted as HAZ1) and Inconel 600 (denoted as HAZ2) of all sample cross sections. As seen in Figure 4.36, the grains generally become notably finer in the HAZ compared to the grains in the base metals, indicating a large thermal gradient in the FZ and HAZ interface during laser welding. The measured grain size in HAZ2 at the Inconel 600 side was 6.5 μm (±1μm) on average, which is a reduction of 65% from the original grain size; the grain size measured in HAZ1 for Ti6Al4V was 8.2 μm (±2.5μm) on average, which is a reduction of 59%. Grain size was measured using ImageJ software. Such phenomenon can be attributed to rapid solidification when the grain size in the microstructure is rather small (Norris et al., 2011). In the FZ, an equiaxed pattern is observed as the grain size is smaller due to rapid melting and solidification. The fusion zone has a similar identification of columnar beta grains of Ti that occur in two-dimensional heat flow condition (Donachie, 2000).
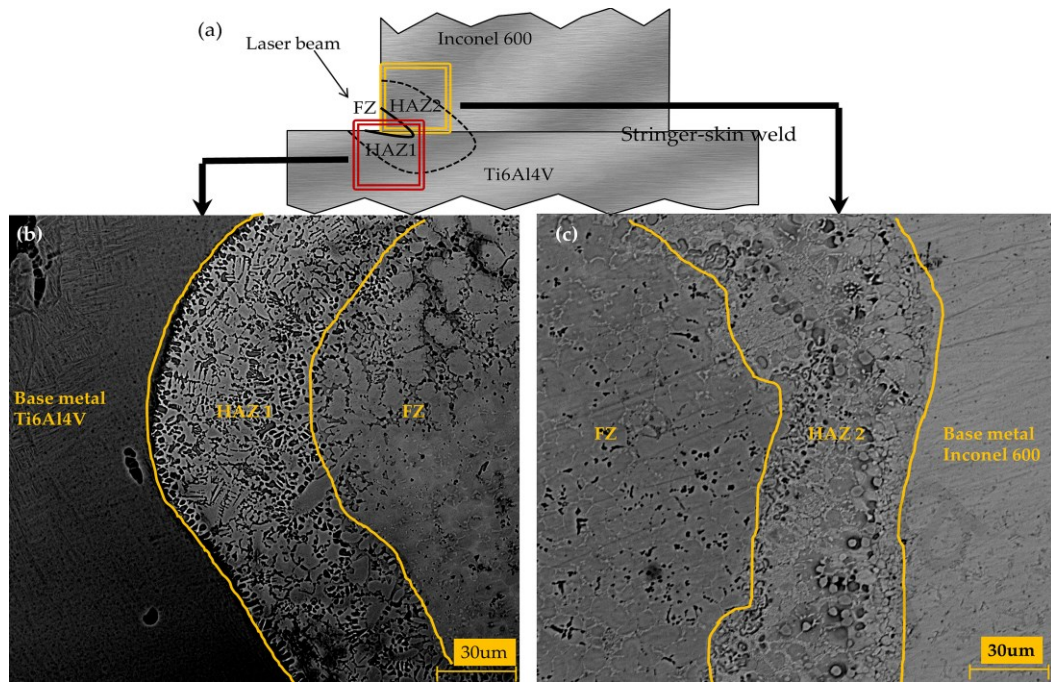
Figure 4.36: (a) Schematic diagram of the FZ, HAZ1, HAZ2 and base of samples; SEM micrographs of sample microstructures: (b) D3 for FZ, HAZ1 and Ti6Al4V base metal, (c) D3 for FZ, HAZ2 and Inconel 600 base metal.

4.6.5 EDX analysis

The NiTi and NiTi$_2$ patterns prove the formation of these elements during laser welding of nickel-based alloy and titanium-based alloy. The EDX results also prove the existence of NiTi and NiTi$_2$. According to the Ni-Ti phase diagram, the NiTi phase was produced in the primary crystallization from the melt and the NiTi$_2$ phase was formed from the peritectic reaction with the NiTi phase, while the cooling after columnar dendrite melting indicates NiTi (Sudarshan, 2007). As shown in Figure 4.37 and Table 4.6, point A has nearly the same percentage of Ni and Ti, proving the NiTi presence; the structure at point B shows a Ti-to-Ni ratio of 2:1, therefore signifying the presence of NiTi$_2$. NiTi$_2$ is detected towards the sample weld pool due to the lower heat input, which allowed phase formation. Meanwhile, NiTi was detected in all samples (Figure 4.37). A similar study was done by Chatterjee et al.(2006) to determine the patterns of NiTi and NiTi$_2$ (Chatterjee et al., 2006). The phases were detected at the weld pool

116

beside the HAZ of Inconel 600. Due to lower thermal diffusivity, Ti flows from Ti6Al4V towards the weld pool and reacts with the Ni from Inconel according to Equations 4.5 and 4.6.

$$Ni^+ + Ti^+ \rightarrow NiTi \tag{Eq.4.5}$$

$$Ni^+ + 2Ti^+ \rightarrow NiTi_2 \tag{Eq.4.6}$$

This observation is further corroborated by the EDX analysis presented in Table 4.6, where the atomic percentage of Ni and Ti for each sample is determined to identify the presence of NiTi and $NiTi_2$. Other alloying element such as vanadium, aluminum, chromium and iron did not involve in the intermetallic phase formation.

Table 4.6: The elemental atomic weight percentage with a phase in D1, D2, D3 and E3

Point	Ni (at. %)	Ti (at. %)	V (at %)	Al (at. %)	Cr (at. %)	Fe (at. %)	Total (%)	Phase
A	39.5	40.5	3.4	5.4	7.7	3.5	100.0	NiTi
B	28.4	56.4	3.3	5.3	3.6	3.0	100.0	$NiTi_2$
C	42.1	38.9	3.2	4.0	8.3	3.5	100.0	NiTi
D	40.5	40.9	3.5	3.9	8.1	3.1	100.0	NiTi
E	39.4	40.6	3.3	4.4	7.6	4.7	100.0	NiTi
F	29.1	55.4	3.5	6.0	3.3	2.7	100.0	$NiTi_2$
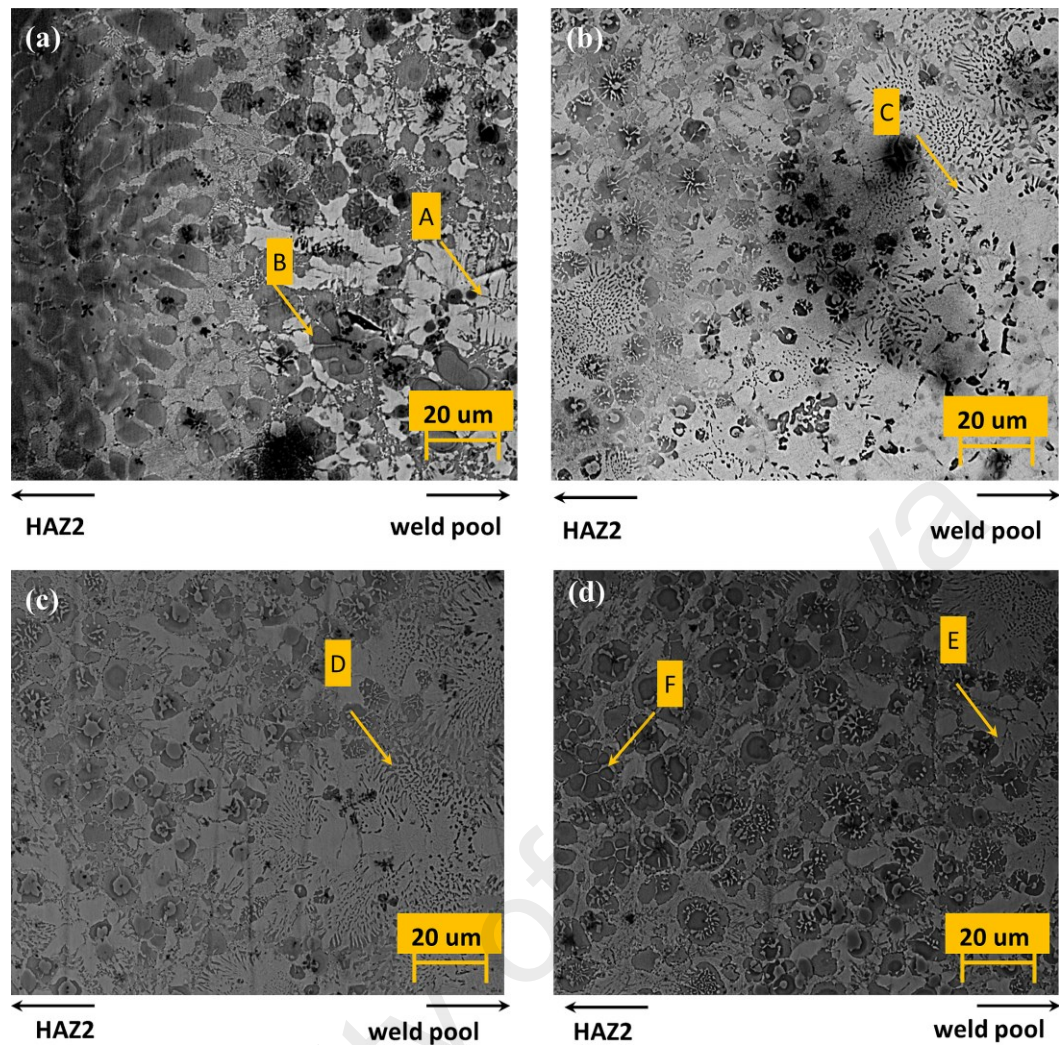
Figure 4.37: SEM micrographs of NiTi and NiTi2 intermetallic compounds formed in the FZ in samples a) D1, b) D2, c) D3 and d) E3

4.6.6 XRD analysis

The Ti–Ni system had different conductivities of $\kappa_{Ni} \approx 4\kappa_{Ti}$, resulting in a Ti-rich melt pool with metallurgical dissimilarity. Due to the differences in thermal diffusivity and conductivity, Ti from Ti6Al4V flowed towards the weld pool and reacted with Ni from Inconel. This resulted in inhomogeneous molten flow (Ti-rich melt pool) and asymmetric heat transfer during the welding process, contributing to the formation of these intermetallic phases due to metallurgical dissimilarity as shown in the phase diagram of Ti–Ni (Chatterjee et al., 2008). NiTi is reportedly more erosion-resistant

than stainless steel (Hiraga et al., 1999; Richman et al., 1995). During welding, the fusion zone that resulted in between base metals produces the compositional differences zone which influence the corrosion process. Dissimilar metal welding produces macroscopic galvanic corrosion which leads to erosion (Abraham et al., 2014). Therefore, formation of NiTi has helped to overcome this issues.

Therefore, the presence of NiTi as an intermetallic compound in the weld zone is an advantage in improving the joining properties. During dissimilar laser welding of titanium alloy and nickel alloy, base metal grains grew into the welding pool. A steep composition gradient was observed at the interface. NiTi and $NiTi_2$ dendrites grew to form a band in the HAZ. The NiTi liquidus line had a steeper slope compared to $NiTi_2$, suggesting the latter is likely to form heterogeneously. According to the phase diagram, both NiTi and $NiTi_2$ constitute the bulk of the weld microstructure. The microstructures may have been caused by the precipitation of $NiTi_2$ from the rich Ti β2 phase and its entrapment due to the growing NiTi dendrites. These particles can nucleate before NiTi in certain circumstances (Kocich et al., 2013).

The XRD analysis indicates that NiTi and $NiTi_2$ formed in the FZ and HAZ. The $NiTi_2$ phase is not recommended in large quantities, because it can lead to a strong tendency of hot cracking, which is prone to cause weaker joints (Chatterjee et al., 2008; Kocich et al., 2013; Miranda et al., 2015; J. P. Oliveira et al., 2016). Figure 4.38 indicates that a high-temperature β2 phase (austenite) from NiTi was found in samples D2 and D3, which further changed to a low-temperature B19' phase (martensite) when the overlapping factor was 30% for sample D1 and the welding speed increased to 50 mm/s for sample E3. The amount of NiTi also decreased when the welding speed increased (E3) and the overlapping factor reduced (D1). Based on the XRD analysis, $NiTi_2$ formed in all samples. Nevertheless, the peak $NiTi_2$ was detected only in D1 and

E3. This may be related to the peritectic reaction that did not occur in samples D2 and D3. At lower heat input where shorter heating and cooling time are needed for laser welding, the penetration of Ni from Inconel 600 was insufficient, resulting in the XRD peak of $NiTi_2$ and martensitic phase of NiTi. However, with higher heat input and slightly longer welding time, the penetration of Ni from Inconel 600 was sufficient, thus causing the XRD peak of the NiTi austenitic phase to become more apparent (Hiraga et al., 1999). This was proven by the increased number of NiTi with the increasing overlapping factor, whereas the NiTi count reduced when laser welding speed increased. The changes in XRD counts show the differences clearly. Similar phases were detected in other related studies, proving that the X-ray beam hit the welded area (Chatterjee et al., 2008; Hiraga et al., 1999). Limited peaks were found during XRD, indicating a tentative phase indexation of these phases. The overlapping factor and laser welding speed clearly affected the microstructural properties of the weld joint.

The results are also in accordance with the results obtained from metallurgical characterization, indicating that heat input is the main factor affecting weld joint geometry and tensile properties. The greater NiTi presence in D3 contributed the highest force due to its super elastic properties. In terms of erosion properties, the austenitic phase of NiTi showed higher super elastic and erosion resistance than the martensitic phase. This explains why the D3 sample needed the most force to fracture, as the austenitic phase accumulated little strain (Hiraga et al., 1999).
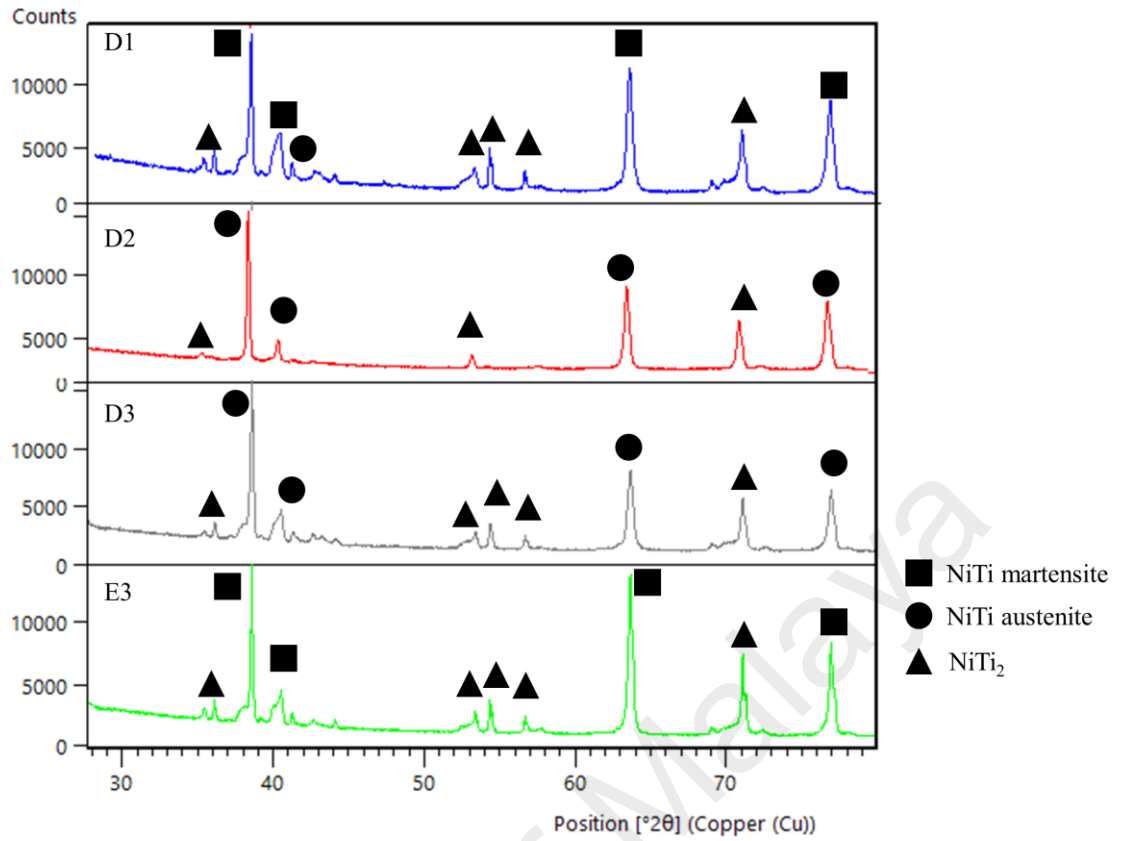
Figure 4.38: XRD patterns of samples D1, D2, D3 and E3

4.6.7 Weld bead microhardness measurement

Figure 4.39 depicts the effects of the overlapping factor and welding speed on weld bead hardness distribution. The hardness was studied across the entire weld bead profile (including the base metal, heat-affected zone and fusion zone).
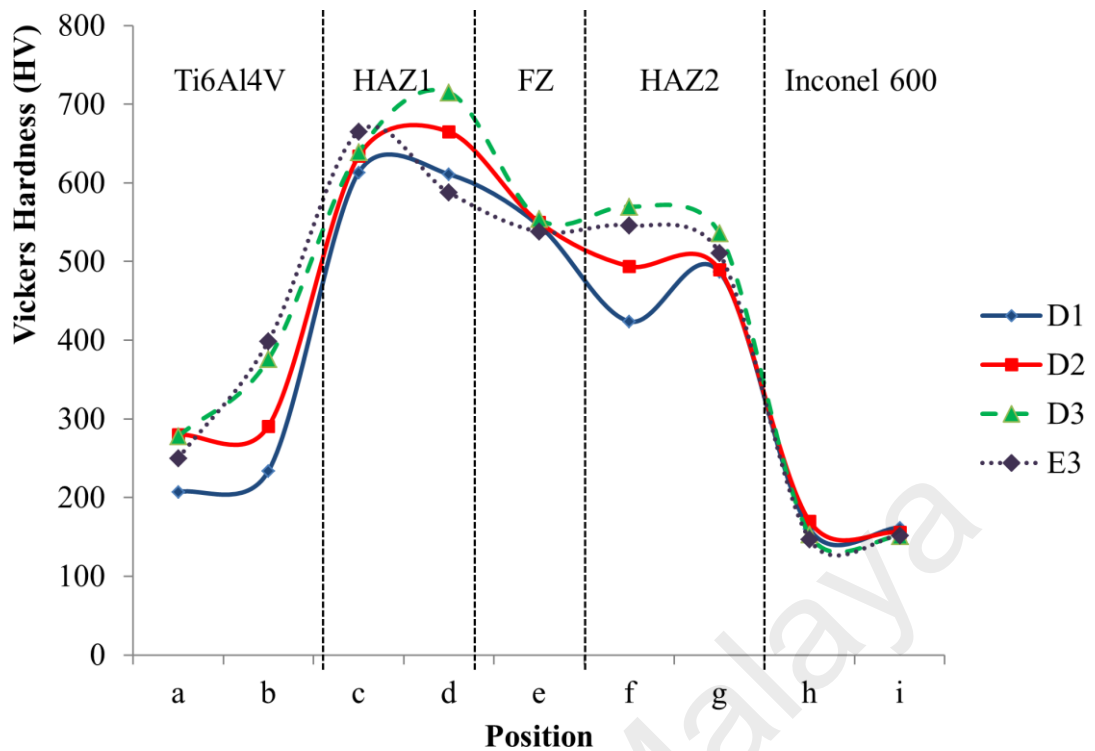
Figure 4.39: Vickers microhardness profiles of samples D1, D2, D3 and E3

The hardness of the Inconel 600 base material was around 140–160 HV, whereas the hardness of the Ti6Al4V base material was around 260–300 HV. As the overlapping factor increased, the FZ and HAZ hardness increased. The hardest sample was achieved at a welding speed of 40 mm/s and overlapping factor of 50%. The hardness at HAZ1 was higher than HAZ2, as HAZ1 was closer to the Ti6Al4V base material, which had higher hardness. As shown in Figure 4.39, sample D3 displayed the highest hardness among its counterparts approximately 200% from the base metals, with 554 HV at FZ, 715 HV at HAZ1 and 570 HV at HAZ2. This is attributed to the presence of NiTi, as the Vickers hardness of NiTi alloy reportedly ranges between 380 and 440 HV (Brantley & Eliades, 2011). Both skin and stringers in this study were annealed by heat treatment. When welding in this condition, there is a possibility that micro fissures will form in the HAZ region due to the coarser grains formed. The measured FZ hardness was higher than the base metals. Meanwhile, the hardness in the HAZ region was even higher than

the FZ region. The hardness in the FZ region was observed to be lower than the HAZ region, as shown in Figure 4.39. This was a result of the higher amount of molten metal in FZ due to the lack of precipitate strengthening caused by particles dispersing from the precipitate. A hardness transition between the FZ and base metal occurred and the HAZ measured the highest hardness among the three regions. In other comparable studies, similar areas were indicated for hardness measurement (Atabaki et al., 2014). Overall, all mechanical properties and metallurgical results obtained from the experiments were satisfactory and no additional filler alloy was needed. The results proved that Ti6Al4V and Inconel 600 can be single-sided laser-welded successfully.

CHAPTER 5: CONCLUSIONS AND RECOMMENDATIONS

5.1 Conclusions

Laser welding parameters were manipulated to evaluate their effects on microstructural and mechanical properties post laser welding of dissimilar metals. Successive laser welding of a double-sided T-joint comprising of 2mm thick AA7075-T6 and 3mm thick AA2024-O was possible without filler material addition in a T-joint configuration using low-power Ytterbium-fiber laser. During laser welding, the rapid heating and solidification formed smaller grains at the FZ compared to the HAZ and BM at all welding speeds. The gap line observed on the joints increased from 0.5 to 0.8, 1.1, 1.5 and 1.8 mm as the welding speed increased from 9 to 12, 15, 18 and 21 mm/s respectively. C1 (with laser power of 270 W, 9 mm/s and 0 offset focal distance) denoted the highest heat input calculated of approximately 4715 J/mm, which required 642.79 N to break the joint. Joining strength weakened as welding speed increased. The effect of laser focal distance was investigated for a constant laser power of 270 W and laser speed of 18 mm/s. The focal distances evaluated at -1, 0 and +1 from the reference focal distance of 346 mm at 338 mm and 354 mm respectively calculated using the Rayleigh length. As the focal distance changed from -1 to +1 offset, the weldment became stronger and proven by the microhardness evaluation results. Offset focal distance of +1 resulted in the highest hardness value of 414 HV in the FZ of sample C7. The HAZ1 hardness also increased from 162 HV to 344 HV, while the HAZ2 hardness increased from 214 HV to 373 HV.

To improve the mechanical properties of the weldment, aluminum filler alloy BA4047 was added on both sides of during laser welding AA2024-O and AA7075-T6. There was an improvement in the overall results. According to the pull test results, the

fracture force of the welded joints significantly increased up to 250-350% with the addition of BA4047 filler wire at any predefined welding speed. Microhardness improved 1200% for lowest welding speed proving addition of filler is successful.

Single-sided laser welding was successfully performed on thin sheets of Ti6Al4V (0.5 mm thickness) and Inconel 600 (1 mm thickness) in a T-joint configuration using low-power Ytterbium-fiber laser. The highest fracture force was obtained at welding speed of 40 mm/s, overlapping factor of 50% and laser power of 250 W, proving a sound joint was obtained because sufficient heat input was produced. This is proven by the minor gap line of 0.202 mm. It can be concluded that the gap line length increased and the penetration depth decreased as the welding speed increased while the overlapping factor decreased. NiTi and $NiTi_2$ intermetallic compound formed in the FZ due to the crystallographic mismatch between Ni and Ti as well as the differences in the thermo-physical properties of the materials. The hardest sample was achieved at a welding speed of 40 mm/s and overlapping factor of 50%. The hardness at HAZ2 was lower than HAZ1, which was closer to the Ti6Al4V base material attributed to the presence of NiTi.

Fuzzy logic was used as a method to analyze all the preliminary pull tests to determine a range of parameters to run metallurgical and other mechanical properties studies. The developed Mamdani FES model can be used to predict the fracture force of similar properties materials that is required to break the weld influenced by laser parameters. The influence of laser power (W) and welding speed (mm/s) on the laser welding of dissimilar aluminum alloys, AA2024-O and AA7075-T6, was predicted. The goodness of fit (R^2) values in training and testing were 0.9963 and 0.9956 respectively, while the relative error (ε) values in training and testing were 7.85% and 5.58% respectively. The relative error was less than 10% and is considered acceptable. The

influence of laser power (W), welding speed (mm/s), and overlapping factor (%) on laser welding of dissimilar metals, titanium-based alloy, Ti6Al4V and nickel-based alloy, Inconel 600 was predicted next. From the study, it can be concluded that the goodness of fit (R^2) values for training and testing were 0.9849 and 0.8404 respectively, while the relative error (ε) values for training and testing were 6.95% and 3.20% respectively. These relative errors were also less than 10% and are considered acceptable. Surface plot analysis showed that the overlapping factor had the highest impact on fracture force, followed by welding speed and laser power. From the fuzzy logic smart model, a range of parameters were chosen for metallurgical and mechanical studies which minimize the effort to determine the optimum parameters.

5.2   Recommendations for future work

For future new research, influence of external magnetic field either constant or alternating on typical keyhole laser welding can be experimented using dissimilar metals. The influence of main parameters on complex configurations in dilution of element can be analyzed. Besides that, hybrid laser arc welding on dissimilar metals can bring new scope of research in competitive and demanding industries. Various metal surface roughnesses can be placed between the laser scanner head and working table, where the surface roughness will influence the laser beam reflection. Strength test analysis, metallurgical characterization, microstructural observation and microhardness evaluation can be done in all recommended studies to evaluate the influence of each parameter.

REFERENCES

Abraham, G. J., Bhambroo, R., Kain, V., Dey, G. K., & Raja, V. S. (2014). Intergranular Corrosion Susceptibility of Alloy 600 after Autogenous Tungsten Inert Gas and Laser Beam Welding using Electrochemical Technique. *High Temperature Materials and Processes, 33*(2), 137-146.

Acerra, F., Buffa, G., Fratini, L., & Troiano, G. (2010). On the FSW of AA2024-T4 and AA7075-T6 T-joints: an industrial case study. *The International Journal of Advanced Manufacturing Technology 48*(9-12), 1149-1157

Atabaki, M. M., Nikodinovski, M., Chenier, P., Ma, J., Liu, W., & Kovacevic, R. (2014). Experimental and numerical investigations of hybrid laser arc welding of aluminum alloys in the thick T-joint configuration. *Optics and Laser Technology, 59,* 68-92.

Badini, C., Pavese, M., Fino, P., & Biamino, S. (2009). Laser beam welding of dissimilar aluminium alloys of 2000 and 7000 series: effect of post-welding thermal treatments on T joint strength. *Science and Technology of Welding and Joining, 14*(6), 484-492.

Balasubramanian, K. R., Buvanashekaran, G., & Sankaranarayanasamy, K. (2010). Modeling of laser beam welding of stainless steel sheet butt joint using neural networks. *CIRP Journal of Manufacturing Science and Technology, 3*(1), 80-84.

Bartels, C. (1914). United States Patent title: Plate-edge joint, No.US1107477 A

Borrisutthekula, R., Yachia, T., Miyashitab, Y., & Mutoh, Y. (2007). Suppression of intermetallic reaction layer formation by controlling heat flow in dissimilar joining of steel and aluminum alloy. *Materials Science and Engineering: A, 467*(1-2), 108-113.

Bradley, G., & James, M. (2000). Geometry and microstructure of metal inert gas and friction stir welded aluminium alloy 5383-H321. *Metalurgical and Materials Transactions, 30*, 121-125.

Brantley, W. A., & Eliades, T. (2011). *Orthodontic Materials: Scientific and Clinical Aspects*. Germany: Thieme.

Cao, X., Wallace, W., Immarigeon, J.-P., & Poon, C. (2003a). Research in laser welding of wrought aluminium alloys. I. laser welding processes. . *Materials and Manufacturing Processes, 18*(1), 1-22.

Cao, X., Wallace, W., Immarigeon, J.-P., & Poon, C. (2003b). Research in laser welding of wrought aluminium alloys. II. metallurgical microstructures, defects, and mechanical properties. *Materials and Manufacturing Processes, 18*(1), 23-49.

Carpinteri, A., Brighenti, R., Huth, H. J., & Vantadori, S. (2004). Fatigue growth of a surface crack in a welded T-joint. *International Journal of Fatigue, 27*(1), 59-69.

Chatterjee, S., Abinandanan, T. A., & Chattopadhyay, K. (2006). Microstructure development during dissimilar welding: Case of laser welding of Ti with Ni involving intermetallic phase formation. *Journal of Materials Science, 41*(3), 643-652.

Chatterjee, S., Abinandanan, T. A., & Chattopadhyay, K. (2008). Phase formation in Ti/Ni dissimilar welds. *Materials Science and Engineering: A, 490*(1-2), 7-15.

Chen, H. C., Pinkerton, A. J., & Li, L. (2011). Fibre laser welding of dissimilar alloys of Ti-6Al-4V and Inconel 718 for aerospace applications. *International Journal of Advanced Manufacturing Technology, 52*(9-12), 977-987.

Cicala, E., Duffet, G., Andrzejewski, H., & Grevey, D. (2010). Continuous Welding of Al-Mg-Si Alloys with Nd:YAG Laser Irradiation: Tensile Properties Optimization of T-joint Seams. *Lasers in Engineering, 20*(3-4), 195-211.

Corporation, O. (2010). Optical Microscopes. Manual book from Olympus Corporation

Dahotre, N. B., & Harimkar, S. P. (2008). *Laser Fabrication and Machining of Materials*. Spring Street, New York, NY 10013, USA: Springer.

Damask, J. N. (2005). *Polarization Optics in Telecommunications* (1 ed. Vol. 101): Springer-Verlag New York.

Daneshpour, S., Koçak, M., Bayraktar, F. S., & Riekehr, S. (2009). Damage Tolerance Analyses of Laser Welded "Skin-Clip" Joints for Aerospace Applications. *Welding in the World, 53*(3), 90-98.

Davis, J. R. (2000). *Nickel, Cobalt, and Their Alloys* (illustrated ed.): ASM International.

Dawes, C. (1992). *Laser Welding: A Practical Guide*: Woodhead Publishing.

Dernoncourt, F. (2011). Introduction to fuzzy logic: MIT (Massachusetts Institute of Technology).

Donachie, M. J. (2000). *Titanium: A Technical Guide*: ASM International.

Dragolich, K. S., & DiMatteo, N. D. (1994). *Fatigue Data Book: Light Structural Alloys* (S. D. Henry Ed.): ASM International.

Elijah Kannatey-Asibu, J. (2009). *Principles of Laser Materials Processing* (Vol. 4): John Wiley & Sons.

Enz, J., Khomenko, V., Riekehr, S., Ventzke, V., Huber, N., & Kashaev, N. (2015). Single-sided laser beam welding of a dissimilar AA2024-AA7050 T-joint. *Materials & Design, 76*, 110-116.

Enz, J., Riekehr, S., Ventzke, V., Kashaev, N., & Huber, N. (2012). Process optimisation for the laser beam welding of high-strength aluminium-lithium alloys. *Schweißen und Schneiden, 64*(8), 482-485.

Ezazi, M., Yusof, F., Sarhan, A. A., Shukor, M. H. A., & Fadzil, M. (2015). Employment of fiber laser technology to weld austenitic stainless steel 304l with aluminum alloy 5083 using pre-placed activating flux. *Materials & Design, 87*, 105-123.

Fratini, L., Buffa, G., Filice, L., & Gagliardi, F. (2006). Friction stir welding of AA6082-T6 T-joints: process engineering and performance measurement. *J. Eng. Manuf.,Part B, 220*(5), 669-676.

Fratini, L., Buffa, G., & Shivpuri, R. (2009). Influence of material characteristics on plastomechanics of the FSW process for T-joints. *Materials and Design, 30*, 2435–2445.

Gale, W. F., & Totemeier, T. C. (2004). *Smithells Metals Reference Book (8th Edition)*: Elsevier.

Gao, X.-L., Liu, J., Zhang, L.-J., & Zhang, J.-X. (2014). Effect of the overlapping factor on the microstructure and mechanical properties of pulsed Nd:YAG laser welded Ti6Al4V sheets. *Materials Characterization, 93*, 136-149.

Graville, B. A. (1976). Patent title: Method of butt welding, No. US3984652 A.

Griot, C. M. (2009). Introduction to laser technology. *2*, 10.11-10.32.

Grote, K.-H., & Antonsson, E. K. (2009). *Springer Handbook of Mechanical Engineering, Volume 10*: Springer Science & Business Media.

Guo, J. F., Chen, H. C., Sun, C. N., Bi, G., Sun, Z., & Wei, J. (2014). Friction stir welding of dissimilar materials between AA6061 and AA7075 Al alloys effects of process parameters. *Materials and Design, 56*, 185-192.

Harwani, M. D. (2014). A Review: Welding Of Dissimilar Metal Alloys by Laser Beam Welding & Friction Stir Welding Techniques. *International Journal of engineering Research and Applications, 1*(4), 64-70.

Hiraga, H., Inoue, T., Shimura, H., & Matsunawa, A. (1999). Cavitation erosion mechanism of NiTi coatings made by laser plasma hybrid spraying. *Wear, 231*(2), 272-278.

Hitz, C. B., Ewing, J. J., & Hecht, J. (2012). *Introduction to Laser Technology* (4 ed.). New Jersey: John Wiley & Sons.

Holtkamp, J., Roesner, A., & Gillner, A. (2010). Advances in hybrid laser joining. *International Journal of Advanced Manufacturing Technology, 47*(9-12), 923-930.

Holzer, M., Hoppe, F., Mann, V., Hofmann, K., Hugger, F., Roth, S., & Schmidt, M. (2015). *Influence of filler wire and focus diameter on crack formation in laser beam welding of high strength aluminum alloys.* Paper presented at the Lasers in Manufacturing Conference.

Hossain, A., Hossain, A., Nukman, Y., Hassan, M. A., Harizam, M. Z., Sifullah, A. M., & Parandoush, P. (2016). A Fuzzy Logic-Based Prediction Model for Kerf Width in Laser Beam Machining. *Materials and Manufacturing Processes, 31*(5), 679-684.

Huntress, E. (2015). Benefits of Laser Welding. *Fab Shop Direct Magazine*. accessed on 10 March 2016

Ion, J. C. (2000). Laser beam welding of wrought aluminium alloys. *Science and Technology of Welding and Joining, 5*(5), 265-276.

John J. Marko, J. (1980) Patent title: Welded lap joint and method of making the same, No.US4187407 A.

Katayama, S. (2013). *Handbook of Laser Welding Technologies* (1 ed. Vol. 1): Elsevier.

Khan, M. M. A., Romoli, L., Fiaschi, M., Dini, G., & Sarri, F. (2011). Experimental design approach to the process parameter optimization for laser welding of martensitic stainless steels in a constrained overlap configuration. *Optics and Laser Technology, 43*(1), 158-172.

Klages, K., Ruettimann, C., & Olowinsky, A. M. (2003). *Laser Beam Micro Welding of Dissimilar Metals.* Paper presented at the Fourth International Symposium on Laser Precision Microfabrication, Munich, Germany.

Klir, G. J., & Yuan, B. (1995). *Fuzzy Sets and Fuzzy Logic: Theory and Applications*. Upper Saddle River, NJ, USA: Prentice Hall PTR.

Kocich, R., Szurman, I., & Kursa, M. (2013). The Methods of Preparation of Ti-Ni-X Alloys and Their Forming. In F. M. B. Fernandes (Ed.), *Shape Memory Alloys - Processing, Characterization and Applications*

Komvopoulos, K. (2010). *Mechanical Testing of Engineering Materials*: Cognella.

Kumar, S., Datta, D., Sharma, S., Chourasiya, G., Babu, D., & Sharma, D. (2014). Estimation of distance error by fuzzy set theory required for strength determination of HDR 192Ir brachytherapy sources. *Journal of medical physics/Association of Medical Physicists of India, 39*(2), 85.

Kurakake, Y., Farazila, Y., Miyashita, Y., Otsuka, Y., & Mutoh, Y. (2013). Effect of Molten Pool Shape on Tensile Shear Strength of Dissimilar Materials Laser Spot Joint between Plastic and Metal. *Journal of Laser Micro/Nanoengineering, 8*(2), 161-164.

Lee, M. F., Huang, J. C., & Ho, N. J. (1996). Microstructural and mechanical characterization of laser-beam welding of a 8090 Al-Li thin sheet. *Journal of Materials Science, 31*(6), 1455-1468.

Li, M., Li, Z. G., Zhao, Y., Li, H., Wang, Y. H., & Huang, J. (2011). Influence of Welding Parameters on Weld Formation and Microstructure of Dual-Laser Beams Welded T-Joint of Aluminum Alloy. *Advances in Materials Science and Engineering*.

Liao, Y. C., & Yu, M. H. (2007). Effects of laser beam energy and incident angle on the pulse laser welding of stainless steel thin sheet. *Journal of Materials Processing Technology, 190*(1-3), 102-108.

Machold, W., P., S., Bayraktar, F., Riekehr, S., Koçak, M., & Schreyer, A. (2008). Influence of the welding sequence on residual stresses in laser welded T joints of an airframe aluminium alloy. *Materials Science Forum, 571*, 375-380.

Mai, T. A., & Spowage, A. C. (2004). Characterisation of dissimilar joints in laser welding of steel-kovar, copper-steel and copper-aluminium. *Materials Science and Engineering: A, 374*(1-2), 224-233.

Masoumi, M., Marashi, S. P. H., & Pouranvari, M. (2010). Metallurgical and Mechanical characterization of laser spot welded low carbon steel sheets. *Steel research international, 81*(12), 1144-1151.

Mifflin, H. (Ed.) (2011) Dictionary of the English Language (5 ed.). Houghton Mifflin Harcourt Publishing Company.

Miller, D. (2004). Determining the cost of welding. *Welding Design and Fabrication, 77*(3), 32-37.

Miranda, R. M., Assunção, E., Silva, R. J. C., Oliveira, J. P., & Quintino, L. (2015). Fiber laser welding of NiTi to Ti-6Al-4V. *The International Journal of Advanced Manufacturing Technology, 81*(9), 1533-1538.

Moraitis, G. A., & Labeas, G. N. (2008). Residual stress and distortion calculation of laser beam welding for aluminum lap joints. *Journal of Materials Processing Technology, 198*(1-3), 260-269.

MPR. (2012). Off to the races. *Metal Powder Report, 67,* 22-24.

Nelson, C., & Crist, J. (2012). Predicting laser beam characteristics. *Laser Technik Journal, 9*(1), 36-39.

Norris, J. T., Robino, C. V., Hirschfeld, D. A., & Perricone, M. J. (2011). Effects of Laser Parameters on Porosity Formation: Investigating Millimeter Scale Continuous Wave Nd:YAG Laser Welds. *Welding Journal, 90*(10), 198.

Nukman, Y., Hassan, M. A., & Harizam, M. Z. (2013). Optimization of prediction error in CO2 laser cutting process by Taguchi artificial neural network hybrid with genetic algorithm. *Applied Mathematics & Information Sciences, 7*(1), 363–370.

Okhotnikov, O. G. (2012). *Fiber Lasers* (1 ed.): Wiley-VCH.

Oliveira, A. C., Siqueira, R. H. M., Riva, R., & Lima, M. S. F. (2015). One-sided laser beam welding of autogenous T-joints for 6013-T4 aluminium alloy. *Materials & Design, 65,* 726-736.

Oliveira, J. P., Panton, B., Zeng, Z., Andrei, C. M., Zhou, Y., Miranda, R. M., & Fernandes, F. M. B. (2016). Laser joining of NiTi to Ti6Al4V using a Niobium interlayer. *Acta Materialia, 105,* 9-15.

Ozaki, H., & Kutsuna, M. (2009). Laser-roll welding of a dissimilar metal joint of low carbon steel to aluminium alloy using 2 kW fibre laser. *Welding International, 23*(5), 345-352.

Padovani, C., Fratini, L., Squillace, A., & Bellucci, F. E. (2007). Electrochemical analysis on friction stir welded and laser welded 6XXX aluminium alloys T-joints. *Corrosion Reviews, 25*(3-4), 475-489.

Paleocrassas, A. G. (2009). *Process characterization of low speed, fiber laser welding of AA 7075-T6 application to fatigue crack repair.* (Degree of Doctor of Philosophy), North Carolina State University.

Park, S. J. (2008). *Dissimilar metal welding titanium and steel sheet by fiber laser*. Paper presented at the 3rd Pacific International Conference on Applications of Lasers and Optics, Beijing, China.

Park, Y. W., Yu, J., & Rhee, S. (2010). A Study on the Weld Characteristics of 5182 Aluminum Alloy by Nd:Yag Laser Welding with Filler Wire for Car Bodies. *International Journal of Automotive Technology, 11*(5), 729-736.

Pederson, R. (2002). Microstructure and Phase transformation of Ti-6Al-4V. (Doctoral dissertation, Luleå tekniska universitet).

Pedrycz, W. (1994). Why triangular membership functions? *Fuzzy Sets and Systems, 64*(1), 21-30.

Peterman, D. (2005). The Misunderstood M-square. *Oemagazine,* 301.

Pinto, L. A., Quintino, L., Miranda, R. M., & Carr, P. (2010). Laser Welding of Dissimilar Aluminium Alloys with Filler Materials. *Welding in the World, 54*(11-12), R333-R341.

Prisco, A., Troiano, G., Acerra, F., Bellucci, B., Squillace, A., & Prisco, U. (2008). LBW of Similar and Dissimilar Skin-Stringer Joints Part I: Process Optimization and Mechanical Characterization. *Adv Mater Res, 38*, 306-319.

Rajasekaran, S., & Pai, G. A. V. (2003). *Neural Networks, Fuzzy Logic and Genetic Algorithm: Synthesis and Applications*: PHI Learning.

Rebak, R. B., & Crook, P. (2000). Nickel alloys for corrosive environments. *Advanced Materials & Processes*.

Renk, K. F. (2012). *Basics of Laser Physics*. New York, London: Springer Heidelberg Dordrecht.

Reutzel, E. W. (2009). Advantages and disadvantages of arc and laser welding. In F. O. Olsen (Ed.), *Hybrid Laser-Arc Welding* (pp. 323): Woodhead Publishing

Ribic, B., Palmer, T. A., & DebRoy, T. (2009). Problems and issues in laser-arc hybrid welding. *International Materials Reviews, 54*(4), 223-244.

Richman, R. H., Rao, A. S., & Kung, D. (1995). Cavitation erosion of NiTi explosively welded to steel. *Wear, 181–183, Part 1*, 80-85.

Rojas, R. (2013). *Neural networks: a systematic introduction*: Springer Science & Business Media.

Ross, T. J. (2009). *Fuzzy logic with engineering applications*: John Wiley & Sons.

Rotella, G., & Umbrello, D. (2014). Finite element modeling of microstructural changes in dry and cryogenic cutting of Ti6Al4V alloy. *CIRP Annals - Manufacturing Technology, 63*(1), 69-72.

Saleh, B. E. A., & Teich, M. C. (1991). *Fundamentals of Photonics*: John Wiley & Sons, Inc.

Sanchez-Amaya, J. M., Delgado, T., De Damborenea, J. J., Lopez, V., & Botana, F. J. (2009). Laser welding of AA 5083 samples by high power diode laser. *Science and Technology of Welding and Joining, 14*(1), 78-86.

Sanchez-Amaya, J. M., Delgado, T., Gonzalez-Rovira, L., & Botana, F. J. (2009). Laser welding of aluminium alloys 5083 and 6082 under conduction regime. *Applied Surface Science, 255*(23), 9512-9521.

Schubert, E., Klassen, M., Zerner, I., Walz, C., & Sepold, G. (2001). Light-weight structures produced by laser beam joining for future applications in automobile and aerospace industry. *Journal of Materials Processing Technology, 115*(1), 2-8.

Shanmugam, N. S., Buvanashekaran, G., Sankaranarayanasamy, K., & Kumar, S. R. (2010). A transient finite element simulation of the temperature and bead profiles of T-joint laser welds. *Materials & Design, 31*(9), 4528-4542.

Shen, Y., Liu, Y., Sun, W., Dong, H., Zhang, Y., Wang, X., . . . Ji, R. (2015). High-speed dry compound machining of Ti6Al4V. *Journal of Materials Processing Technology, 224*, 200-207.

Shokrani, A., Dhokia, V., & Newman, S. T. (2012). Environmentally conscious machining of difficult-to-machine materials with regard to cutting fluids. *International Journal of Machine Tools & Manufacture, 57*, 83-101.

Simeon, M. M., & Vadim, P. V. (2013). *Laser-Assisted Microtechnology* (R. M. Osgood Ed. Vol. 19): Springer Science & Business Media.

Singh, R., Alberts, M. J., & Melkote, S. N. (2008). Characterization and prediction of the heat-affected zone in a laser-assisted mechanical micromachining process. *International Journal of Machine Tools and Manufacture, 48*(9), 994-1004.

Spectra-Physics. (2011). Calculating Power Density – A Shortcut (Photonics Technical). from Newport

Steen, W., & Mazumder, J. (2010). *Laser Material Processing* (4 ed.).

Sudarshan, T. S. (2007). *Surface Modification Technologies: Proceedings of the 20th International Conference on Surface Modification Technologies*: A S M International.

Sun, Z., & Ion, J. C. (1995). Laser-welding of dissimilar metal combinations. *Journal of Materials Science, 30*(17).

Tao, W., Yang, Z. B., Chen, Y. B., Li, L. Q., Jiang, Z. G., & Zhang, Y. L. (2013). Double-sided fiber laser beam welding process of T-joints for aluminum aircraft

fuselage panels: Filler wire melting behavior, process stability, and their effects on porosity defects. *Optics and Laser Technology, 52*, 1-9.

Tavares, S. M. O., Azevedo, P. C. M., Emilio, B., Richter-Trummer, V., Figueiredo, M. A. V., Vilaca, P., & de Castro, P. M. S. T. (2009). Friction Stir Welding of T-Joints in Dissimilar Aluminum Alloys. *Imece2008: Proceedings of the ASME International Mechanical Engineering Congress and Exposition*, 265-273.

Tomashchuk, I., Grevey, D., & Sallamand, P. (2015). Dissimilar laser welding of AISI 316L stainless steel to Ti6-Al4-6V alloy via pure vanadium interlayer. *Materials Science and Engineering a-Structural Materials Properties Microstructure and Processing, 622*, 37-45.

Trabalho, C. D. (2009). *Characterization of Nd:YAG pulsed laser welded austenitic AISI 304L stainless steel.* Paper presented at the V Congresso Brasileiro De Engenharia De Fabricacao, Brazil.

Unt, A., & Salminen, A. (2015). Effect of welding parameters and the heat input on weld bead profile of laser welded T-joint in structural steel. *Journal of Laser Applications, 27*.

Ventzke, V., Riekehr, S., Horstmann, M., Haack, P., & Kashaev, N. (2014). One-sided Nd:YAG laser beam welding for the manufacture of T-joints made of aluminium alloys for aircraft construction. *Welding and Cutting, 13*(4), 245-249.

Vince. (2015). Welding Exhaust Systems - Part 1. *Burn Stainless*.

Walsh, C. A. (2002). Laser Welding - Literature Review *Materials Science and Metallurgy Department*. England: University of Cambridge.

Weman, K. (2003). *Welding processes handbook*. Cambridge, England: Woodhead Publishing Limited.

Xu, G. X., Wu, C. S., Ma, X. Z., & Wang, X. Y. (2013). Numerical Analysis of Welding Residual Stress and Distortion in Laser plus GMAW Hybrid Welding of Aluminum Alloy T-Joint. *Acta Metallurgica Sinica-English Letters, 26*(3), 352-360.

Yang, Z. B., Tao, W., Li, L. Q., Chen, Y. B., Li, F. Z., & Zhang, Y. L. (2012). Double-sided laser beam welded T-joints for aluminium aircraft fuselage panels: Process, microstructure, and mechanical properties. *Materials and Design, 33*, 652-658.

Yanga, J., Suna, S., Brandtb, M., & Yan, W. (2010). Experimental investigation and 3D finite element prediction of the heat affected zone during laser assisted machining of Ti6Al4V alloy. *Journal of Materials Processing Technology, 210*(15), 2215-2222.

Zadeh, L. A. (1996). *Fuzzy sets, fuzzy logic, and fuzzy systems: selected papers by Lotfi A Zadeh* (Vol. 6): World Scientific.

Zain-ul-Abdein, M., Nelias, D., Jullien, J. F., & Deloison, D. (2009). Prediction of laser beam welding-induced distortions and residual stresses by numerical simulation for aeronautic application. *Journal of Materials Processing Technology, 209*(6), 2907-2917.

Zhang, D., Zhao, Z., Gao, S., & Zhao, H. (2012). *Research on CO2 Laser Welding with Filler Wire of Dissimilar High Strength Aluminum Alloy 2024 and 7075.* Paper presented at the Photonics and Optoelectronics (SOPO), 2012 Symposium on.

Zhang, L. J., Zhang, X. J., Ning, J., & Zhang, J. X. (2015). Modulated fiber laser welding of high reflective AZ31. *International Journal of Advanced Manufacturing Technology, 76*(1-4), 721-733.

Zhang, Y., Chen, G. Y., Wei, H. Y., & Zhang, J. (2008). A novel "sandwich" method for observation of the keyhole in deep penetration laser welding. *Optics and Lasers in Engineering, 46*(2), 133-139.

Zhao, Y., Zhou, L., Wang, Q., Yan, K., & Zou, J. (2014). Defects and tensile properties of 6013 aluminum alloy T-joints by friction stir welding. *Materials & Design, 57*, 146-155.

Zhou, G., Yang, X. Q., Cui, L., Zhang, Z. H., & Xu, X. D. (2012). Study on the Microstructures and Tensile Behaviors of Friction Stir Welded T-joints for AA6061-T4 Alloys. *Journal of Materials Engineering and Performance 21*(10), 2131-2139.

LIST OF PUBLICATIONS

Academic Journals

1. Janasekaran, S., Jamaludin, M. F., Muhamad, M. R., Yusof, F., & Shukor, M. H. A. (2017). Autogenous double-sided T-joint welding on aluminum alloys using low power fiber laser. The International Journal of Advanced Manufacturing Technology, 90(9-12), 3497-3505. (ISI-Indexed)

2. Janasekaran, S., Tan, A., Yusof, F., & Abdul Shukor, M. (2016). Influence of the Overlapping Factor and Welding Speed on T-Joint Welding of Ti6Al4V and Inconel 600 Using Low-Power Fiber Laser. Metals, 6(6), 134. (ISI-Indexed)

3. Janasekaran, S., Tan, A. W., Yusof, F., Shukor, A., & Hamdi, M. (2016). Feasibility study of low power fiber laser welding AA2024 and AA7075 alloys T-Joint. In Key Engineering Materials (Vol. 701, pp. 182-186). Trans Tech Publications. (ISI-Indexed)

4. Janasekaran, S., Yusof, F., Zin, H. M., Jamaludin, M. F., & Shukor, M. H. A. (2017). A fuzzy logic-based prediction model for fracture force using low-power fiber laser beam welding. The International Journal of Advanced Manufacturing Technology, 1-8. (ISI-Indexed)

5. Janasekaran, S., Jamaludin, M. F., Yusof, F., Shukor, M. H. A., & Ariga, T. (2017). Influence of BA4047 filler addition through Mamdani fuzzy logic optimization for double-sided T-joint welding of aluminum alloys using low-power fiber laser. The International Journal of Advanced Manufacturing Technology, 1-11. (ISI-Indexed)

Conferences/Seminars

No	Title	Venue	Year
1	A preliminary study on joining of sapphire and Inconel 600 using low power fiber laser	Regional Conference on Materials Engineering, Kuala Lumpur -2014	2014
2	Laser welding of dissimilar materials	Seminar, CAREF, Faculty of Engineering, University Malaya	2014
3	Influence laser beam overlapping factor in joining dissimilar materials	Trends and new developments in Laser Technology, Technische Universität Dresden, Fraunhofer IWS, Dresden, Germany -2015	2015
4	Feasibility Study of Low Power Fiber Laser Welding AA2024 and AA7075 Alloys T-Joint	International Conference on Science & Engineering of Materials 2015 (ICoSEM2015) Pullman KL Hotel Kuala Lumpur, Malaysia	2015
5	A low power fiber laser welding of dissimilar materials in T-joint configuration	Candidature Defense, Level 5, Mechanical Department, Faculty of Engineering, University Malaya	2016
6	Laser welding of Aluminum alloy	Seminar, CAREF, Faculty of Engineering, University Malaya	2016
7	T-joint Welding of AA2024 and AA7075 Using Low Power Fiber Laser with addition of BA4047 filler alloy	International Symposium on Laser Precision Microfabrication (LPM), China	2016